DIRECT INK WRITING OF FUNCTIONAL FIBER COMPOSITES

BY

YIZHOU JIANG

B.S., Jilin University, 2015
M.S., University of Illinois at Chicago, 2016

DISSERTATION

Submitted as partial fulfillment of the requirements
for the degree of Doctor of Philosophy in
Industrial Engineering and Operations Research
in the Graduate College of the
University of Illinois at Chicago, 2020

Chicago, Illinois

DEFENSE COMMITTEE

Dr. Yayue Pan, Chair and Advisor
Dr. Alan Feinerman
Dr. Mengqi Hu
Dr. Carmen Lilley
Dr. Alexander L. Yarin

In Loving Memory of
My Beloved Grandmother

JINLAN MA

1928 – 2019

ACKNOWLEDGEMENTS

I would first like to express my most profound appreciation to my advisor, Dr. Yayue Pan, whose expertise was invaluable in formulating the research questions and methodologies. Your insightful feedback pushed me to sharpen my thinking and brought my work to a higher level.

I want to extend my sincere thanks to my dissertation committee, Dr. Alan Feinerman, Dr. Mengqi Hu, Dr. Carmen Lilley, Dr. Alexander L. Yarin, for the unwavering support. You provided guidance in all areas that helped me accomplish my research goals and enjoy myself in the process.

I acknowledge my colleagues and friends at UIC, Dr. Haiyang He, Dr. Lu Lu, Dr. Malek Nofal, Erina Joyee, Ketki Lichade, Yilong Wang, Chengji Zhang, and Jevon Plog's tremendous help. I would particularly like to single out my best friend, Meng Cheng; I want to thank you for further my research.

In addition, I sincerely thank my parents for wise counsel. You are always there for me. Finally, I could not have completed this dissertation without the support of my girlfriend, Siyao Li; without your long-term support, this dissertation would not be possible at all.

TABLE OF CONTENTS

TABLE OF CONTENTS (continued)

LIST OF FIGURES

LIST OF FIGURES (continued)

LIST OF ABBREVIATIONS

3D	Three-Dimensional
ABS	Acrylonitrile Butadiene Styrene
AM	Additive Manufacturing
BET	Brunauer Emmett Teller
CNT	Carbon Nanotube
CV	Cyclic Voltammetry
DI	Deionized
DIW	Direct Ink Writing
EF	Electric Field
EIS	Electrochemical Impedance Spectroscopy
ESR	Equivalent Series Resistance
FDM	Fused Deposition Modeling
FR	Flexible Resin
G'	Storage Modulus
G''	Loss Modulus
PDMS	Polydimethylsiloxane
PET	Polyethylene Terephthalate
PLA	Polylactic Acid
PP	Polypropylene
PVA	Polyvinyl Alcohol
rGO	Reduced Graphene Oxide
SC	Supercapacitor
SEM	Scanning Electron Microscopy
SL	Stereolithography
SLS	Selective Laser Sintering
SMA	Shape Memory Alloy
SMP	Shape Memory Polymer
TFF	Transparent Flax Fiber
UV	Ultraviolet

SUMMARY

Fiber-polymer composites show tremendous promise due to their unique properties. Such composites usually consist of polymer matrix embedded with high-strength synthetic/natural fibers. They generally possess exceptional mechanical properties, such as high specific stiffness and strength. By printing fiber-polymer composites using additive manufacturing (AM) techniques, the three-dimensional (3D) models can be fabricated with arbitrary free-form geometry, improved mechanical properties, and even multiple functionalities. Yet grand challenges such as limited material choices, weak fiber-matrix interface, and little control over filler distributions within the matrix still exist in the additive manufacturing of fiber-polymer composites.

Among the many additive manufacturing techniques that have been investigated for productions of fiber-polymer composites, direct ink writing (DIW) is an extrusion-based AM approach and has a relatively diverse choice of printable matrix materials. Applications, including energy storage, mechanical reinforcements, and biomimetic materials, have been presented through DIW of fiber composites. However, challenges, including the complicated process planning, low geometrical accuracy, filament shape instabilities, and minimal fiber extrusion capability, are still existing in the DIW of fiber composites.

Against this background, this dissertation aims to address these challenges in DIW of fiber-polymer composites and to develop a fundamental understanding of the complex interplay of ink properties, DIW printing process, and printed composite functionalities through testing the following hypotheses:

Hypothesis I: The incorporation of an electric field between the printing nozzle and the substrate induces an electrowetting effect. Such an electrowetting effect enlarges the printable ranges of

materials and the working range of manufacturing process settings, as well as improves the printing accuracy.

Hypothesis II: The addition of water-washable gel changes the storage modulus and loss modulus of the synthetic fiber suspensions in a way that the shear-yielding and shear-thinning properties are enhanced, hence increasing the printability of synthetic fiber inks and allowing for higher fiber contents in the composite.

Hypothesis III: Sonication efficiently removes the primary wall of natural fibers and hence increases the printability of natural fibers in DIW while retaining its mechanical characteristics in the printed composite.

Accordingly, a DIW setup equipped with an electric field is developed. The DIW process without and with the electric field is modeled analytically and validated experimentally. Synthetic-fiber-polymer composite inks and natural-fiber-polymer composite inks are prepared and characterized for DIW printing. Functional parts are printed out of the prepared composite inks, and the printed structures are characterized. The three hypotheses are tested in these research tasks. The findings are beneficial to material science and manufacturing process, enabling significant improvements in DIW of fiber-polymer composites and future applications in functional devices fabrication in the following perspectives:

a) Generalized mappings between the printed feature geometries and process parameters were developed.

b) Influence of liquid ink rheological properties on printing stability was understood.

d) Approaches for modifying synthetic/natural fiber for higher printability were established.

d) Electric-field-assisted and temperature-controlled DIW process planning strategies were developed and evaluated.

e) Novel applications of DIW printed fiber composites were demonstrated.

This dissertation structures as follows: Chapter 1 presents an overview of this dissertation. Chapters 2 and 3 investigate DIW setup, DIW process modeling, and electrowetting-assisted DIW process. Chapters 4 and 5 study the rheological enhancement for synthetic fiber composites and test the electrochemical properties of the printed synthetic-fiber-polymer composites. Chapters 6 and 7 investigate the preparation methods of natural-fiber-polymer composite ink and the mechanical properties of the printed composite. Conclusions are drawn, and future work is proposed in the end.

1. Introduction

Some contents in this chapter have been previously published in (permissions are included in the appendix):

Jiang, Y., Cheng, M., Shahbazian-Yassar, R., & Pan, Y. (2019). Direct Ink Writing of Wearable Thermoresponsive Supercapacitors with rGO/CNT Composite Electrodes. Advanced Materials Technologies, 4(12), 1900691.

Jiang, Y., Plog, J., Yarin, A. L., & Pan, Y. (2020). Direct ink writing of surface-modified flax elastomer composites. Composites Part B: Engineering, 108061.

Jiang, Y., Yarin, A. L., & Pan, Y. (2020). Printable highly transparent natural fiber composites. Materials Letters, 277, 128290.

1.1 Fiber-Polymer Composites Overview

The evolution of fiber-polymer composites began when plastics were first discovered. In the early twentieth century, synthetic plastics, including polystyrene, vinyl, phenolic, and polyester, were found. However, due to their relatively low strength, such plastics could not meet the application's mechanical requirement of high-loading automobile parts and aircraft. Against this background, scientists investigated numerous methods to reinforce their properties.

One of the methods was fiber reinforcement. The first fiber-reinforced composite was developed in 1935, and the significant evolution of fiber composites occurred during World War II due to the high demand for lightweight and strong materials (Bakis et al., 2002). Afterward, in the 1970s, because of the discovery of a huge variety of resins and synthetic fibers, the conventional material usage has been entirely changed by fiber reinforcement (Vinson and Chou, 1975). At that time, synthetic fibers, such as glass (**Fig. 1a**) and carbon fibers (**Fig. 1b**) are the most commonly

used reinforcement material in the polymer composites. The combination of high-strength, high-stiffness synthetic fibers and inexpensive, lightweight polymers led to composite materials with significantly improved mechanical properties and durability better than either of the elements alone. However, the production cost was still very high (Hahn and Tsai, 1980).

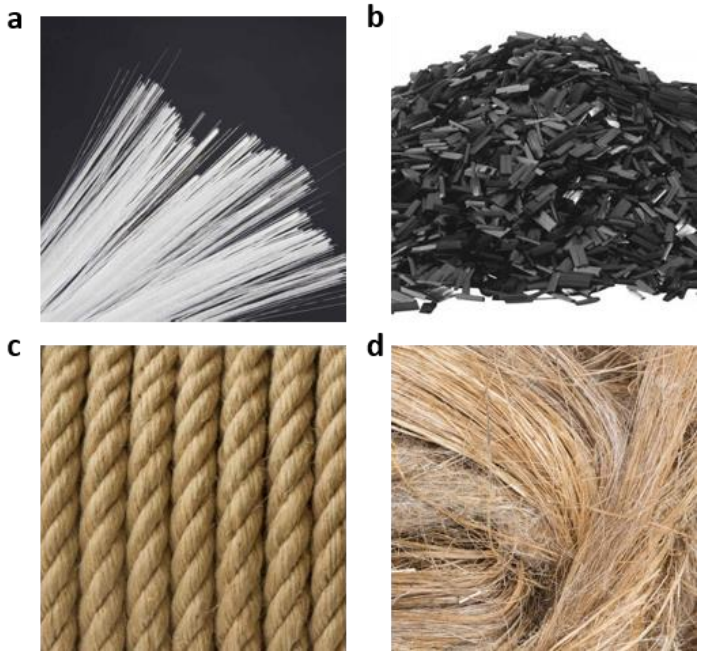

FIG. 1. Typical synthetic and natural fibers. (a) Glass fiber. **(b)** Carbon fiber. **(c)** Jute. **(d)** Flax.

By the early 1990s, the increasing importance was placed on cost reduction for the growth of the fiber polymer composites industry. As the production cost of fiber composites materials decreased and aided by research developments, synthetic fiber polymer composites are now finding a much wider acceptance (Buckley and Edie, 1993). Yet an issue of synthetic fibers is that they are non-biodegradable and can create more environmental issues (Harish et al., 2009). In the search for alternatives and considering the availability, renewability, properties, and cost, natural fibers such as jute (**Fig. 1c**) and flax (**Fig. 1d**) sisal fibers were investigated as replacements of the synthetic fibers for fiber polymer composites (Abilash and Sivapragash, 2016).

To date, many manufacturing approaches, including pultrusion, injection molding, and hot press, have been utilized to fabricate fiber polymer composites in the industry (Bakis et al., 2002). Designed explicitly for fiber polymer composites, the pultrusion process is a highly automated manufacturing method that continuously pulls liquefied fiber polymer composites through a heated curing die to produce high fiber volume profiles with a consistent cross-section (Meyer, 2012). The pulling speed can be as high as 3 m/min, and a 35-50% fiber volume fraction is typically applied. Such a high fiber volume fraction leads to the high strength of the produced composites for civil applications, including bridge decks (Qiao et al., 2000). Recently, woven and braided fiber fabrics have been used to replace conventional fibers to make pultruded parts with further improved mechanical properties in a multidirectional manner (Srisuwan et al., 2014).

In addition to the pultrusion process, there are also compression-based approaches for manufacturing fiber composites, and the injection molding is one of them. During the injection molding procedure, curable matrix and chopped and non-chopped long fibers are first poured into an open mold consisting of upper and lower parts (Rosato and Rosato, 2012). The mixtures are compressed by closing the mold and solidifying the matrix to produce parts in a variety of dimensions. Compared with the pultrusion process, the injection molding can produce parts with higher shape-complexity using customized molds without sacrificing mechanical strength and stiffness (Gupta and Wang, 1993). Similar to the injection molding approach, the hot press process is another compression-based manufacturing technique for fiber polymer composites. The process usually starts from putting a flat sheet of fiber thermoplastic composites into a temperature-controlled press machine with various tray dimensions and geometries (Fan et al., 2009). By melting the thermoplastic and compressing the heated composites via closing the trays, the flat sheet can

transform into the designed shapes based on the tray geometry (Gu et al., 2017). Such compression-based methods are capable of producing complex parts with a constant thickness.

However, the fabricated geometry using the methods mentioned above, is limited to geometries with consistent cross-section or thickness. Due to the limited manufacturing capability, the growing demand for fiber-polymer composites with multiplex geometries, exquisite constructions, and advanced functions underscores the need for advanced manufacturing technologies that can quickly fabricate arbitrary complicated composites structures.

1.2 Additive Manufacturing Techniques for Fiber Polymer Composites

Additive manufacturing (AM), also known as three-dimensional (3D) printing, is a class of manufacturing technologies that fabricate 3D objects from digital models by accumulating materials, usually in a layer-by-layer fashion (Gibson et al., 2014). AM has been developed rapidly since its first emergence in the 1980s (Wong and Hernandez, 2012). According to the types of materials and the related accumulating techniques, AM can be categorized into vat photo polymerization, material jetting, binder jetting, material extrusion, powder bed fusion, sheet lamination, and directed energy deposition (Gibson et al., 2014). Among these AM processes, various principles such as thermal phase change, chemical phase change, and physical binding have been utilized to accumulate different raw materials, including thermal plastics, photosensitive resins, metal powders, and solid sheets. To date, the AM industry continues to grow because of its versatility and low-cost for customization and rapid prototyping for a variety of applications like automotive, aerospace, biomedical, and architectural designs (Haleem and Javaid, 2019).

Despite the AM technique's high design flexibility, most parts produced by AM processes are still limited to single material composition with relatively low mechanical strength, restricting their potential for high-loading structural applications (Ngo et al., 2018). To enhance the mechanical performance of 3D printed parts, various forms of high-strength fibers have been added into the raw materials for different AM processes (Christ et al., 2015). Due to the ease of production, adding short synthetic fibers is most common (Ivey, 2017). By pre-blending raw materials with short synthetic fibers, printable fiber-reinforced composites could be utilized in many AM processes (Wang et al., 2017). This inexpensive process usually makes the final printed part exhibit enhanced tensile properties. Yet many issues, including fiber suspension

inhomogeneity, non-solidification, and undesired voids, are still existing (Parandoush and Lin, 2017).

Long continuous synthetic fibers theoretically have more effective mechanical reinforcement for printed parts (Yang et al., 2017a). Many continuous fiber reinforced composites have been reported using fused deposition modeling and stereolithography (Goh et al., 2019). However, other major AM processes, such as selective laser sintering, have minimal manufacturing capability for such long synthetic fiber-reinforced materials because of the tremendous difficulties in the material preparation step to mix powders and long fibers (Yan et al., 2011). In addition to synthetic fibers, natural fibers can also be utilized in printable composites, while many drawbacks including natural fiber agglomeration and nozzle clogging due to their complicated structures and dramatically varied dimensions have been reported (Balla et al., 2019). To overcome such low printability issue of natural fibers, pre-processing approaches such as surface modification are needed (Jiang et al., 2020a). In this section, we review the strengths and weaknesses of major AM processes in composite preparation and printing, including fused deposition modeling, stereolithography, selective laser sintering, and direct ink writing.

1.2.1 Fused Deposition Modeling

Fused deposition modeling (FDM) is a popular extrusion-based additive manufacturing (AM) technique, widely used for fabricating plastic parts with advantages including low cost, ease of operation, and office-friendly machine design (Gibson et al., 2014). An FDM printer usually includes thermoplastic filament, feeding roller, temperature-controlled liquefier, printing nozzle, and building platform. During the FDM process, the plastic filament is fed into the heated liquefier by the driver gear's feeding pressure. Parts are fabricated by heating the filament to the glass

transition state and then extruded through the nozzle to the platform in a layer-by-layer infilling way (Boparai et al., 2016). By adjusting the process parameters such as extruding speed, liquefying temperature, and infilling ratio, parts with various dimensions and structures can be built using thermoplastic including acrylonitrile butadiene styrene (ABS), nylon polylactic acid (PLA), polypropylene (PP), and polyether ether ketone (Patel et al., 2012).

To further improve the mechanical properties of printed parts from the FDM process, fiber reinforcement has attracted tremendous attention (Ning et al., 2015). Discontinuous synthetic fibers in diverse sizes have first been investigated for the FDM techniques, including carbon fiber, single-walled carbon nanotube, multi-walled carbon nanotube, glass fiber, and nylon fibers (Parandoush and Lin, 2017). Natural fibers such as Harakeke and Hemp have also been utilized as reinforcement to improve the mechanical properties of printed parts (Mohan et al., 2017). The reinforcement is more effective along the printing direction because discontinuous fibers tend to be aligned by the shear force within the nozzle during extrusion.

It has been reported that the reinforcement performance is dependent on the fiber loading. Both the tensile strength and the elastic modulus of the printed part tend to increase with fiber loading increased (Zhong et al., 2001). Although discontinuous fibers are relatively simple to be processed by FDM, as they can be extruded using a standard filament form, many limitations, like undesired porosity and voids, have been reported (Tekinalp et al., 2014). Specifically, such porosity and voids caused by the addition of fibers can form in between the extruded fiber composite filaments, resulting in delamination and decreased tensile strength.

As opposed to discontinuous fiber reinforcement, continuous fiber-reinforced composites, including long carbon, glass, and Kevlar fibers, have been studied in the FDM technique. To date, the printing process for such continuous fiber can be done by modifying the printing head in the

following ways: a) modifying the filament using continuous fiber before extrusion (Zhong et al., 2001); b) in situ coating using molten thermoplastic onto continuous fibers at the nozzle (Melenka et al., 2016); c) adding the continuous fiber as a secondary feedstock (Gardner, 2016). In a), for example, continuous glass fibers can pass through the dissolved ABS to create printable continuous fiber-reinforced composites for FDM. In b), fibers are fused into the molten thermoplastic filament within the nozzle, and the movement of melted thermoplastic for extrusion can draw them through the nozzle. In c), continuous fiber bundles are pre-impregnated with thermoplastics such as nylon before extruding from a nozzle. Compared with pure plastic parts, the parts reinforced by such continuous fibers show an as high as five folds improvements in tensile strength (Akhoundi et al., 2019).

Nevertheless, similar to discontinuous fiber, continuous fibers can also cause nozzle clogging. The nozzle clogging can be potentially solved by creating an additional laying mechanism which encapsulates long fibers by the extruded thermoplastic (Saari et al., 2015). Although both continuous and discontinuous fiber-reinforced filament can significantly improve the mechanical properties, the printed composites are limited to plastic-based raw materials (Van Der Klift et al., 2016). It is a grand challenge to remove such a plastic matrix to increase the fiber content to manufacture advanced products for fiber-centered applications.

1.2.2 Stereolithography

Stereolithography (SL) process is also a popular AM technology for photosensitive polymer printing. The typical SL system is composed of a liquid resin vat, UV projector, building platform, and linear stage (Gibson et al., 2014). In the SL process, the liquid photosensitive polymer is cured through the light irradiation, which provides the amount of energy needed to

induce a curing reaction, forming a highly cross-linked polymer (Bártolo, 2011). In general, parts fabricated by SL exhibit relatively weak mechanical properties, which limits their applications as functional elements under high loading circumstances (Dulieu-Barton et al., 2000). Adding fiber reinforcement to the photo-curable resin is beneficial to increasing the mechanical strength (Cheah et al., 1999). To date, both continuous fibers and discontinuous fibers have been used as reinforcement for photosensitive polymers in SL.

A wide range of discontinuous fibers and other fillers, including silicate dioxide (Gurr et al., 2008), graphene oxide (Chiappone et al., 2017), carbon black (Chiu et al., 2015), ferromagnetic fibers (Lu et al., 2018), glass fiber (Cheah et al., 1999), and carbon fibers (Yang et al., 2017b), have been utilized to create reinforced photosensitive polymers in SL. The most commonly used method to prepare such composites is premixing the fillers and photosensitive polymer. Other additives might also be needed to stabilize the suspension and work as a coupling agent between the added fillers and the matrix. Since the fibers are usually premixed, their orientations are random, causing the potential need for extra steps to align the fibers in the photosensitive polymer (Sakly et al., 2014). It has been reported that the tensile strength, flexural strength, Young's modulus, and hardness can be increased upon reinforcement (Cheah et al., 1999).

On the other hand, the SL of continuous fibers reinforced composites has been demonstrated by incorporating fiber-laying mechanisms (Gupta and Ogale, 2002). Such continuous fiber-reinforced parts showed 2 to 3 times improvement in the tensile strength than the pure resin (Karalekas and Antoniou, 2004). The amount of fiber loading is lower than 20%, restricting their full potential for mechanical reinforcement purposes.

However, there are numerous drawbacks associated with the addition of fibers into the photosensitive polymer. The fiber suspension can cause light to scatter, weakening the UV

penetration depth and the lateral printing resolution. Regions of the liquid resin covered by fillers can remain uncured (Karalekas and Antoniou, 2004). For example, it was estimated that 25% of resin remains uncured when using carbon fibers as reinforcement, mostly inside the carbon fibers. To overcome this issue, more protracted irradiation and higher laser power are necessary (Salmoria et al., 2009). In terms of the influence of fibers on the rheological properties, the viscosity increased as significant volume fractions of fibers added, degrading the liquid resin flow in the vat (Zak et al., 2000). One way to address this problem is the fiber surface coating, which can significantly reduce the viscosity, allowing the processing of resins with relatively high fiber loadings.

1.2.3 Selective Laser Sintering

Selective laser sintering (SLS) is a powder-based AM process. The typical SLS system consists of a laser beam, powder bed, powder roller, and powder supply. In the SLS process, the laser scans the powder bed and sinters powders to form a 3D object in a layer-by-layer way. Different types of powders, including wax, ceramics, metals, and polymers, have been investigated as feedstock in SLS (Gibson et al., 2014). More specifically, this process can be categorized into the following categories: a) full melting; b) solid-state sintering; and c) liquid phase sintering. In full melting, the entire melting process fully melts the powder, and the printed part exhibits comparable properties of traditional bulk material (Zeng et al., 2012). It can be applied to a wide variety of powders, while the processing time is relatively long. Solid-state melting is a thermal process that works at temperatures between 50% to 100% of the material's melting temperature. In liquid phase sintering, the binder material usually becomes liquefied by heating, while structural material remains solid during the process.

Fiber reinforcements for SLS-fabricated parts are mostly reported in the form of short discontinuous fibers to enhance the mechanical properties. Carbon nanotube (Bai et al., 2014), carbon black (Athreya, 2011), glass beads (Chung and Das, 2006), and SiC (Gill and Hon, 2004) have been demonstrated, and matrix materials utilized are usually the thermoplastics. Researchers investigated the mixing methods for such fiber-powder composites. Many approaches, including mechanical and melt mixing (Gill and Hon, 2004), fiber pre-coating (Goodridge et al., 2011), and surfactant-based techniques (Chunze et al., 2009), have been demonstrated to improve the homogeneity of the composites.

Although adding reinforcement results in improved tensile properties, numerous weak interface issues due to the undesired porous structure, and the poor adhesion between fiber and powders are also observed (Goodridge et al., 2011). To overcome the adhesion issue, it was found that increasing the laser intensity is beneficial to lower the viscosity of the composite and to enhance the surface adhesion. However, a further increase in the laser intensity and power can degrade the polymer matrix's mechanical properties due to the decreased molecular weight (Arai et al., 2017).

1.2.4 Direct Ink Writing

As a versatile AM technique, direct ink writing (DIW) was initially invented for fabricating 3D functional structures (Gratson et al., 2004). The process employs computer-controlled translation stages, which move an ink deposition nozzle to create materials with 3D architecture in a droplet-by-droplet or filament-by-filament way. A wide variety of applications, from flexible electronic fabrication to soft functional tissue printing, has been demonstrated during the past twenty years (Rocha et al., 2020). Compared with other major AM techniques such as FDM, SLA, and SLS, DIW

widens the printable material range and achieves a higher manufacturing flexibility as its inks can be any liquid materials.

The reinforcement in DIW printed parts has been widely reported to enhance the mechanical properties and introduce new functionalities using short fillers, such as magnetic metal particles (Kim et al., 2018), boron nitride (Kemp et al., 2020), graphene (You et al., 2018), carbon nanotube (Chen et al., 2017), and carbon fibers (Raney et al., 2018). Many of these studies involved a relatively high filler loading for creating a filler-dominant structure. For instance, Kemp et al. reported using boron nitride as a filler to enhance ceramic-based composites' rheological properties. The 40 vol% addition of boron nitride can effectively modify the composites' flow characteristics by inducing stronger shear thinning and viscoelastic properties for ceramic structure manufacturing. Chen et al. reported the DIW of planar carbon nanotube-based supercapacitor. They utilized aqueous carbon nanotube solutions as a composite ink of the DIW process. After evaporating the water content of the composite, the fiber loading of the obtained supercapacitor electrode was close to 100%, leading to a highly conductive interface for energy storage purposes. However, the printing resolution was limited to 2-3 mm due to the relatively low viscosity of the composite.

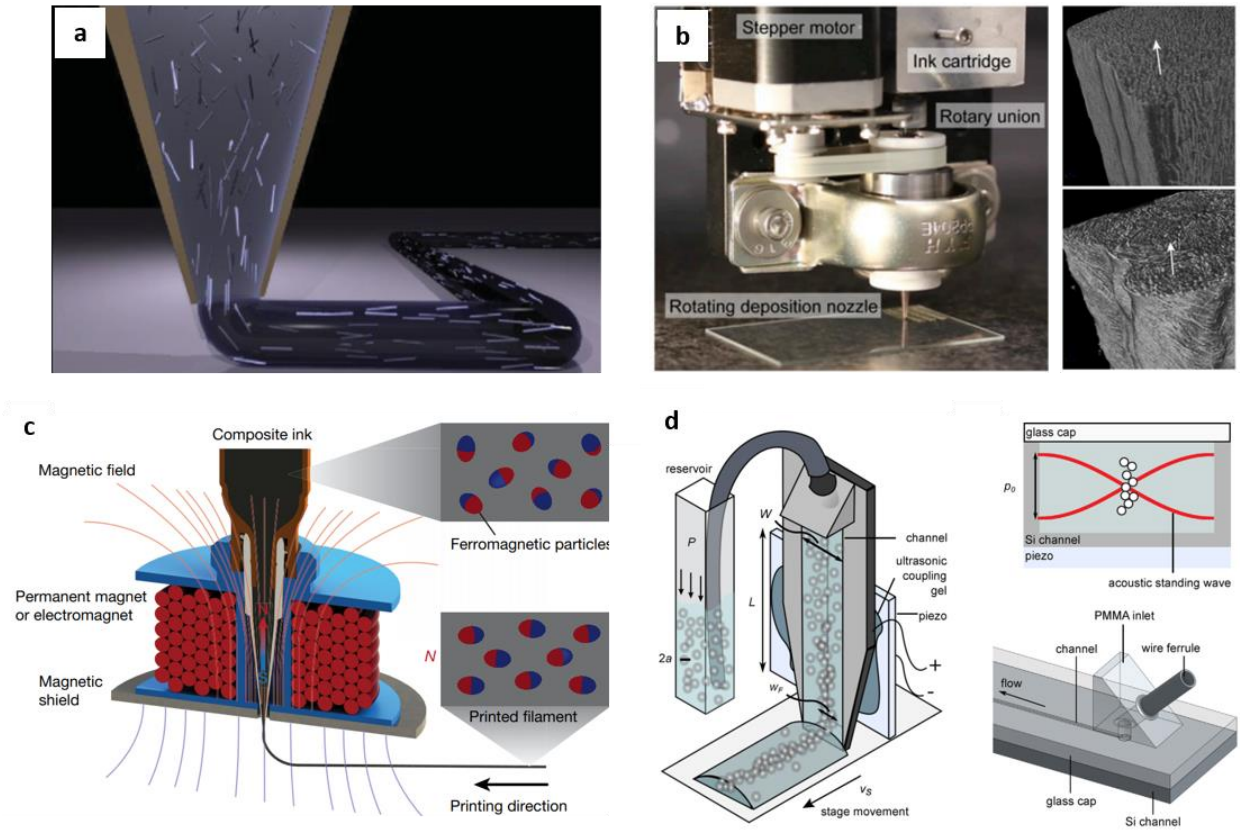

Fig. 2. DIW of Composites. **(a)** Illustration of shear-induced fiber alignments in the DIW process (Compton and Lewis, 2014). Reproduced with permission. **(b)** Rotational DIW wiring process for fiber composites with damage-tolerant designs; short carbon fiber embedded in photosensitive polymer; upper-right image: non-rotated, bottom-right image: rotated (Raney et al., 2018). Reproduced with permission. **(c)** Magnetic particle composites printed by a magnetic-field-assisted DIW process; ferromagnetic particles embedded in elastomer matrix (Kim et al., 2018). Reproduced with permission. **(d)** Acoustic-field assisted DIW for anisotropic composites; particles were controlled by acoustic wave (Friedrich et al., 2017). Reproduced with permission.

Interestingly, numerous strategies for controlling the fiber orientation and distribution in DIW have been reported. One example is the well-known shear-induced fiber alignment in DIW, creating aligned fiber morphologies, and significantly enhancing the mechanical properties along the

printing direction (Compton and Lewis, 2014) (**Fig. 2a**). More functionalities using heterogeneous fillers can be achieved by integrating external field control and mechanical movement into the existing process. For instance, based on the shear-induced fiber alignment, Raney et al. demonstrated the rotational DIW of carbon fiber reinforced polymer composites with programmable mechanics using a more than 30% fiber loading (**Fig. 2b**). By integrating a rotational stage into the conventional DIW configuration, the aligned fiber can be decoupled with weakened mechanical properties for damage-tolerant designs (Raney et al., 2018). Kim et al. presented a magnetic-field-assisted DIW process for programmable metal particle composites (**Fig. 2c**). Through controlling the polarity of the electromagnet during the DIW process, the orientation of the printed particles can be locally adjusted to form the pre-programmed shapes under magnetic actuations for soft robot applications (Kim et al., 2018). Friedrich et al. reported an acoustic control mechanism in the DIW process for anisotropic filler distributions (**Fig. 2d**), and the fillers could be distributed at the center of the printed filaments (Friedrich et al., 2017).

However, caused by the high aspect ratio, fibers can induce bundled agglomeration with poor individual fiber dispersion, which highly degrades the liquid flow during the extrusion in DIW. The printability is still limited by many challenges, including the low extrusion-capability of fiber composite inks and geometrical inaccuracy of printed composite parts (M'barki et al., 2017). Many manufacturing defects, including tip clogging, tip fracture, uneven fiber distributions, have been reported in the literature (Tlegenov et al., 2018) and our work (Jiang et al., 2020a). This dissertation focuses on the DIW process and a detailed review of DIW of fiber-polymer composites in the next section.

1.3 Limitations in Direct Ink Writing of Fiber Composites

1.3.1 High-Complexity in Process Planning

In the DIW process, modeling the printed geometry is a grand challenge because of the tip dependence and large variations in DIW systems such as ink properties (Newtonian or non-Newtonian fluids), syringe feeding mechanisms (pneumatic or mechanical), substrate wetting properties, and tip gauges. Mainly, the current modeling methods for printed geometry prediction of extrusion-based additive manufacturing can be classified into the following categories: a) Models originated directly from experimentation. For instance, Boley et al. have developed a printed filament geometry relationship for gallium-indium alloys (Boley et al., 2014). This type of model is highly accurate and reliable, but it can only be applied to specific materials and substrates. b) Models based on complex physics analysis. An example is the generalized dispensing model developed by Zhao et al. Although this type of model is not limited to specific material, these models usually have some parameters that are difficult to be characterized in a DIW system (Zhao et al., 2005). c) Models derived from application-orientated variables. For example, Deng et al. have developed a geometrical ink extrusion model for 3D printed circuits (Deng et al., 2016). Those models are beneficial for specific applications under certain conditions. Yet they are not developed for and cannot be applied to the general DIW process due to a set of assumptions made specifically for the target applications.

1.3.2 Shape Instabilities of Printed Low-Viscosity Liquid

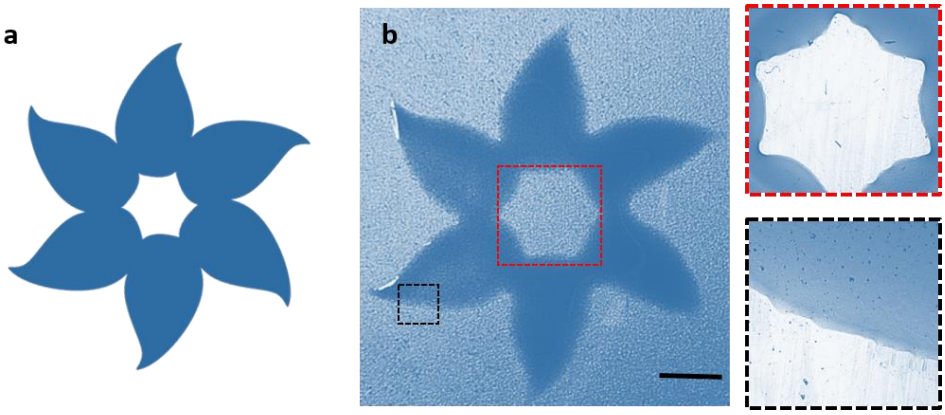

FIG. 3. Low geometrical accuracy of low-viscosity liquid. (a) A flower Design. **(b)** Printed sample showing low geometrical accuracy (photo-sensitive resin on polyimide, scale bar = 4 mm).

Low-viscosity liquids, including commonly used solvents such as acetone and ethanol, have a zero-shear viscosity less than 10^2 Pa·s. Such low-viscosity solvents are usually indispensable in the DIW process. Because of the inherent inappropriate rheology of low-viscosity solvents (Friedrich and Begley, 2018), fiber and fiber composites in DIW studies are limited to simple shapes with low geometry accuracy, causing significantly degraded production quality (**Fig. 3**). In the recently reported literature, the printing resolution of DIW for fiber composite inks is in the range of 0.5 - 2.0 mm, limiting fiber or fiber composite applications at finer scales (Chen et al., 2017).

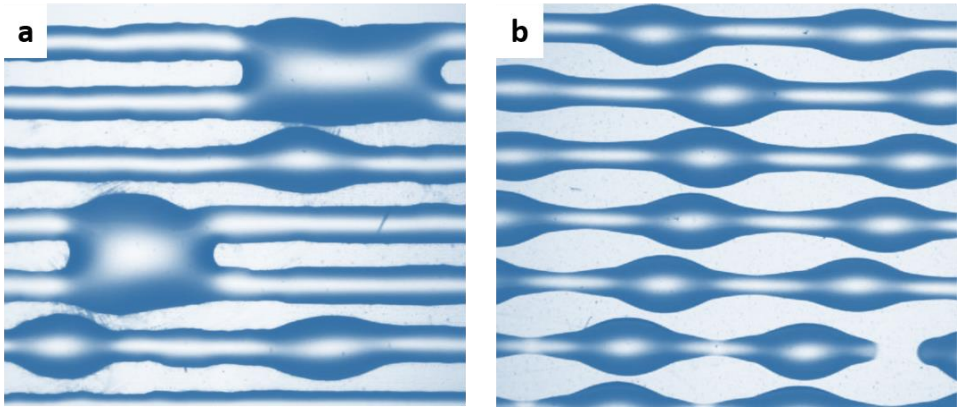

FIG. 4. Shape-instabilities induced by hydrophobic substrate. (a) Printed filaments on glass substrate using 5 wt% PVA aqueous solution. **(b)** Printed filaments on polyimide substrate using 5 wt% PVA aqueous solution.

In DIW, the substrate is usually an integral component of the printed part for functions. A wide variety of substrates have been used in DIW, given wetting properties appropriate for the related inks (Rocha et al., 2020). Yet when the wetting properties of the substrate are not proper, shape instabilities of the deposited ink occur, leading to printing defects or low resolution. This problem is most common in the DIW printing of low-viscosity inks on hydrophobic substrates. Examples of common geometrical defects, such as unstable shape and bulges are shown in **Fig. 4**. Dynamic and localized control of the wettability of substrate is pivotal for addressing those challenges and advancing direct ink writing technologies toward higher resolution and quality, more flexible ink design, and a broader choice of substrate materials (Jiang et al., 2018).

1.3.3 Limited Extrusion-Capability of Fiber Ink

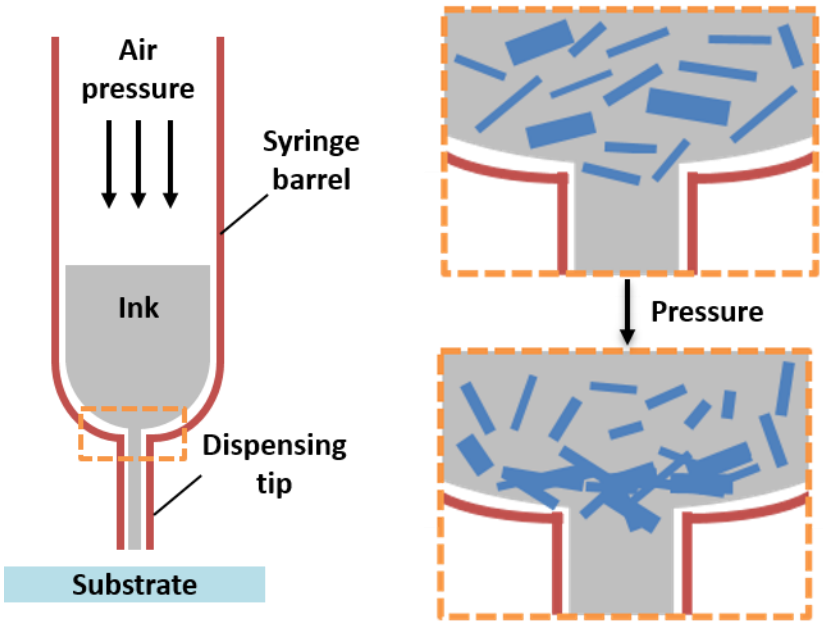

FIG. 5. Tip clogging in direct ink writing of fiber composites.

Recently, the use of natural fibers instead of synthetic fibers in composite materials for AM attracted significant research community attention. These natural fibers exhibit high specific mechanical strength, excellent thermal and acoustic insulation, and good biodegradability (Sanjay et al., 2018). In contrast to relatively rigid synthetic fibers, natural fibers also offer excellent flexibility and softness, making them ideal for many applications such as soft robotics and medical engineering (Ahmad et al., 2015). Nevertheless, printing non-uniform flexible natural fibers by extrusion-based additive manufacturing technologies is challenging due to the poor dispersion of natural fibers with wide variations in fiber dimensions (**Fig. 5**). For extrusion-based AM approaches, the critical prerequisite is the fiber composite ink homogeneity and stability without agglomeration to avoid the nozzle clogging issue (Jiang et al., 2020a).

1.4 Research Hypotheses and Framework

To address the above existing challenges in DIW of fiber composites, we proposed the following three research hypotheses.

Hypothesis I: The incorporation of an electric field between the printing nozzle and the substrate induces the electrowetting effect. The electrowetting effect enlarges the printable material choices and working range of DIW process settings, as well as improves the printing accuracy.

Hypothesis II: The addition of water washable gel changes the storage modulus and loss modulus of the synthetic fiber suspensions in a way that the shear-yielding and shear-thinning properties are enhanced, increasing the printability of synthetic fiber inks and hence enabling productions of functional components with higher fiber contents.

Hypothesis III: Sonication efficiently removes the primary wall of natural fibers and hence increases the printability of natural fibers while retaining their mechanical characteristics in the printed composite.

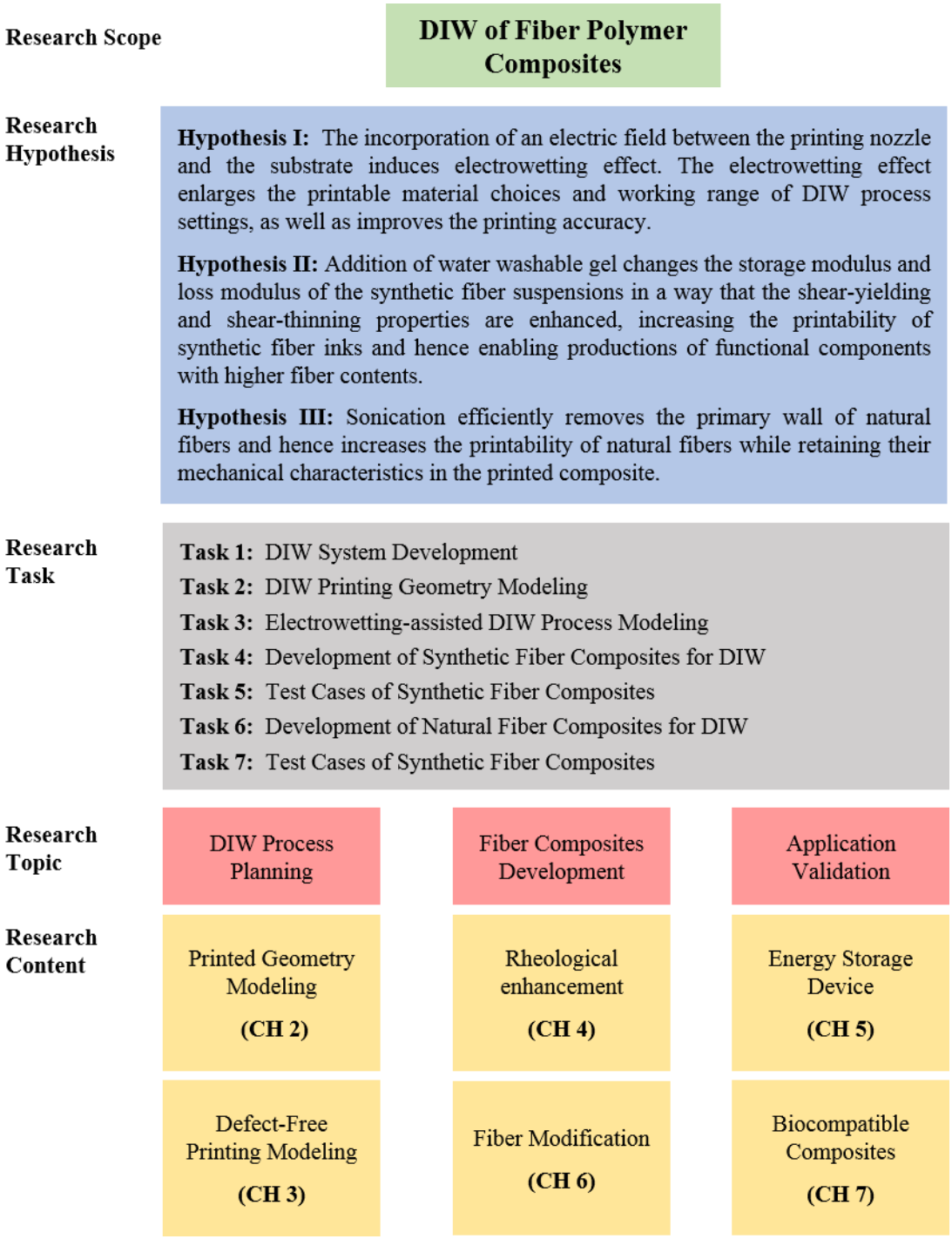

FIG. 6. Research framework

In this Ph.D. dissertation, the goal is to develop printable fiber composite inks and establish effective DIW printing processes for fabrications of fiber composites. Based on the hypotheses, the research framework is designed, as shown in **Fig.6**. A DIW system is developed for experimental investigations. The strategies for preparing printable synthetic and natural fiber composites are established. The process planning in DIW processes, including the geometry modeling, modeling of defect-free printing process parameter settings, electric-field assisted process planning, and temperature-based solidification planning, are investigated. The developed inks and DIW techniques are validated by test cases including fabrications of energy storage devices and sustainable composites.

2. Direct Ink Writing System and Process Modeling

In this chapter, to investigate the DIW process, we first develop the direct ink writing system (**Research Task 1**). Afterward, we prepare the various inks and characterize their rheological properties for testing. A filament geometrical model is derived and validated under various process parameter settings (**Research Task 2**). Some contents in this chapter have been previously published in (permissions are included in the appendix):

Jiang, Y., Plog, J., Yarin, A. L., & Pan, Y. (2020). Direct ink writing of surface-modified flax elastomer composites. Composites Part B: Engineering, 108061.

Jiang, Y., Hu, S., & Pan, Y. (2018). A Normalized Trace Geometry Modeling Method with Bulge-Free Analysis for Direct Ink Writing Process Planning. 3D Printing and Additive Manufacturing, 5(4), 301-310.

2.1 Direct Ink Writing Setup

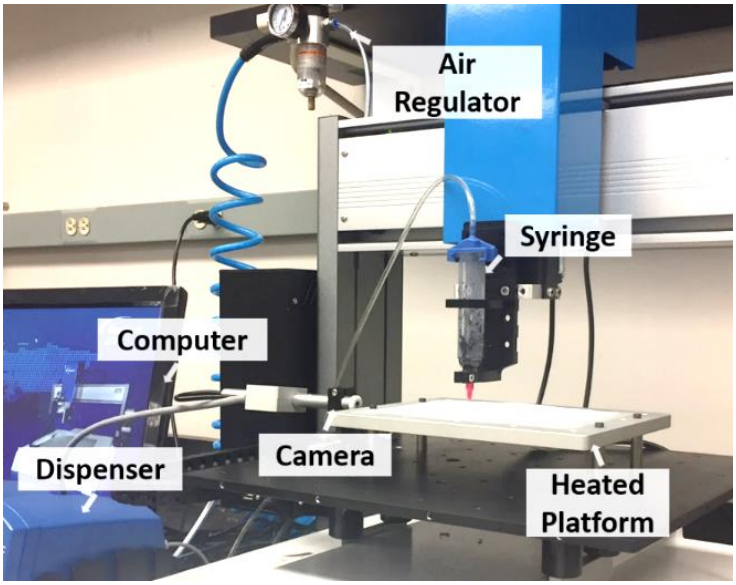

FIG. 7. Direct ink writing setup.

The system used for direct ink writing experiments is shown in **Fig. 7**. It was developed by modifying a dispensing robot (E3V, Nordson EFD). DIW was implemented by extruding inks through dispensing tips to a moving platform in a filament-by-filament and layer-by-layer way. The air pressure and the vacuum level were accurately controlled by dispensers (Ultimus II, Nordson EFD). Filaments were directly written using various stationary blunt stainless-steel syringe tips with inner diameters ranging from 0.10 mm to 0.41 mm and a pump system coupled with a motorized XY stage. The ink was prepared by loading the solution into a 10cc syringe barrel. The experimental setup also consists of a pressure controller that can regulate the ink applied flow rate, a heat-controlled platform, and a CCD camera. The platform temperature was controlled and can be adjusted from 15°C to 135°C. The syringe was mounted to a Z stage. The standoff distance is proportional to the tip gauge for each experiment. A CCD camera for visually detecting such standoff distance is integrated into the system. The CCD camera was also used to monitor the dispensing process in real-time. The stage was reset to the origin point to initiate a printing job. Upon reaching the starting position of a filament, the pre-programmed applied flow rate from the pressure controller began immediately after the start of the platform motion. The pressure controller stops at the end of the filament. An elevated temperature can be applied during the printing, resulting in fast evaporating of the solvent within several minutes.

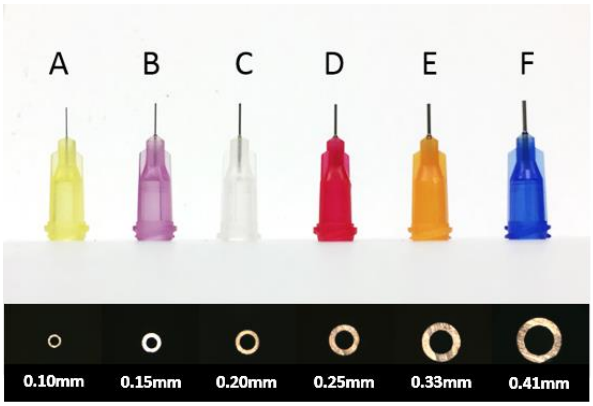

FIG. 8. Dispensing tips in model validation.

In this study, we utilized several dispensing tips (Nordson EFD, RI). As shown in **Fig. 8**, the inner diameters of them are 0.10mm (A), 0.15mm (B), 0.20mm (C), 0.25mm (D), 0.33mm (E), and 0.41mm (F).

2.2 Tested Inks

To test the proposed normalized filament geometry/stability prediction models in the following chapters, we prepared inks using polyvinyl alcohol (PVA) aqueous solutions and photo-curable liquid resin. PVA-I was prepared by adding 6g PVA powder (Mowiol 18-88, Sigma-Aldrich, molecule weight 130,000) to 40 ml deionized water, followed by mixing in a mixer (AR-100, Thinky) for 10 min at 2000 rpm, and storing at room temperature. The ink was prepared by loading the solution in a 10cc syringe barrel (Nordson EFD) and centrifuged at 3,000 rpm for 5 min to degas. The barrel was fitted with various stainless-steel tips with inner diameters ranging from 0.10mm to 0.41mm. PVA-II was prepared by diluting PVA-I using deionized water with a 1:2 dilution ratio. After dilution, the mixture was then mixed for 10 min at 2000 rpm and centrifuged at 3,000 rpm for 5 min to degas. In addition to PVA-I and PVA-II, a flexible resin FLGR02 (Formlabs, MA), is also tested. FLGR02 is an elastomer that allows for bendable or compressible parts. It can achieve 80% elongation, 7.7-8.5 MPa tensile strength, and 80-85A hardness after fully solidified. In the following experiments, to validate that the normalized geometry prediction model is applicable to both Newtonian and non-Newtonian fluids, flexible resin (FR) and PVA-I were tested. To validate the identified bulge-free stability boundary, we tested PVA-II, which is more likely to form a defect due to its relatively low viscosity.

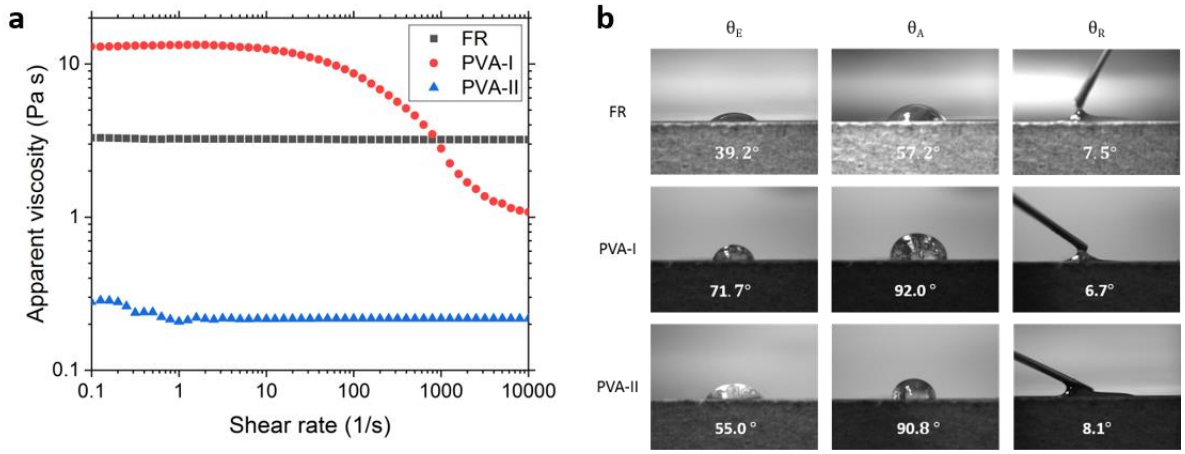

FIG. 9. Rheological properties of inks for model validation. (a) Rheological properties. **(b)** Advancing, receding, and equilibrium contact angles.

The rheological properties of the prepared inks are shown in **Fig. 9a**. PVA-I is shear-thinning, as evidenced by a pronounced decrease in its apparent viscosity from 14.3 Pa·s to 1.8 Pa·s when the shear rate increases from 200 s^{-1} to 2000 s^{-1}. This flow behavior ensures that PVA-I can be easily extruded under moderate pressure. Similarly, PVA-II undergoes noticeable shear thinning, in which the viscosity decreases by half of the magnitude as the shear rate increases from 0.1 s^{-1} to 1.0 s^{-1}. It should be noted that when the shear rate exceeds the threshold 1.1 s^{-1}, PVA-II exhibits Newtonian fluid behaviors with a stationary 0.2 Pa·s apparent viscosity. This is caused by the additional dilution process during PVA-II preparation, in which the added deionized water has a dramatic influence on viscosity. In addition, the Newtonian fluid's behavior of FR was observed, with a measured 3.3 Pa·s apparent viscosity as the shear rate increases from 0.1 s^{-1} to 10000 s^{-1}.

In terms of the contact angles of the tested inks, to differentiate the types of them, we introduce subscripts. In short, θ_A is the advancing contact angle, θ_E is the equilibrium contact angle, and θ_R is the receding contact angle. **Fig. 9b** summarizes the contact angle measurements of FR, PVA-I, and PVA-II, on the polyimide substrate at 25^0C. Although PVA-II is less viscous than PVA-I, it has a similar contact angle as PVA-I. The variations in θ_E between PVA-I 71.7° and PVA-II 55.0° indicates that PVA-II exhibits a slightly higher level of wetting with polyimide. These results suggest medium wettability between polyimide and both PVA-I and PVA-II. In addition, the resulting θ_R was found to be <10° for FR, PVA-I, and PVA-II.

2.3 Normalized Filament Geometry Prediction Model Development

Herein, we introduced a normalized method for modeling the geometry of printed filament in DIW. The normalized model converts conventional dispensing parameters to a dimensionless variable, speed ratio v^*. Our model offered two key advantages over traditional methods. First, the normalized geometry model is applicable to any printable fluids and independent of the tip gauge. Second, parameters in our model are facile to be characterized in mass production.

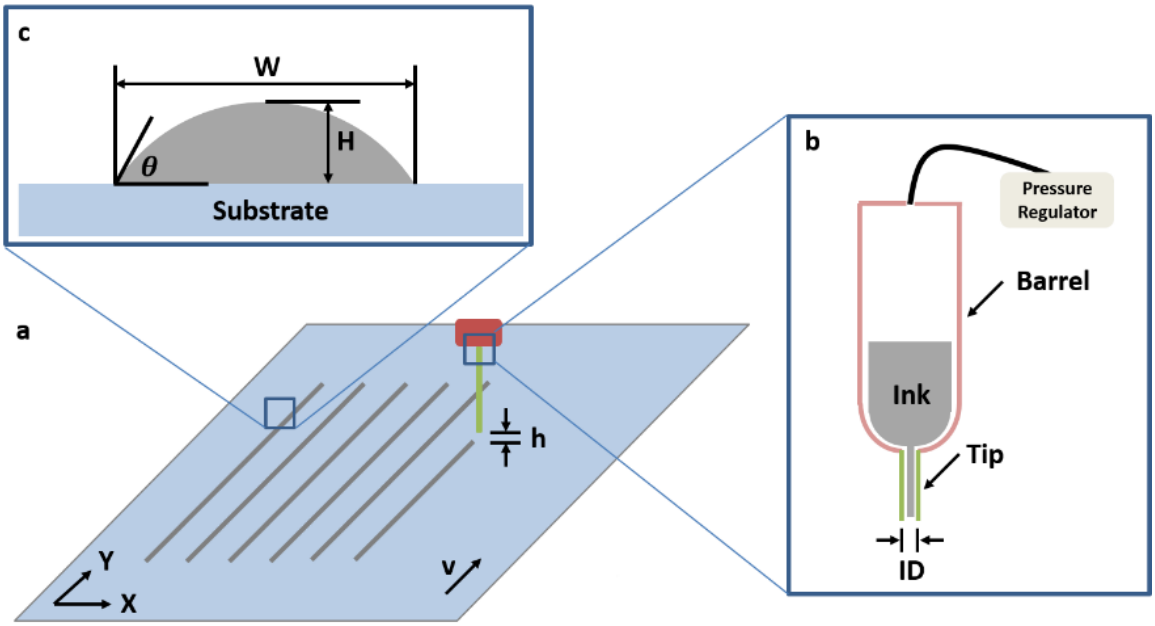

FIG. 10 General direct ink writing system. (a) Schematic drawing of DIW system writing several parallel straight filaments with a substrate speed *v* and a tip standoff distance *h*. **(b)** Schematic drawing of dispensing portion of DIW system: the tip with inner diameter *ID* is attached to the barrel, and the flow is controlled by the pressure regulator. **(c)** Geometry illustration for the cross-section of a written filament.

The typical DIW system consists of a building platform, computer-controlled mechanical stages, and a nozzle-based ink deposition apparatus (Gratson et al., 2004). The liquid ink is directly

extruded from the nozzle by a pumping device onto the building platform in a filament-by-filament way. A general direct ink writing system is illustrated in **Fig. 10a**, the main component in DIW system is the dispensing portion as shown in **Fig. 10b**. In DIW, a three-dimensional object is built by drawing two-dimensional slices line by line and then accumulating layers up to form the designed 3D geometry. Hence, the extruded filament is the building element that directly affects the printing resolution, accuracy, and speed. For a printed filament cross-section, due to extremely small Bond number, the influence of gravity is negligible compared with the surface tension (Duineveld, 2003). Hence, the cross-section can be described as a truncated circle with a width *W*, a height *H*, and a contact angle θ, as demonstrated in **Fig. 10c**. The extruded ink volume ΔV in the time interval Δt is:

$$\Delta V = Q_A \Delta t \tag{2.1}$$

where Q_A is applied flow rate of the ink. The printed filament length in the time interval Δt is:

$$\Delta l = v \Delta t \tag{2.2}$$

where *v* is the substrate speed. Assuming no change in fluid density throughout the syringe and tip, the printed filament cross-section area *A* can be calculated by:

$$A = \frac{Q_A}{v} \tag{2.3}$$

Stringer & Derby have derived a geometry prediction model for inkjet printing (Stringer and Derby, 2010):

$$W_{Inkjet} = \sqrt{\frac{2\pi d_0^3}{3p(\frac{\theta_E}{sin^2\theta_E} - \frac{cos\theta_E}{sin\theta_E})}} = \sqrt{\frac{4A_{Inkjet}}{(\frac{\theta_E}{sin^2\theta_E} - \frac{cos\theta_E}{sin\theta_E})}} \tag{2.4}$$

where W_{Inkjet} is the predicted width of an ink-jetted filament, d_0 is the initial droplet diameter, *p* is the droplet spacing, and θ_E is the ink equilibrium contact angle. The model given by them is a function of the printed filament cross-section area A_{Inkjet}, as illustrated in Equation (2.4). Although

the printed filament in inkjet printing is formed by discrete droplets, it has the same uniform cross-section as printed by DIW. Thus, by substituting A_{Inkjet} with A in Equation (2.3), the width of DIW printed filament W, can be obtained as follows:

$$W = \sqrt{\frac{4Q_A}{v(\frac{\theta_E}{sin^2\theta_E} - \frac{cos\theta_E}{sin\theta_E})}} \tag{2.5}$$

The predicted height of DIW printed filament H could be further calculated by simple cross-sectional analysis:

$$H = \frac{W}{2}(\frac{1}{sin\theta_E} - \frac{1}{tan\theta_E}) \tag{2.6}$$

The printed filament geometry is directly affected by the tip inner diameter. Hence, to develop a model independent of the tip size, we normalized the width W and the height H by dividing them by the tip inner diameter ID. In addition, we defined a dimensionless variable, speed ratio v^*, as the ratio of the speed of the fluids exiting the tip to the substrate moving speed v:

$$v^* = \frac{4Q_A}{\pi ID^2 v} \tag{2.7}$$

As shown in Equation (2.7), the speed ratio v^* replaces conventional dispensing parameters, including applied flow rate Q_A, substrate speed v, and tip inner diameter ID. By rearranging Equation (2.5) and (2.6) using v^*, W/ID and H/ID, the normalized geometry prediction model of DIW can be obtained:

$$\frac{W}{ID} = \sqrt{\frac{\pi v^*}{(\frac{\theta_E}{sin^2\theta_E} - \frac{cos\theta_E}{sin\theta_E})}} \tag{2.8}$$

$$\frac{H}{ID} = \frac{1}{2}(\frac{1}{sin\theta_E} - \frac{1}{tan\theta_E})\sqrt{\frac{\pi v^*}{(\frac{\theta_E}{sin^2\theta_E} - \frac{cos\theta_E}{sin\theta_E})}} \tag{2.9}$$

Basically, they are functions of the speed ratio v^* and the ink equilibrium contact angle θ_E. By normalizing geometry parameters W and H to dimensionless W/ID and H/ID, a single parameter

speed ratio v^* is sufficient to predict the printed filament geometry, if the ink equilibrium contact angle is given. Thus, the normalized geometry prediction model has several significant strengths. First, the model is independent of tip gauge and feeding mechanism. The model also has the capability to estimate the appropriate tip gauge for printing the desired geometry. Lastly, the number of process parameters has been greatly reduced.

2.4 Normalized Filament Geometry Prediction Model Validation

To verify that the model is applicable to both Newtonian and non-Newtonian fluids, we tested FR (Newtonian) and PVA-I (non-Newtonian). Filaments were printed onto polyimide substrate using three different tips for each ink. We measured the printed filament width *W* and height *H*. For each tip gauge, the measured results were further normalized by its corresponding tip inner diameter. The normalized results were compared with the predicted data given by Equation (2.8) and Equation (2.9).

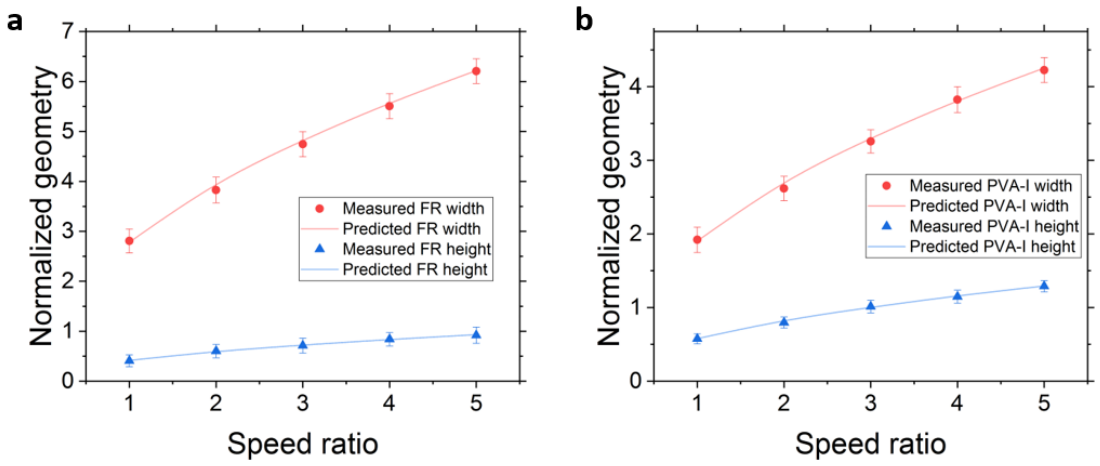

FIG. 11. Normalized filament geometry prediction model validation. (a) FR. **(b)** PVA-I.

The distance between the substrate and the tip is standoff distance *h*. It should be noted that if *h/ID* is too small, the compression caused by the presence of the tip at a lower position will lead to a filament height saturation. On the other hand, a relatively large *h/ID* can result in non-continuous filaments. **Fig. 11a** shows the predicted geometry of FR compared with the measured geometry of filaments written on polyimide with a 0.75 *h/ID*. Similarly, **Fig. 11b** presents the comparison between the predicted geometry of PVA-I and the measured geometry of filaments written on polyimide with a 0.85 *h/ID*. As expected, a relatively small 95% confidence interval

indicates a polynomial effect of v^* on filament geometry. These data all show excellent agreement with the prediction of the normalized geometry model, which validates the effectiveness of this approach for geometry predicting in DIW applications, independent of tip size or ink.

3. Defect-Free Direct Ink Writing of Low-Viscosity Materials

In this chapter, to study the electric field's influence on the geometrical accuracy and stability of the printed filament (**Hypothesis I**), we first investigate the typical defect formation in the conventional DIW process. Afterward, we develop the electrowetting-assisted process (**Research Task 3**) and validate its efficiency in enhancing the filament shape-stability. An image processing method is implemented to characterize filament geometrical accuracy.

3.1 Common Bulge Issue of Low-Viscosity Material in Direct Ink Writing

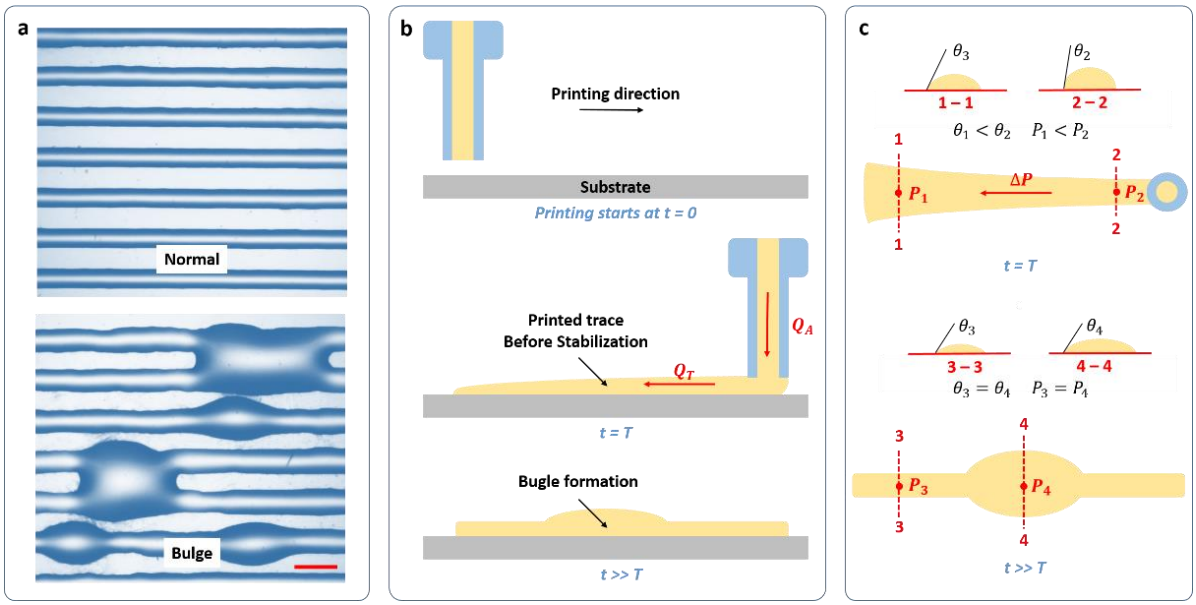

FIG. 12. Analysis of bulge formation. (a) Normal and bulged filaments of 5 wt% PVA aqueous solution printed on glass by DIW. Normal filaments were produced by 18 mm/s printing speed and 5 mm^3/s extrusion rate, while bulged filaments were produced by 12 mm/s printing speed and 5 mm^3/s extrusion rate, scale bar = 1 mm. **(b)** Illustration of bulge formation, side view. **(c)** Illustration of bulge formation, top view.

Low-viscosity liquids characterized by a zero-shear viscosity less than 10^2 Pa s, such as the commonly used solvents, oils, and conductive polymers, show tremendous printing difficulties using the DIW process due to their inherent inappropriate rheology (Friedrich and Begley, 2018). The printed geometry from such materials usually suffers from fluid instabilities, causing critical geometrical defects, including inconsistent filaments and bulges. To understand this type of instability, Friedrich and Begley derived an analytical model from studying the influence of extrusion flow rate, printing speed, and ink contact angles on the printed filament's shape stability and reported numerous drawbacks existing in the current DIW processes for printing low-viscosity liquids.

Specifically, bulges in printed filaments are common issues that can significantly degrade the geometrical accuracy (**Fig. 12a**). To explain the formation of such bulges, we first identify the two types of flows that exist in the DIW process, namely the applied flow Q_A and transported flow Q_T (Duineveld, 2003). Herein, Q_A is defined as the rate of liquid exiting from the dispensing nozzle, which is directly controlled by the pumping system. On the other hand, after the filament was printed onto the substrate, but before stabilization, there is a temporary transported flow Q_T caused by the liquid instability. The transported flow is induced by the internal pressure ΔP from the deviations in dynamic contact angles of the continuous filament. For example, as shown in **Fig. 12b** and **Fig. 12c**, we assume that the printing direction is from location 1 to location 2, the printing starts at t = 0 and ends at t = T. Under these conditions, the contact angles at locations 1 and 2 are denoted as θ_1 and θ_2 with internal pressure P_1 and P_2, respectively. When the dispensing nozzle at location 2 (t = T), the real-time θ_1 is similar to the equilibrium contact angle θ_E due to the settlement in T. On the contrary, the real-time θ_2 is closer to the advancing contact angle θ_A. Such

existing pressure difference ΔP caused by the time-dependently dynamic contact angles can trigger the formation of a bulge under the following circumstance (Stringer and Derby, 2010):

$$KQ_A < Q_T;\ Q_A = Av \tag{3.1}$$

where *K* is a non-zero constant that can be experimentally characterized (Jiang et al., 2018), *v* is the substrate speed, and *A* is the cross-section area of the printed filament. The transported flow rate is given by Duineveld's work (Duineveld, 2003):

$$Q_T = \frac{4S\Delta PA^2}{\eta l_r} \tag{3.2}$$

where *S* is the cross-section coefficient, ΔP is the internal pressure difference between the bulge and the ridge, η is the material apparent viscosity, l_r is the minimum ridge distance. The cross-section area *A* can be substituted by the applied flow rate Q_A and substrate speed *v* (Stringer and Derby, 2010), as shown in Equation (3.3):

$$S = \frac{\theta_E - sin\theta_E cos\theta_E}{8(sin\theta_E + \theta_E)^2} \tag{3.3}$$

The printed filament width *W* in a typical DIW configuration is:

$$W = \sqrt{\frac{4Q_A}{v(\frac{\theta_E}{sin^2\theta_E} - \frac{cos\theta_E}{sin\theta_E})}} \tag{3.4}$$

The dynamic pressure in a printed filament, *P*, with width *W* and real-time contact angle θ can be written as:

$$P = \frac{2\sigma sin\theta}{W} \tag{3.5}$$

where σ is the surface tension of the liquid.

When t >> T, the contact angles along the filament tend to be equivalent, resulting in a significantly reduced internal pressure between the ridge (locations 3, contact angle denoted as θ_3 with internal pressure P_3) and the bulge (location 4, contact angle denoted as θ_4 with internal

pressure P_4). The printed filament eventually reaches its stable state ($P_3 \approx P_4$) by minimizing the surface energy. The dynamic contact angles during the printing process are characterized as:

$$\theta_E < \theta_3 = \theta_4 < \theta_1 < \theta_2 < \theta_A \tag{3.6}$$

To get the upper bound of the internal pressure difference, ΔP is defined as:

$$\Delta P = \frac{2\sigma(sin\theta_A - sin\theta_E)}{W} \tag{3.7}$$

By substituting width W using Equation (3.4), the critical substrate speed for bulge-free printing could be calculated:

$$v_{critical} = f(\sigma, \eta, \theta_A, \theta_E, Q_A) = K^{-\frac{2}{3}} \left[\frac{4S\sigma}{\eta l_r}(sin\theta_A - sin\theta_E)\sqrt{\frac{\theta_E}{sin^2\theta_E} - \frac{cos\theta_E}{sin\theta_E}}\right]^{\frac{2}{3}} {Q_A}^{\frac{1}{3}} \tag{3.8}$$

As shown in Equation (3.8), the critical printing speed for bulge-free filament printing is a function of material viscosity, surface tension, equilibrium contact angle, advancing contact angle, and the applied flow rate.

3.2 Electrowetting-Assisted Direct Ink Writing of Low-Viscosity Liquid

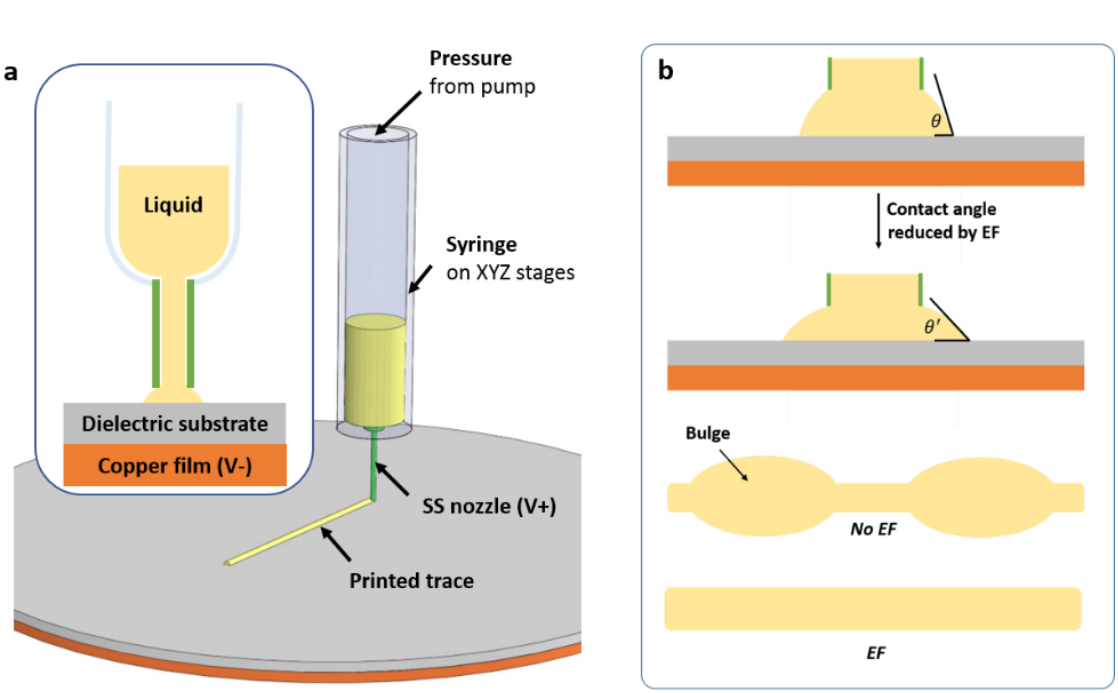

FIG. 13. Electrowetting-assisted direct ink writing. (a) Electrowetting-assisted DIW configuration demonstration. **(b)** Illustration of advancing contact angle influenced by the electric field during printing.

To increase the diversity of the printable materials in DIW by enabling low-viscosity material printing, many novel methods have been recently reported. For example, Skylar-Scott et al. designed a laser-assisted DIW process to print freestanding 3D metal structures with super-high conductivity using concentrated silver nanoparticle composites (Skylar-Scott et al., 2016). By focused infrared laser annealing, the thin liquid metal inks can be rapidly solidified to compensate for the rheological instabilities. Kim et al. used a temperature-controlled platform to instantly cure the low-viscosity elastomer-based ink to fabricate programmable soft structures (Kim et al., 2018). These methods are effective for specific stimuli-curable low-viscosity materials. However, printing a broad type of non-curable low-viscosity liquids in DIW is still a grand and ongoing

challenge. Thickening agents are commonly used as additives to change the rheology of low viscosity liquids to improve their printability. Nevertheless, the additives inevitably degrade the characteristics of the original materials and are not desirable for some applications (Ahmed, 2015).

Against this background, we investigated a novel electrowetting-assisted DIW method for low-viscosity liquid printing. An external electric field is applied between the dispensing nozzle and the substrate, to globally reduce the dynamic contact angles during printing for decreasing the internal pressure along the printing direction. Our proposed method overcomes the common shape-instability issue in DIW of low-viscosity materials. We introduced an analytical model to predict the critical defect-free printing speed and validated the model by test printing PVA-II onto a polyimide film. Additionally, we implemented an image processing method to analyze the geometry of the printed filaments. Compared with conventional approaches, our proposed method significantly widened the working range of process parameter settings with a much higher extrusion throughput and considerable improvement in the geometry accuracy.

When applying the electric field (EF) using electrowetting-assisted DIW configuration (**Fig. 13a**), the real-time contact angles of the liquid during printing can be immediately decreased, which further weakens the impact of the transportation flow (**Fig. 13b**). Under such electric field, the updated real-time contact angle θ' (Kang, 2002) can be modeled as:

$$cos\theta' = cos\theta + \frac{\epsilon V^2}{2\sigma d} \tag{3.9}$$

where ϵ is the electric permittivity of the dielectric layer, V is the electrical potential, d is the thickness of the dielectric layer.

It should be noted that the surface tension of the liquid is also affected by the electric field. Studies have shown that the change in surface tension under such electrowetting configuration is 2% at most **(**Bateni et al., 2004**)**, which is negligible compared with their influence on the

advancing contact angles. To simplify the model, we keep using the non-electric-field-affected surface tension in our study. Taking the effect of horizontal electric field into consideration, the critical printing speed for the bulge-free printing is then updated as follows:

$$v'_{critical} = K^{-\frac{2}{3}}\left[\frac{4S\sigma}{\eta l_r}(sin\theta'_A - sin\theta'_E)\sqrt{\frac{\theta'_E}{sin^2\theta'_E} - \frac{cos\theta'_E}{sin\theta'_E}}\right]^{\frac{2}{3}} {Q_A}^{\frac{1}{3}} \tag{3.10}$$

Here, we define a coefficient to combine parameters related to the inherent liquid properties for simplicity:

$$C_E = K^{-\frac{2}{3}}\left[\frac{4S\sigma}{\eta l_r}(sin\theta'_A - sin\theta'_E)\sqrt{\frac{\theta'_E}{sin^2\theta'_E} - \frac{cos\theta'_E}{sin\theta'_E}}\right]^{\frac{2}{3}} \tag{3.11}$$

The updated critical printing speed for DIW can be re-written as:

$$v'_{critical} = C_E {Q_A}^{\frac{1}{3}} \tag{3.12}$$

3.3 Defect-Free Direct Ink Writing Validation

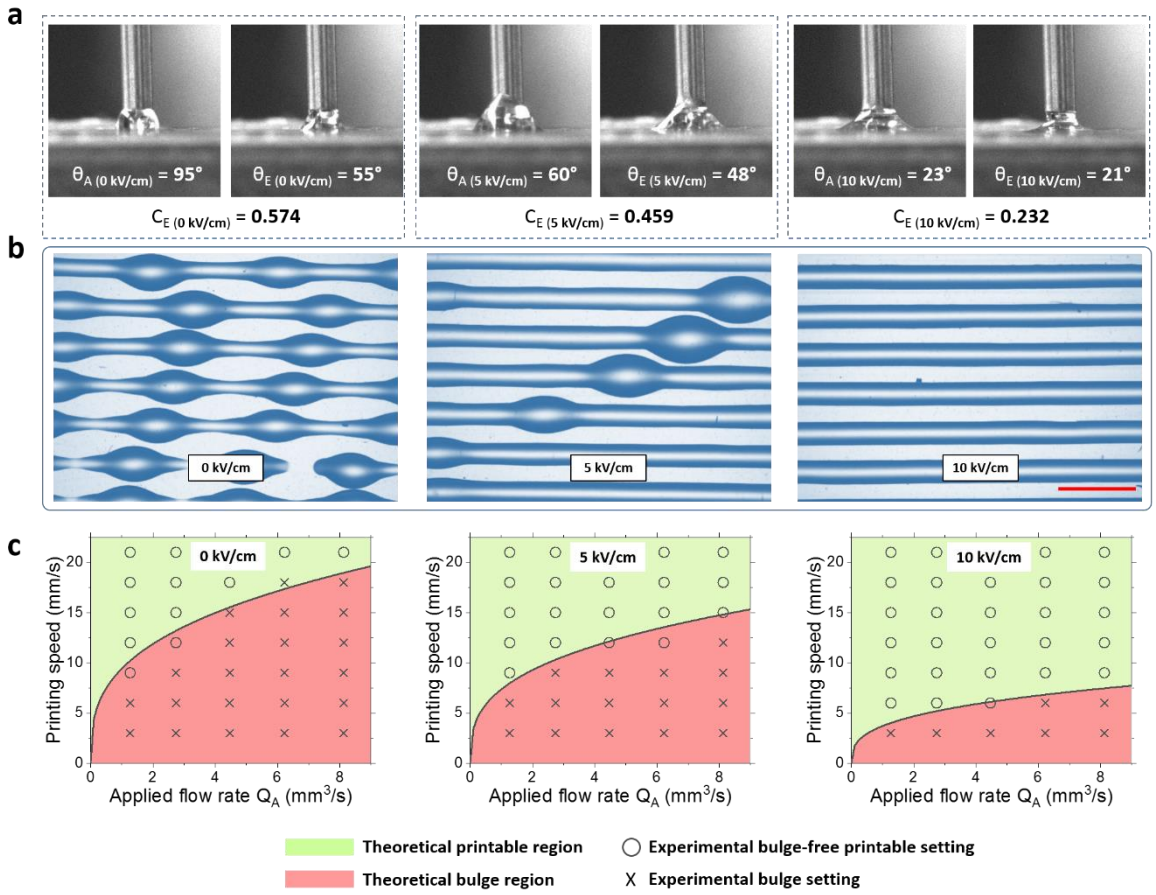

FIG. 14. Contact angles and printable regions under different electric fields. (a) Average advancing and equilibrium contact angles on polyimide under varied EF strength, with C_E characterized. **(b)** Printed filaments under varied EF strength, filaments were printed under 3 mm^3/s applied flow rate using 5 wt% PVA aqueous solution onto polyimide at 9 mm/s printing speed through 23-gauge dispensing nozzle, scale bar = 2 mm. **(c)** Comparisons of theoretically predicted printable regions and experimentally characterized printable regions under varied EF strength.

To investigate the electric field's influence on filament stability, we tested printing PVA-II on the polyimide substrate under various EF strengths. A CCD camera was utilized to capture the dynamic advancing and equilibrium contact angles (**Fig. 14a**). At 0 kV/cm, the average advancing and equilibrium contact angles were 95° and 55°. When there was a 5 kV/cm EF, the average advancing and equilibrium contact angles changed to 60° and 48°. By further increasing the EF strength to 10 kV/cm, they dramatically decreased to 23° and 21°. Based on these measurements, C_E was characterized. C_E decreased from 0.574 to 0.232 $s^{-2/3}$ when the EF strength increased from 0 to 10 kV/cm.

Afterward, straight filaments were printed using a 0.48 mm stainless steel dispensing nozzle through a 3 mm^3/s applied flow rate with a 9 mm/s printing speed. The thickness of the dielectric substrate was 0.3 mm, and the standoff distance was 0.5 mm. As demonstrated in **Fig. 14b**, under 0 kV/cm, we observed periodic bulges on the printed filaments. Such periodicity can be explained by the capillary instability (Schiaffino and Sonin, 1997). When using a 5 kV/cm EF, the impact of the capillary instability was weakened, the number of bulges significantly decreased. Furthermore, by increasing the EF strength to 10 kV/cm, no bulge was observed, validating the feasibility and effectiveness of EF on the printing shape stability improvement.

Using the estimated C_E values, we computed the theoretical printable regions based on Equations (3.10) - (3.12). To experimentally validate the theoretical printable regions, we tested more process parameter settings and examined whether any bulge formed on printed filaments. If no bulge was observed, the process setting was identified as a bulge-free printable setting. Otherwise, the process setting was identified as a non-printable setting. As shown in **Fig. 14c**, the discrete circles marked DIW process settings that generated bulge-free printing results, while the cross marked process settings that generated bulged filaments in experiments. It showed that the

experimental boundaries between the discrete circles (bulge-free settings) and crosses (bulge settings) agreed well with the theoretical boundaries, validating the accuracy of the theoretical geometry model for the novel electrowetting-assisted DIW process. Furthermore, experimental results also validated the theoretical model that the electrowetting effect significantly enlarged the bulge-free printable region of the 5 wt% PVA aqueous solution on the polyimide substrate and increased the printing throughput by 153% (defined as the ratio between applied flow rate and printing speed). Such throughput enhancement is due to the reduced dynamic contact angle during printing, which led to a much less interval pressure and transportation flow along the printed filament. These findings verified the accuracy of the prediction model. They confirmed the effectiveness of our proposed electrowetting-assisted approach on addressing the bulge formation problem in DIW of low-viscosity liquids and increasing the throughput.

3.4 Geometrical Accuracy of Electrowetting-Assisted Direct Ink Writing

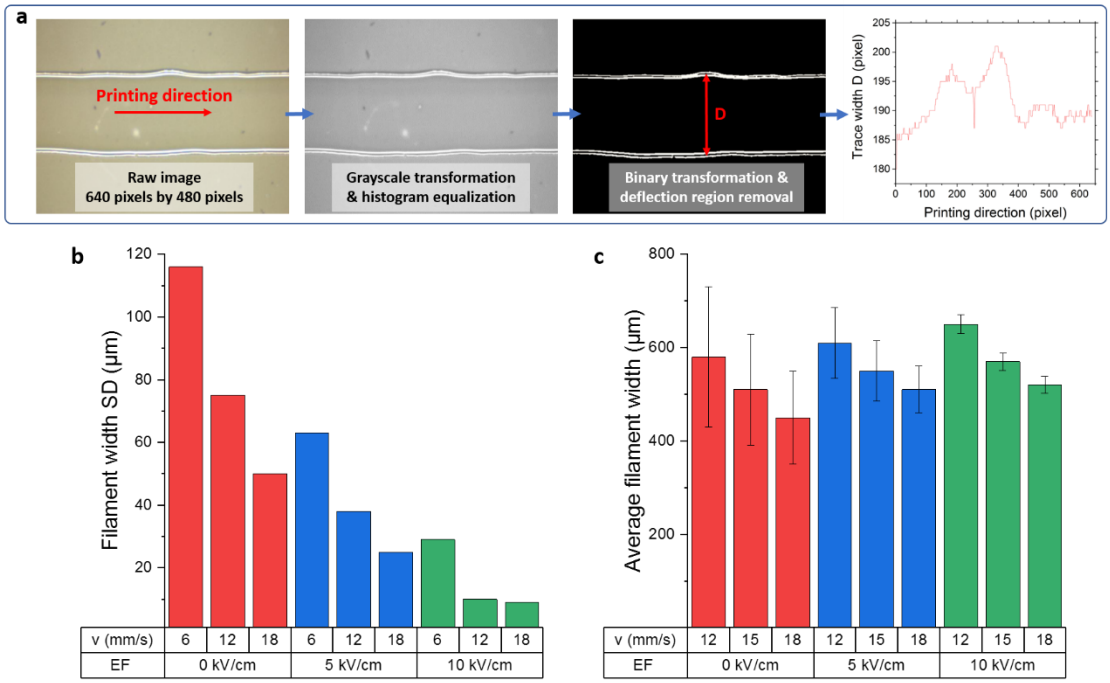

FIG. 15. Geometrical accuracy of electrowetting-assisted direct ink writing. (a) Image processing method for geometrical accuracy analysis. **(b)** Standard deviation of the printed filament's width under varied EF strength and printing speed. **(c)** Average filament width of the bulge-free filaments under varied EF strength and printing speed, 95% CI.

To study the printing quality of the electrowetting-assisted DIW process, we implemented an image processing approach to statistically analyze printed filaments. As shown in **Fig. 15a**, the colored raw image of a printed filament (dimension: 640 by 480 pixels) was first obtained by a microscope (MicroVu Sol). The raw image was then transformed into a grayscale format, and a histogram equalization was conducted to pre-process the image to improve its contrast in MATLAB. The equalized grayscale image was further converted into the binary form and was processed using a median filter (kernel size: 5 to 15) to remove any unwanted light deflection region for the filament width measurement. The filament width at each location along the printing

direction was measured by finding the filament boundary and subtracting the upper and lower bounds in MATLAB. The calculated data for each filament was transformed from pixel to physical size and stored as a vector with 640 elements for statistical analysis.

Using this image processing method, we analyzed the standard deviations of the width of filaments produced at 6, 12, and 18 mm/s printing speeds through a 3 mm^3/s applied flow rate under varied EF strengths (**Fig. 15b**). It should be noted that some of these filaments from relatively slow printing speeds suffered from bulges. As expected, filaments under 0 kV/cm showed the most considerable inconsistency, with an as high as 115 μm standard deviation in width. After using a 5 kV/cm EF, the corresponding standard deviation was reduced by approximately 40-60%. When applying 10 kV/cm EF strength, although filaments printed at 6 mm/s speed still showed a moderate variation (30 μm), the width deviation of filaments printed at higher speeds such as 12 and 18 mm/s is much smaller, down to 9 μm. Higher printing speeds and EF applications enabled the successful printing of bulge-free filaments with consistent widths. For those successfully printed filaments, the average widths were shown in **Fig. 15c** and analyzed with 95% CI. It showed that although high printing speed alone was able to achieve bulge-free filament printing, the within-filament width variation was still considerable. With the application of EF, not only the bulge formation problem could be addressed, but the within-filament width variation was also reduced, enabling a more consistent printing result. In addition, when applying EF, the filament width was slightly increased by 10-20% due to the electrowetting effect, and the increment was proportional to the EF strength. These experimental results validated the effectiveness of our proposed method on improving the printed filament straightness, printing geometrical accuracy, and printing result consistency.

4. Synthetic Fiber Composites Inks

This chapter investigates the development of synthetic fiber composites for high-resolution DIW using CNT-based inks (**Research Task 4**). The influence of water-washable gel on the DIW printability of the composite ink is investigated (**Hypothesis II**). The rheological property, wettability, printability, and the electrochemical performance of the developed synthetic composite inks are studied. Some contents have been previously published in (permissions are included in the appendix):

Jiang, Y., Cheng, M., Shahbazian-Yassar, R., & Pan, Y. (2019). Direct Ink Writing of Wearable Thermoresponsive Supercapacitors with rGO/CNT Composite Electrodes. Advanced Materials Technologies, 4(12), 1900691.

4.1 Development of Washable Gel for Rheology Enhancement

Compared with natural fiber, synthetic fiber composites usually show higher extrusion-capability due to their relatively simple structures and consistent fiber dimensions. In terms of the liquid inks used in DIW, two rheological properties are preferred: the shearing-thinning behavior and the shear-yielding behavior (Smay et al., 2002). The shear-thinning behavior ensures a relatively low pumping pressure when extruding the liquid ink through the nozzle, which effectively prevents nozzle clogging and fracture. The shear-yielding behavior assures the printed filaments' high shape-stability, which is essential for the printed geometry accuracy.

However, not many materials exhibit such rheological behaviors. Low-viscosity liquids, such as the commonly used aqueous polymer solutions for synthetic fiber composites, show tremendous printing difficulties in the DIW process due to their improper rheology (Xie et al., 2014). For example, the current DIW accuracy for aqueous synthetic fiber composites is only approximately 2-

3 mm, limiting the future fabrication of more advanced functional devices. The printed geometry from such low-viscosity liquid usually suffers from instabilities, resulting in geometrical defects (Jiang et al., 2018).

To improve the printability of low-viscosity liquid, thickening agents can be used to adjust the rheology of the liquid. Carbomer is a synthetic polymer of acrylic acid (Singla et al., 2000). It is a commonly used thickening agents that helps control the viscosity/flow of the liquid. It also helps distribute and suspend insoluble solids such as fibers into the liquid. In a water solution at neutral pH, Carbomer behaves as an anionic polymer and it side chains trend to acquire a negative charge. This makes Carbomer polyelectrolytes, with the ability to absorb and retain water and swell to up to three folds of the original volume. Therefore, Carbomer can be used in gel formulations because it creates a colloidal mixture with water, enabling both shear-thinning and shearing-yielding properties of the liquid. On the other hand, the loading fraction of Carbomer into water is typically in the range of 0.1% to 0.5%. Such relatively low loading fraction is beneficial to minimizing the influence of Carbomer content on the fiber composites structure. Also, the addition of Carbomer can be removed by flowing water, resulting in a high fiber content of the composites.

Against this background, we developed a gel to enhance the rheology of synthetic fiber composites using Carbomer for high-resolution DIW. The printing resolution was improved by more than an order of magnitude. Such fully washable gel is beneficial to fiber-centered applications. To prepare the gel, 0.5 g Carbomer 940 was first added into 100 g deionized water. The mixture was then stirred at 200 rpm overnight. To adjust the pH of the mixture to neutral, we gradually added NaOH aqueous solution to the mixture. The obtained gel can be used to mix with synthetic fiber composites to enhance the printability. After the printing process, the printed fiber composites were dried and cleaning through the flowing water to remove the Carbomer and NaOH content.

4.2 Synthetic Fiber Composites Preparation

Using the developed gel, we reported the development of high-performance electrode fabrication for energy storage devices. Carbon nanotube (CNT), as a low-dimensional nanofiber discovered in 1991, exhibits diverse and unique properties, including super-high stiffness and excellent conductivity (Dresselhaus et al., 2000). Accordingly, CNT-reinforced composites have been demonstrated in numerous fields, such as mechanical reinforcement, optical devices, and electrical/thermal enhancement. Specifically, CNT is an ideal electrode material for next-generation high-performance energy storage devices due to its high internal surface area. Many novel designs, including flexible, wearable, self-protective supercapacitors and batteries, have been reported.

To further improve the electrode performance, recent studies have reported the benefits of adding reduced graphene oxide (rGO) to CNT to form a composite structure (Cui et al., 2015). The conductive CNT interconnects the adjacent rGO sheets, inducing a well-linked solid-state electrode. The ionic conductivity is hence enhanced. To identify the proper preparation of hybrid CNT and rGO composite ink, samples labeled as CNT-10%, CNT-25%, and CNT-50% were tested with rGO and CNT weight ratios of 9:1, 3:1, and 1:1, respectively. 2 mg/ml CNT and rGO aqueous solution were first prepared separately.

Based on the washable gel, to prepare the synthetic fiber-based composites for DIW, 2 mg/ml CNT and rGO aqueous solution were first prepared separately. Large surface area SWNT (purity>95%, specific surface area>1075 m^2/g) was purchased from Timesnano (product code TNSAR, Chengdu, China) and used as received. CNT (100 mg) and sodium dodecyl sulfate powder (350 mg, >99.0%, Sigma-Aldrich) were added into deionized water (50 mL). Reduced graphene oxide (BET surface area: 422.69 – 499.85 m^2/g) was purchased from Graphenea (product code rGO, Spain) and used as received. rGO (100 mg) and sodium dodecyl sulfate powder (350 mg) were added

into deionized water (50 mL). Then, both solutions were mixed (AR-100, Thinky) at 2000 rpm for 15 min, followed by 1-hour probe sonication (QSonica Q500, 70% power) to uniformly disperse active materials in the rGO solution and CNT solution, separately. According to the desired ratio, a total volume of 2ml rGO and CNT solution, together with 0.8ml washable gel, were mixed at 2000 rpm for 3 min.

4.3 Rheological Properties of Synthetic Fiber Composites

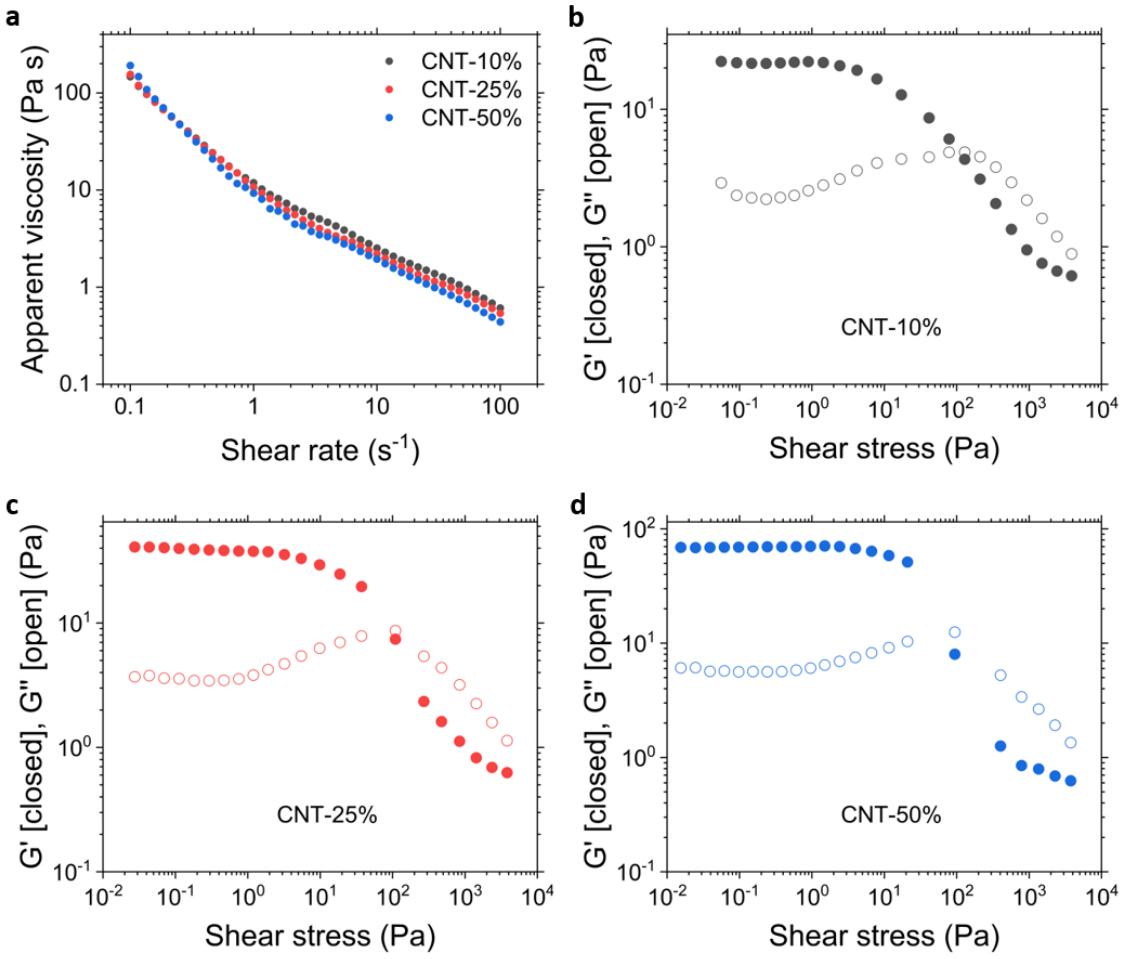

FIG. 16. Synthetic fiber composites rheology characterization showing strong shear-thinning and shear-thinning behaviors. (a) Apparent viscosity characterization. **(b) - (d)** Modulus characterization.

To validate the rheological properties of the prepared synthetic fiber-based composites, the samples were first characterized using a rotational rheometer (Kinexus Ultra+, Malvern) equipped with a 25-mm-diameter plate geometry. The plate geometry is supported by a virtually frictionless air-bearing, driven by an ultra-low inertia motor, coupled to an ultra-high precision position encoder. In all experiments, the inks were equilibrated at 25^{0}C for 15 min before testing. The

sample was then loaded into the gap of a fixed substrate and the plate geometry. In this test, the rheological characteristics of the sample can be determined by rotating, based on the controllable motor torque. The test runs a logarithmic sequence of shear rates and measures the apparent viscosity with a 25^0C testing temperature for each material.

The apparent viscosity of the three inks is characterized (**Fig. 16a**). They demonstrate a similar intense shearing thinning behavior, which ensures a stable and consistent printing process of DIW. The measured apparent viscosities mainly decrease from 106.5 to 0.5 Pa s when the shear rate varies from 0.1 to 100 s^{-1}. The shear-thinning property of our CNT-based ink allows a stable extrusion from the dispensing tip without clogging. **Fig. 16b-d** show the storage modulus (G') and loss modulus (G'') as a function of shear stress. The prepared composites are elastic-like solids (G' >> G'') with respective G' values of 40.9 Pa that flow when its shear yield stress value of 109.68 Pa is exceeded. Once the ink exits the nozzle and returns to a zero-shear condition, it rapidly solidifies and retains its filamentary shape.

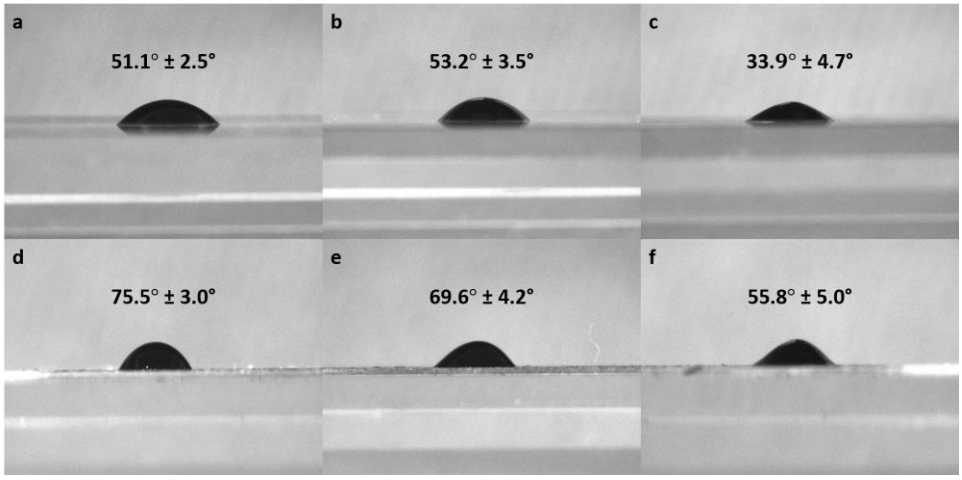

FIG. 17. Synthetic fiber composites contact angles. (a) CNT-10% onto stretchable film. **(b)** CNT-25% onto stretchable film. **(c)** CNT-50% onto stretchable film. **(d)** CNT-10% onto dried CNT-10%. **(e)** CNT-25% onto dried CNT-25%. **(f)** CNT-50% onto dried CNT-50%.

Afterward, equilibrium contact angles of the inks are captured using a high-definition greyscale camera (CMLN-13S2M-CS, Point Grey Research Inc) with a 35mm lens at 25°C. **Fig. 17** shows the summary of the measured contact angles of the inks onto stretchable film and thoroughly dried inks. It should be noted that the equilibrium contact angle of the newly deposited ink onto a thoroughly dried ink ranges from 55° to 70°, indicating the previous dried layer can evenly stack a newly deposited filament.

4.4 Printability of Synthetic Fiber Composites

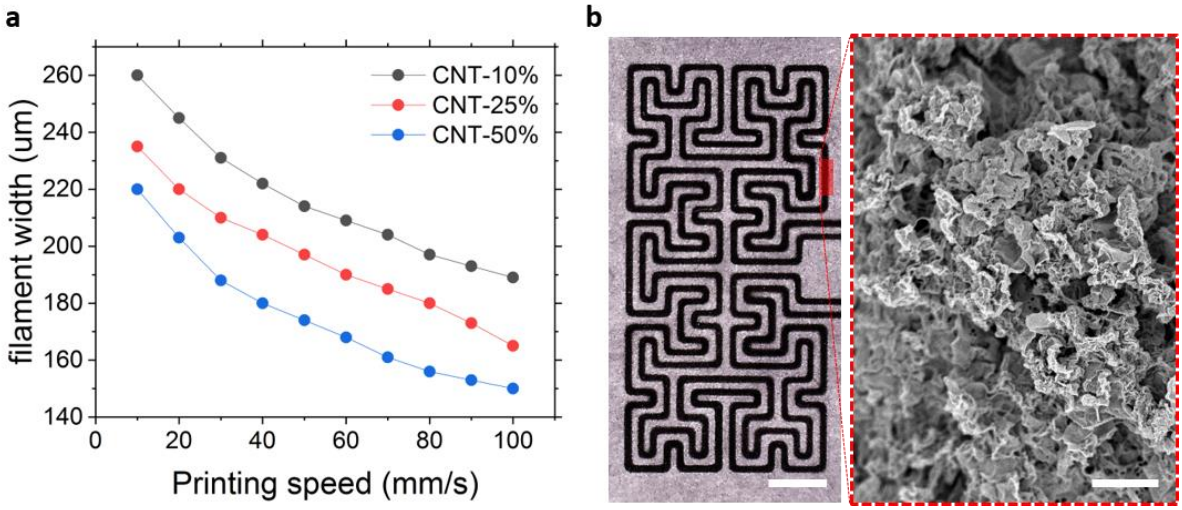

FIG. 18. Printed synthetic fiber composites geometrical evaluation. (a) Measured filament width at various printing speed. **(b)** Printed pattern demonstration, left scale bar = 2 mm, right scale bar = 3 μm.

To investigate the printing accuracy, the filament width printed at 3.0 psi through a 100 μm inner diameter tip at various speeds is characterized (**Fig. 18a**). By varying the print speed, the printed filament geometry produced from three inks can be adjusted. As demonstrated in **Fig. 18b**, we tested printing a complicated pattern using CNT-25% ink. The printing resolution of the electrodes in this study can be smaller than 150 μm, which is among the best in the recently reported planar carbon-based energy storage devices fabricated by the DIW technique (Valentine et al., 2017). The superior printability is beneficial from strong shear-thinning and shear-yielding behaviors by adding the prepared washable gel. As demonstrates by the scanning electron microscopy (SEM) images of the printed sample, no residue from the gel was observed after drying and washing.

4.5 Electrochemical Performance of Synthetic Fiber Composites

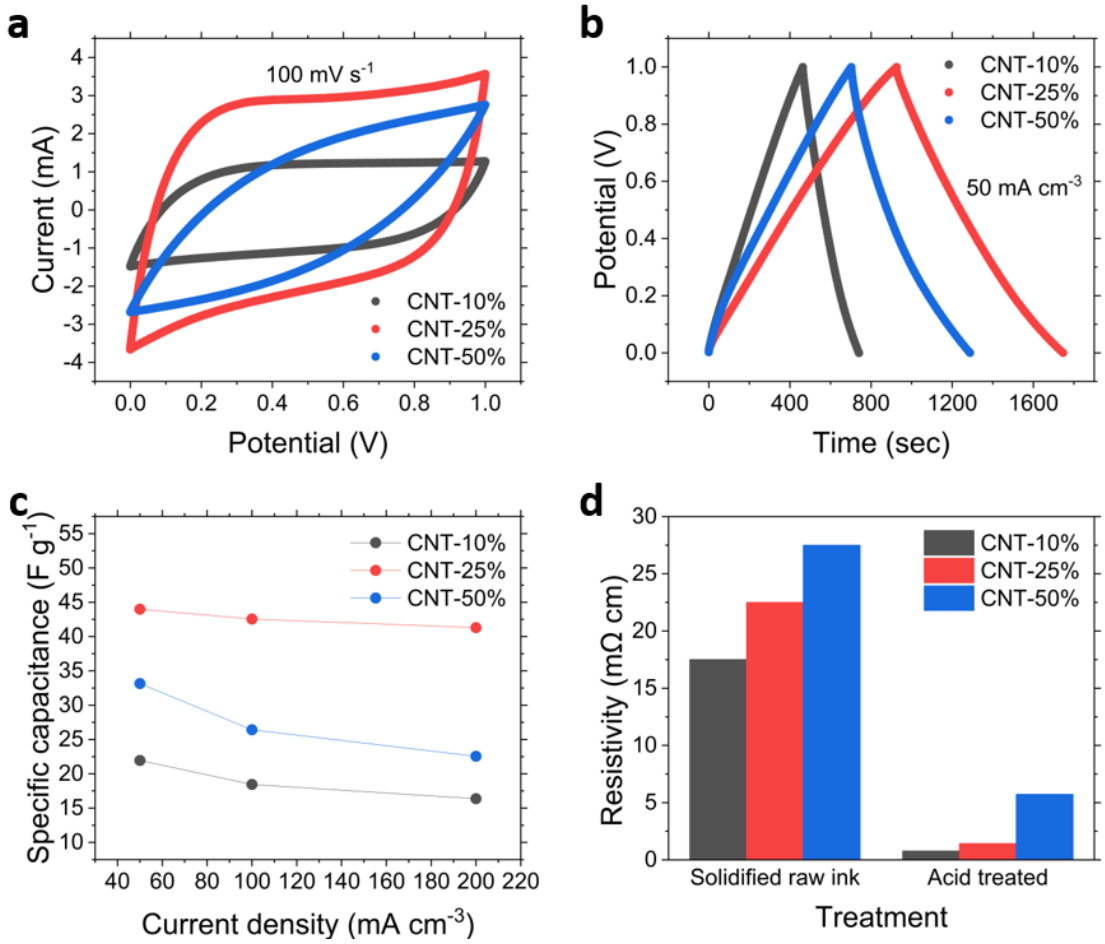

FIG. 19. Electrochemical characterizations of synthetic fiber composites. (a) CV profiles. **(b)** Galvanostatic charge/discharge profiles. **(c)** Specific capacitance at various current densities. **(d)** Resistivity measurements.

In addition, to study the influence of the CNT/rGO ratio on the electrochemical performance, we fabricated sandwiched SCs with 15 mm by 2.5 mm electrodes (175 µm gap between electrodes) using the DIW technique. A 0.25 mm inner diameter stainless steel tip was used to print CNT-10%, CNT-25%, and CNT-50% inks onto the glass substrate. The standoff distance was 0.12 mm. The printing speed was 20 mm s-1, and the input air pressure was 2.0 psi.

After depositing a single 20 mm by 5 mm rectangular layer in an "S" path, the setup stood by for 3 min to solidify fully at 75°C. A total of 25 layers were printed onto the substrate. The calculated active material density was 5 ug mm^{-2}. Afterward, the printed pattern is soaked in nitric acids (Sigma-Aldrich, 70%), followed by water/acetone cleaning before drying in an oven at 65°C. Electrodes are separated by 175um thick PET films. The electrolyte was then filled in between electrodes.

Subsequently, we tested their performance in aqueous LiCl electrolytes by using cyclic voltammetry (CV) and galvanostatic methods with a potential range from 0 to 1 V (**Fig. 19a** and **Fig. 19b**). At 100 mV s^{-1} scan rate during the initial CV cycles, the measured cycling current remained within a roughly equivalent level, indicating the absence of the electro-activation (Pech et al., 2010). It implies that the intercalation of CNTs in the printed rGO/CNT ink effectively alleviates rGO sheet restacking. On the other hand, the CV tests indicate that the CNT-25% ink exhibits a superior power handling capability than CNT-10% and CNT-50%. Such observations are also verified by the results from the galvanostatic test at 50 mA cm^{-3}. The specific capacitances at various current densities are summarized in **Fig. 19c**. The resistivity of thoroughly dried electrodes is measured from 6 μm printed films (**Fig. 19d**), which is adequate for the formation of a conductive thin film. After nitric acid treatment, the resistivity is dramatically reduced by removing surfactants and impurities.

4.6 Thermal Stability of Synthetic Fiber Composites

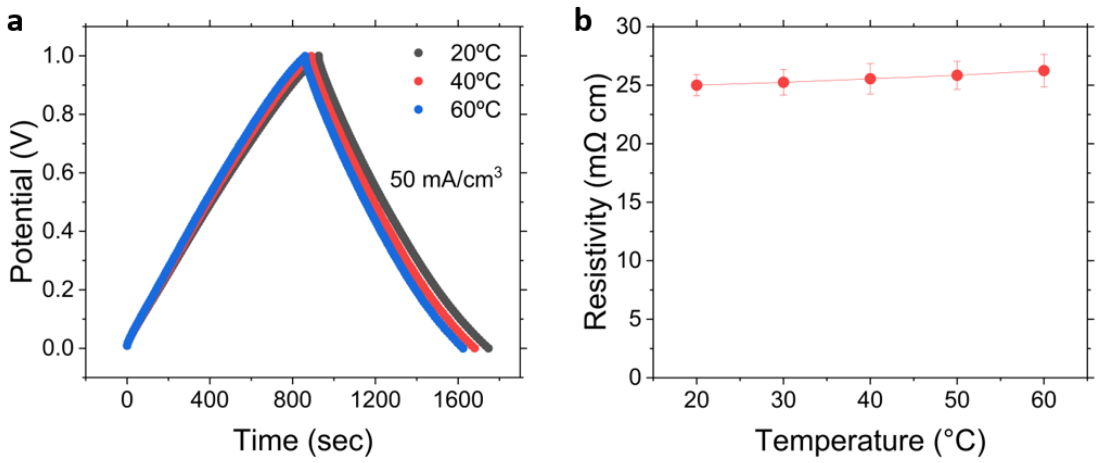

FIG. 20. Thermal stability of synthetic fiber composites. (a) Galvanostatic charge/discharge profile under varied thermal conditions from 20ºC to 60°C, CNT-25%. **(b)** CNT composites conductivity under varied thermal conditions, CNT-25%.

To study the thermal stability of the proposed CNT-based composite in the aqueous LiCl system, we tested the same sandwiched SC (CNT-25%) under various thermal conditions from 20C to 60C. The galvanostatic charge/discharge profiles at 50 mA cm^{-3} rate from 0 to 1 V under varied thermal conditions (20ºC to 60ºC) are shown in **Fig. 20a**. The electrochemical performance results indicated that this SC architecture is barely affected by the temperature change from 20ºC to 60°C on a non-thermoresponsive substrate. The corresponding EIS measurements of SC in terms of temperature also confirm the minimal variation of the electrochemical temperature coefficient in this temperature range (Gao et al., 2017). To study the influence of the thermal conditions on the electrode conductivity, the resistivity from acid-treated rGO/CNT ink (CNT-25%, 15 mm by 2.5 mm electrodes, 6 µm thick) was measured under varied thermal conditions, and the results were plotted in **Fig. 20b**. The conductivity was found to slightly decreases (<5%)

when the temperature increases from 20ºC to 60°C, which is consistent with the related study about the conductivity of carbon-based low-dimensional materials (Ebbesen et al., 1996). The slight variations of the rGO/CNT electrode conductivity indicate the minor influence caused by the temperature range from 20ºC to 60°C on the electrode performance in a non-thermoresponsive architecture.

5. Test Case I: Carbon Nanotube-Based Thermoresponsive Supercapacitor

This chapter presents a novel design and fabrication strategy for thermoresponsive supercapacitors against thermal runaway issues using the CNT-based composite ink developed in Chapter 4 (**Research Task 5**). We first introduce a thermoresponsive supercapacitor mechanism and propose a fully-packaged supercapacitor design. The proposed design is fabricated using the DIW process with a temperature control approach, and the fabricated supercapacitor is tested under various thermal conditions. Some contents have been previously published in (permissions are included in the appendix):

Jiang, Y., Cheng, M., Shahbazian-Yassar, R., & Pan, Y. (2019). Direct Ink Writing of Wearable Thermoresponsive Supercapacitors with rGO/CNT Composite Electrodes. Advanced Materials Technologies, 4(12), 1900691.

5.1 Thermal Runaway Issues of Electrochemical Devices

Carbon-based supercapacitors (SCs) are of significant interest in wearable electronics, sensing, energy harvesting, and medical applications (An et al., 2001). They are considered as next-generation energy storage devices with unique electrical and mechanical properties. The intrinsic characteristics of porous carbon, including high specific surface area, uniform pore size distribution, and excellent conductivity, play an essential role in electrochemical performance. Furthermore, extensive efforts have been made recently on the design and manufacturing of flexible SCs, which can maintain their electrochemical performance under deforming (bending, stretching, or twisting). Despite these advances, they lack the self-protection against harsh conditions to realize the potential for intelligent energy storage devices. For SCs, one of the most

common safety issues is the thermal runaway, which is caused by the considerable heat generated during rapid charging and discharging (Feng et al., 2018).

When SCs are used in harsh conditions, like extreme weather or electronic components that generate significant heat locally, the thermal runaway issue is even more frequent or severe. Thermal runaway damages to the product, such as explosion and fire, have been widely reported and remain a significant challenge in SCs applications. Some electrode/electrolyte materials may also produce harmful compound by-products and bring new environmental issues. For example, under an overheated condition caused by the thermal runaway, the lithium-ion battery electrolyte's reaction with the material of the unprotected positive electrode results in the formation of toxic fluoro-organic compounds (Hofmann et al., 2017). Conventional solutions to address the thermal runaway issues in SCs are using alternative electrode or electrolyte materials or adding heat sinks. However, alternative materials, including solid-state or polymer gel electrolytes, show low ionic conductivity (Hammami et al., 2003). This method provides an immutable slow charging/discharging rate under various thermal conditions. The addition of the heat sink makes the device bulky and impossible for some applications that require flexibility and compactness. Besides, almost all these approaches compromised the energy performance of SCs, which is degraded by the static charge-discharge rate under the various thermal circumstance.

5.2 Proposed Thermoresponsive Supercapacitor Mechanism

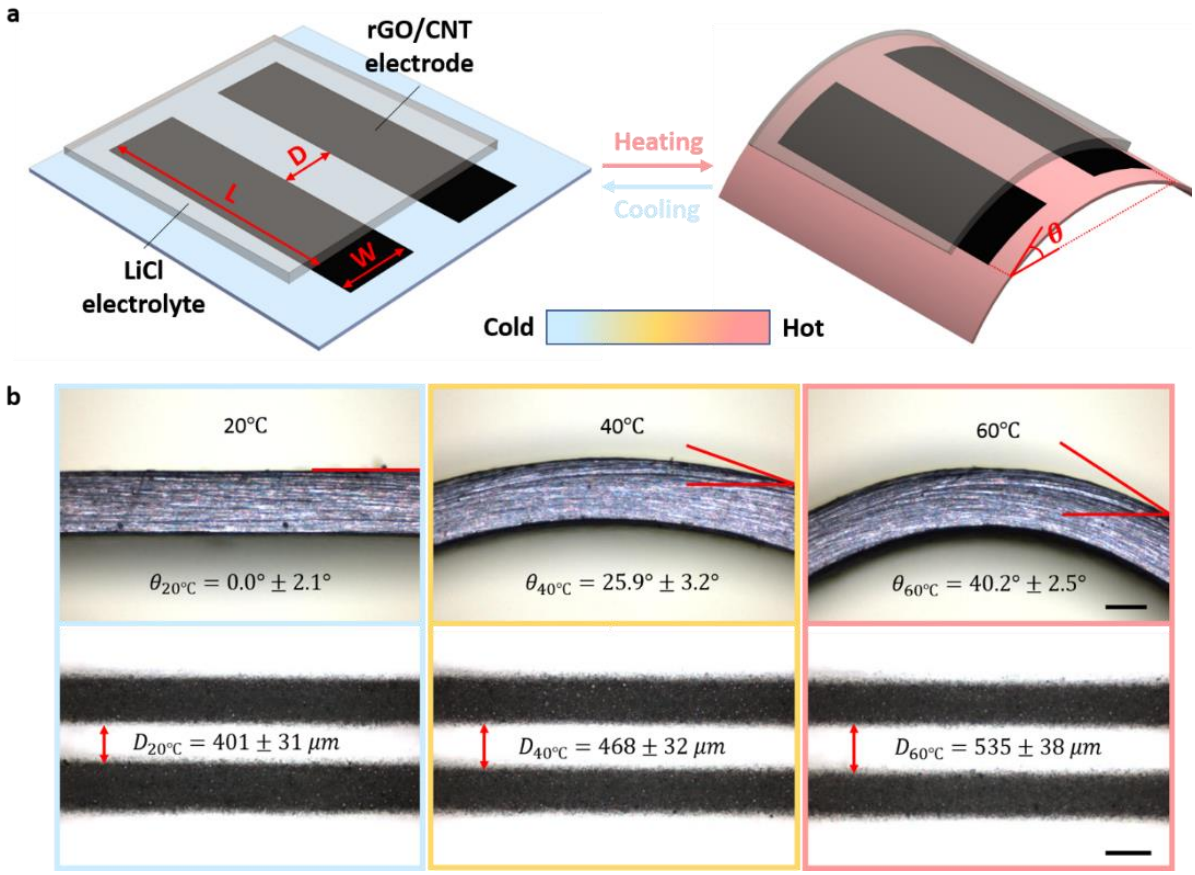

FIG. 21. Thermoresponsive mechanism of supercapacitor structure. (a) Schematic drawing of typical in-plane SC under temperature change. **(b)** Measured thermoresponsive geometry dynamics of the as-fabricated single SC cell (side view scale bar = 0.2 mm, top view scale bar = 0.5 mm).

To overcome these shortcomings, we report a novel temperature-dependent SCs structure that works as self-protection against the thermal runaway issues with a powerful and efficient thermoresponsive mechanism, by self-adjusting the charge-discharge rate according to environmental temperature. To realize the temperature-dependent structure, we propose to integrate shape-memory materials in SCs design. Shape memory alloys (SMAs) can endure

reversible phase transitions stimulated by temperature or humidity. Such mechanical property they exhibited is namely pseudoelasticity. Numerous applications of SMAs include valves in piping systems, packaging devices, and biomedical materials (Hartl et al., 2007). Although many studies of shape memory polymers (SMPs) have been reported, most of them are limited to one-way shape memory behavior, and the cycling time is usually minimal (Ge et al., 2014). Compared with SMPs, SMAs show higher stability and minor long-term fatigue, enabling a more reliable SC construction. Hence, in this study, SMA is investigated to allow for the thermoresponsive and self-protection functionality of SCs.

The thermoresponsive mechanism of the typical in-plane SC design is characterized by the SMA bending angle θ and the cell geometries (electrode length L, width W, and the distance D between two electrodes in millimeter, **Figure 21a**). In general, θ is a function of temperature T, ranging from 20°C to 60°C in wearable applications:

$$\theta = f(T) \tag{5.1}$$

To further estimate the capacitance of thermoresponsive SCs, we assume the active materials are uniformly distributed with a planar density α (mg mm^{-2}), and the pore surface is entirely fulfilled by the electrolyte. The capacitance C (mF) of the typical in-plane SC design given a bending angle θ is approximated by:

$$C = \frac{\varepsilon\alpha\beta WL\,\mathrm{sinc}\,\theta}{D+W} \tag{5.2}$$

where ε is the permittivity, and β (m^2 mg^{-1}) is the surface area of the active materials. Substituting Equation 5.1 to Equation 5.2, we obtain:

$$C = \frac{\varepsilon\alpha\beta WL\sin[f(T)]}{(D+W)f(T)} \tag{5.3}$$

When the surrounding temperature of an SMA increases from T_1 to T_2, the corresponding bending angle varies from θ_1 *to* θ_2. The capacitance difference ΔC caused by the thermal change is:

$$\Delta C = \frac{\varepsilon\alpha\beta WL}{(D+W)}\left[\frac{\sin\theta_1}{\theta_1} - \frac{\sin\theta_2}{\theta_2}\right] = \frac{\varepsilon\alpha\beta WL}{(D+W)}\left\{\frac{\sin\,[\mathrm{f}(T_1)]}{\sin\,(T_1)} - \frac{\sin\,[\mathrm{f}(T_2)]}{\sin\,(T_2)}\right\} \tag{5.4}$$

According to the current-voltage relation of typical capacitors, the current density reduction percentage p_1 is:

$$p_1 = \frac{\Delta C}{C} = 1 - \frac{\theta_1 sin\theta_2}{\theta_2 sin\theta_1} = 1 - \frac{f(T_1)\sin\,[f(T_2)]}{f(T_2)\sin\,[f(T_1)]} \tag{5.5}$$

Based on the Joule heating equation, the deformation-caused heat reduction percentage p_2 in a current path for preventing thermal runaway is:

$$p_2 = p_1^2 \tag{5.6}$$

In this study, the bending angles of a 12.0 mm by 6.0 mm SMA plate patterned with a typical in-plane SC cell (W = 0.5 mm, L = 5.0 mm, D = 0.4 mm at 20°C) are measured under various temperatures (**Fig. 21b**). As calculated, if the SC endures a thermal change from 20°C to 60°C, possibly due to improper long-term use or harsh environments, the heat produced by excessive current or other overheated components is alleviated approximately 35% by the proposed design.

This novel thermoresponsive SCs structure addresses the thermal runaway and functionalizes smart thermal sensing in wearable electronics applications (Stoppa and Chiolerio, 2014). For instance, due to the extension to the capabilities of medical monitoring, such thermoresponsive energy storage devices can be integrated into the routine care of patients with chronic diseases, providing an accurate tracking and a reliable drug delivery process for the healthcare management (DicCbshfsE et al., 2011).

5.3 Thermoresponsive Supercapacitor Design and Fabrication

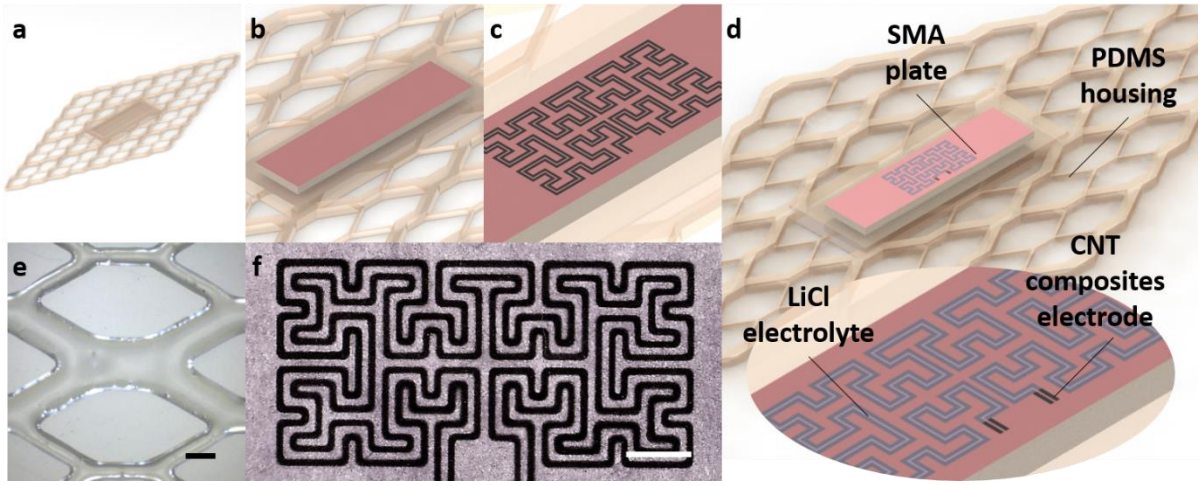

FIG. 22. Thermoresponsive supercapacitor design and fabrication. (a) Schematic drawing of elastomer housing. **(b)** Schematic drawing of SMA plate. **(c)** Schematic drawing of CNT-based electrodes. **(d)** Schematic drawing of the integrated SC design. **(e)** Printed elastomer housing (scale bar = 1 mm). **(f)** Printed CNT-based electrodes (scale bar = 2 mm).

Based on the proposed thermoresponsive structure, we investigate the DIW of wearable thermoresponsive supercapacitor with high geometrical complexity using the prepared CNT-based composites (Chapter 4) ink. Additionally, to preserve SCs temperature-dependent shape-changing property and improve SCs reliability, our proposed DIW process prints elastomer layers to seal the whole SCs structure fully, and hence fabricate entirely packaged thermoresponsive SCs in one-platform and one-job without any assembly or post-processing steps (Jiang et al., 2019).

To fabricate an SC, flexible housing (PDMS) for the thermoresponsive SMA plate is first printed at an elevated temperature. The design of the highly flexible, lightweight, nonbiodegradable housing is inspired by a leaf-like architecture (**Fig. 22a** and **Fig. 22e**). The flexibility not only accommodates the SMA bending and flattening but also provides a robust

protection to the human body for wearable applications. The SMA plate, which is entirely covered with a stretchable film mask, is placed in the housing (**Fig. 22b**). The CNT-based ink is then deposited repeatedly in a layer-by-layer fashion onto the film substrate, using a DIW technique. To demonstrate the capability of manufacturing complicated geometries, a Hilbert-pattern in-plane supercapacitor design is investigated (**Fig. 22c** and **Fig 22f**). The pattern is inspired by conventional supercapacitor interdigital structures, which are suitable for both sensing and wearable energy storage device applications (Pech et al., 2010). After evaporating water contents in the printed CNT-25% composites, acids are printed on the dried CNT composites layers to remove the impurities and surfactants remained in it (Chen et al., 2017). The acids are deposited in a dot-by-dot way, instead of a continuous filament, to avoid the common bulge problem due to its low viscosity with 1.2 mPa s at room temperature (Duineveld, 2003). Afterward, acetone and deionized water are used to neutralize the printed electrodes. The electrodes are further connected by writing aqueous LiCl electrolyte onto the pattern (**Fig. 22d**). The fabrication is completed upon the printing of an elastomer layer on the top of the electrolyte to adequately package the SCs to improve the reliability in the long term.

5.4 Supplementary Fabrication Experimental Details

In addition to the CNT-based composites (refer to Chapter 4), other chemical information and experimental details are included in this section. The electrolyte was prepared by adding lithium chloride powder (12.0 g, >99.0%, Sigma-Aldrich) to deionized water (40 ml), followed by stirring (Eurostar 60, IKA) for 5 min at a 500 rpm rotating speed before storing at room temperature. Dow Sylgard 184 silicone elastomer was purchased and used as received for the housing. It is a two-component (mix ratio 10:1), room temperature curing encapsulant that is used as a protective coating for electronics. In this study, two components were first mixed at 2000 rpm for 5 min before loading to a 10cc syringe barrel. After fully sealing the printed in-plane SC, it is solidified at 25℃ for 48 hours. The shape memory alloy plates (140 mm by 6 mm by 0.3 mm) were purchased from Baoji Seabird Metal Material Co (China). It is then carefully cut and polished into 12.0 mm by 6.0 mm by 0.3 mm pieces. The as-cut plate is flat at 15°C. It starts to curve when the temperature increases and reaches the maximum curvature until stabilizing at 65°C. It recovers to the flattened shape when the environment temperature decreases to 15℃. A stretchable film (Scotch 8884) was then attached to the SMA plate.

5.5 Temperature Controlled Solidification Process

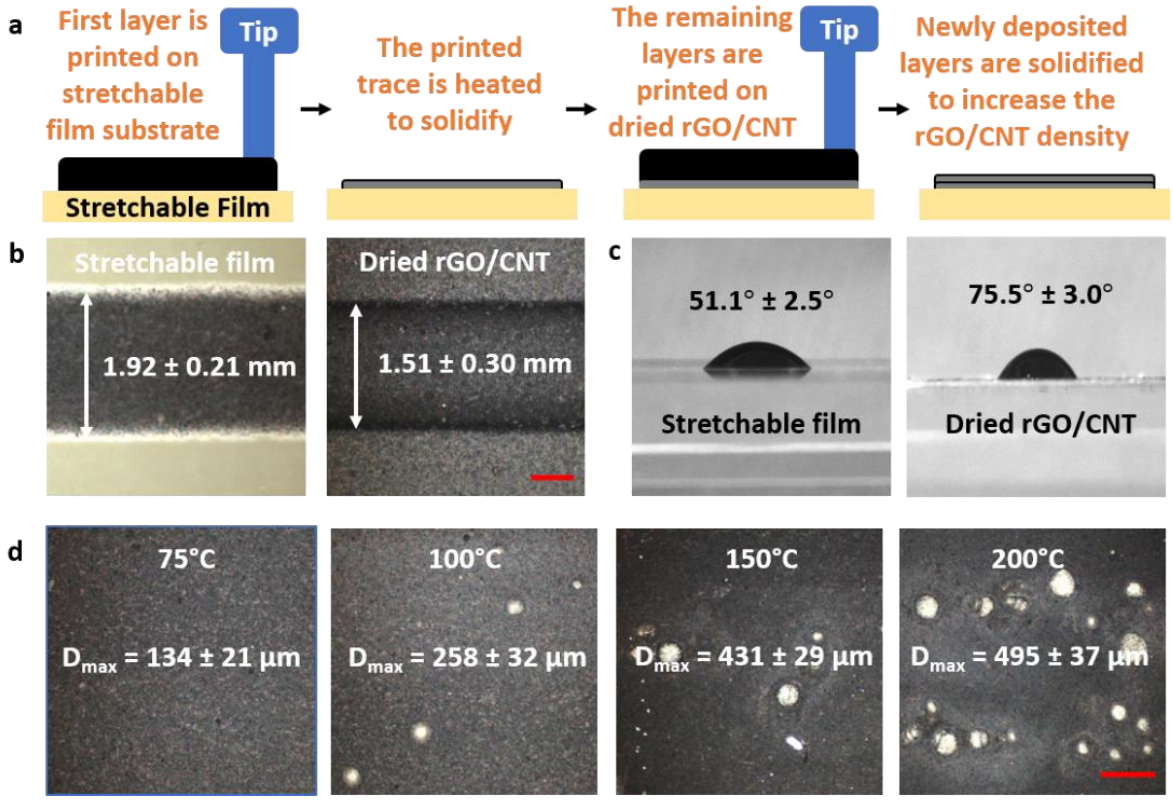

FIG. 23. Solidification strategies for fiber composites (I). (a) Step-by-step illustration of the layer-by-layer printing process of CNT-based composites on a heated substrate. **(b)** Filament width comparison between samples printed onto stretchable film and dried CNT-10% substrates under the same setting (scale bar = 0.5 mm). **(c)** Equilibrium contact angle measurements of CNT-10% on stretchable film and dried CNT-10% substrates. **(d)** Observation of undesired pores on dried single-layer CNT-10% sample surface at different heating conditions (scale bar = 1 mm).

In this section, we developed temperature-controlled printing mechanisms for improving printing accuracy and efficiency. For synthetic fiber-based inks, the temperature-controlled printing process enables the rapid fabrication of high-purity carbon-based materials. For example,

the CNT-based composites inks (refer to Chapter 4) are deposited repeatedly onto a heated substrate in a layer-by-layer way (25 layers in total). After the deposition of a new layer, it is thoroughly dried by the heated substrate, as demonstrated in **Fig. 23a**. It should be noted that the first layer is printed onto a stretchable film (Scotch 8884) substrate, while the remaining layers are printed onto the previously dried composite layers.

To investigate the influence of both substrates on the printed filament geometry, CNT-10% is extruded through a 0.96 mm inner diameter dispensing tip onto the stretchable film substrate and the dried CNT-10% substrate, separately. As shown in **Fig. 23b**, the solidified filament width decreases from 1.92 mm to 1.51 mm. Such geometry change is mainly caused by the wettability of both substrates, which is also confirmed by the equilibrium contact angle measurement shown in **Fig. 23c**. Stretchable film (51.1°) shows a higher wettability than the dried CNT-10% (75.5°) substrate. Hence, to compensate for the effects of two different substrates for a consistent filament width, the printing velocities are adjusted based on the measurements.

In addition to tuning the printing velocity for printing on varied substrates, the heating temperature for CNT composites inks is also adjusted. To characterize the appropriate temperature, a single-layer 10 mm by 10 mm structure is printed onto a glass substrate and heated at 75°C, 100°C, 150°C, and 200°C until thoroughly dried, respectively. Although higher temperatures can rapidly solidify the printed ink, it leaves considerate pores onto the dried surface. In this study, D_{max} is defined as the maximum observed pore diameter under a microscope. **Fig. 24d** shows the optical images of samples heated at different temperatures. Samples heated at 75°C shows little pores (*Dmax* at 75°C = 134 μm). The observed maximum pore diameter is increased by increasing heating temperature (*Dmax* at 100°C = 258 μm, *Dmax* at 150°C = 431 μm, *Dmax* at 200°C = 495 μm).

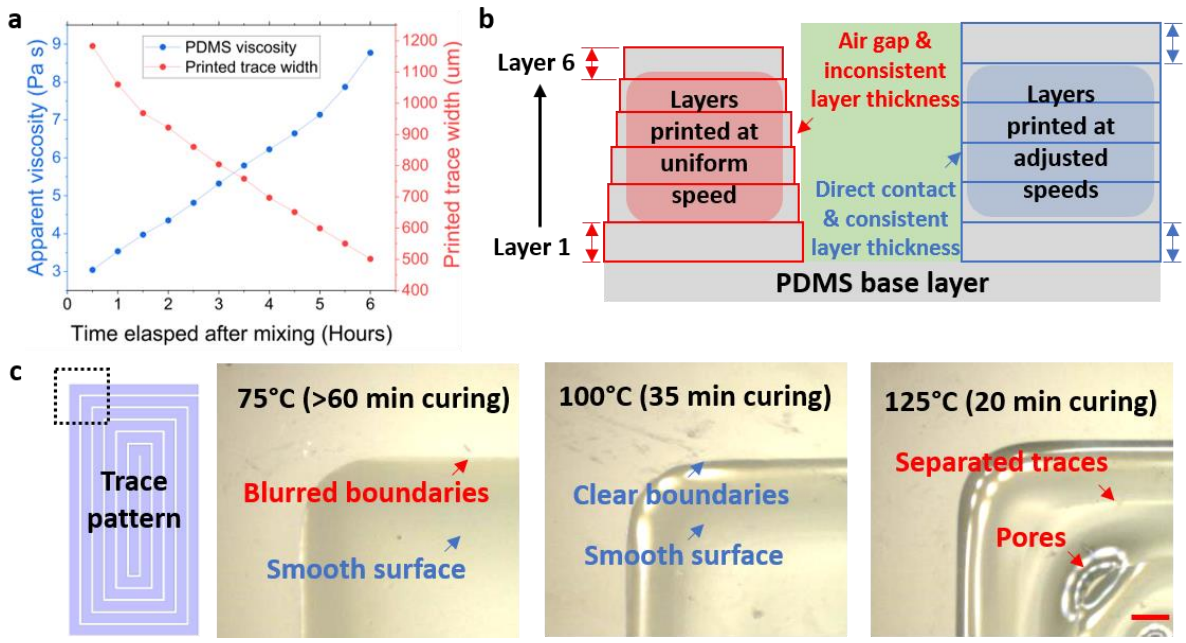

FIG. 24. Solidification strategies for fiber composites (II). (a) Apparent viscosity and printed filament width influenced by the time elapsed after elastomer base and curing agent mixing. **(b)** Demonstration of the non-adjusting speed and adjusting speed methods for layer-by-layer elastomer printing. **(c)** Elastomer curing temperature investigation for optimizing printed surface quality of a single layer, 20 mm by 10 mm by 20 mm rectangular samples (scale bar = 0.5 mm).

Silicone-based elastomers, such as polydimethylsiloxane (PDMS), have superior elasticity, biocompatibility, and optical transparency (Mata et al., 2005). It is a two-part (base and curing agent, 10:1 mixing ratio), clear, room temperature and heat cured elastomer with an approximately 90 min pot life. After this 90-minute pot life, the material viscosity would be significantly changed due to the crosslinking. The curing time for the elastomer at 100°C is 35 minutes according to the specification. A broad range of applications has been demonstrated in bioengineering, flexible and wearable electronics (Liu et al., 2016). It is also commonly used in fiber-based composites as the matrix material. **Fig. 24a** shows the viscosity change of the elastomer within the first 6 hours after

mixing base and curing agent. The measured apparent viscosity at a consistent 0.1 s^{-1} shear rate increases from 3.0 Pa s to 8.9 Pa s. The elastomer is extruded using a 0.46 mm inner diameter blunt dispensing tip (5.0 psi air pressure) at a 10 mm s^{-1} printing velocity into 20 mm filaments to investigate the influence of the gradually increased viscosity to the printed geometry (filament width). The measured filament width decreases from 1180 μm to 501 μm within the first 6 hours after mixing. As a result, with the conventional uniform printing speed, the printed multi-layer structure will have significant shrinkages along the printed filament width direction, resulting in printing defects such as air gaps between filaments within the layer geometry inaccuracy.

To address the shrinkage problem during PDMS printing, a possible solution is to adjust the printing velocity over time, as illustrated in **Fig. 24b**. Also, because the chemical properties of the PDMS ink are changing during the printing process, the curing temperature should be adjusted appropriately. Samples with a 20 mm by 10 mm rectangular shape are printed and heated at 75°C, 100°C, and 125°C substrate, respectively (**Fig. 24c**), to identify the appropriate curing temperature at different printing time. Although samples solidified at 75°C show a smooth surface, the boundaries are blurred. The curing time (> 60 min) is over-long for the multi-layer DIW process, considering the relatively short pot life of the elastomer ink. Samples solidified at 125°C show separated filaments due to the over-fast curing, which leaves little time for filaments to merge to form an integral and smooth surface properly. Several undesired pores are also observed at the printed filament corner, while samples printed at 100°C show clear boundaries and smooth surfaces. As estimated, our proposed temperature-controlled mechanism improves the time efficiency by approximately an order of magnitude.

5.6 Thermoresponsive Electrochemical Performance Evaluation

To evaluate the performance of the fabricated thermoresponsive SC, an external heating source is employed to mimic the thermal runaway situation to demonstrate the effective thermoresponsive self-protection mechanism. The electrodes were fabricated by extruding CNT-25% ink in a Hilbert pattern where aqueous LiCl serves as the electrolyte. The entire SC was sealed and protected by the printed elastomer. All the printed cells were tested using a Bio-Logic VMP3 Potentiostat electrochemical workstation. The environmental temperature was controlled by a temperature test chamber (Binder FP53, Germany). The Galvanostatic charge/discharge of the cells was tested at a scanning rate ranging from 20 mA s^{-1} to 200 mA s^{-1}. The electrochemical impedance spectroscopy test results were collected in a frequency range of 0.1 Hz to 1 MHz. The temperature-dependent CV curves at 50 mV s-1 scan rate of shape memory alloy integrated SCs are shown in **Fig. 25a**. Upon increasing the temperature from 20 to 60°C, the charge-discharge currents decrease to avoid burst heat generation. Similar trends are also observed from the galvanostatic test at 20 mA/cm^3 (**Fig. 25b**). This indicates the printed SC functionalize appropriately in a wide temperature range due to the integrated SMA substrates. The specific capacitances at various current densities are summarized in **Fig. 25c**. The specific capacitance of printed SCs at different current densities decreases by increasing the ambient temperature. Such reduction suggests that the temperature-dependent electrode geometry enables dynamic responses in the specific capacitance of SCs. The estimated heat reduction percentage is approximately 40%. When thermal runaway happens by increased ambient temperature, it weakens the power delivery dynamically by inhibiting the transportation of conductive ions to prevent potential damages.

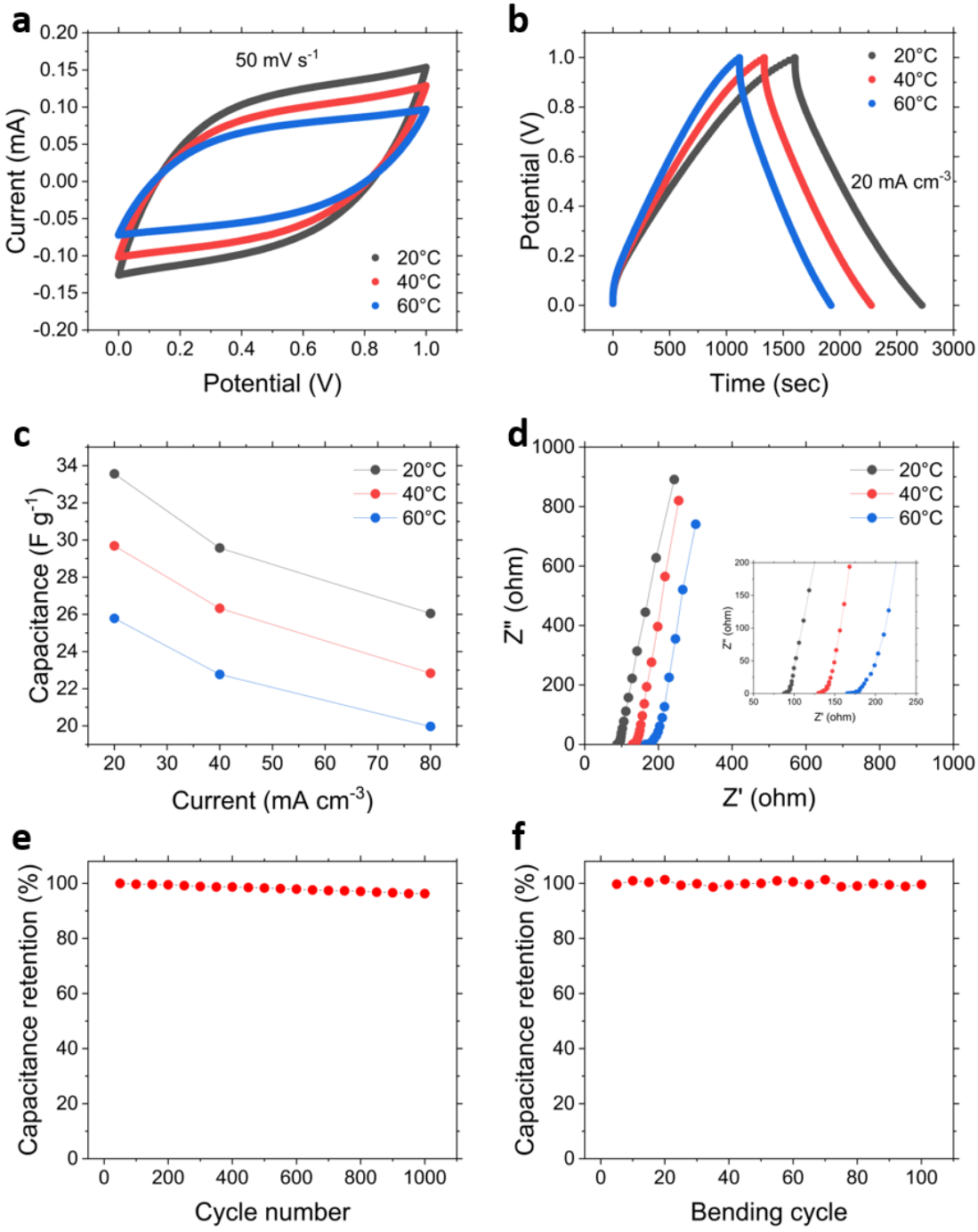

FIG. 25. Thermoresponsive supercapacitor from 20°C to 60°C. (a) CV profiles. **(b)** Galvanostatic charge/discharge profiles. **(c)** Specific capacitance at various current densities. **(d)** Nyquist plot from EIS. **(e)** Capacitance retention of 1000 cycles under a current density of 80 mA/cm^3 at 20°C. **(f)** Capacitance retention at different bending cycles.

To further investigate the inhibition of ion transportation by the functional thermal responsive design, the impedance of SCs is measured through the electrochemical impedance spectroscopy (EIS) approach (**Fig. 25d**). In general, the impedance of an SC is mainly determined by two distinct processes: the charge transfer during a fast voltage change at the electrode-electrolyte interface (high frequency), as well as the ion diffusion during a slow voltage change within the electrolyte (low frequency). In this study, the temperature-dependent SC structure design enables a dynamic impedance at low frequency. For typical in-plane SC designs, the electrolyte resistance is affected by the resistivity of the electrolyte and cell constant. A larger electrode gap leads to a higher electrolyte resistance, degrading capacitive performance. The equivalent series resistance (ESR) of the printed SC increases from 85 to 160 Ω when the temperature is rising from 20°C to 60°C, mainly caused by the increased electrode resistance. The increased ESR results in a drop of voltage during the charge/discharge process, which reduces the usable capacity of the SC. These results verified that the impedance of the SC is highly temperature-dependent, providing self-protection against the thermal runaway. Compared with conventional passive approaches to solving thermal runaway in energy storage devices, our proposed strategy employs a reversible active self-protection mechanism. Besides, the printed SC is found to be robust under temperature changes, demonstrating a 95.6% retention after 1000 cycles at a current density of 80 mA/cm^3 (**Fig. 25e**) and retains its original capacitance after 100 bending cycles (**Fig. 25f**).

6. Natural Fiber Composites Inks

This chapter investigates the development of printable natural fiber composite inks using raw flax fiber (**Research Task 6**). We examine the influence of a probe sonication process on the flax fiber structure modification and the ink printability (**Hypothesis III**). The preparation process, rheological property, and extrusion capability of the proposed natural fiber composite inks are studied. Some contents have been previously published in (permissions are included in the appendix):

Jiang, Y., Plog, J., Yarin, A. L., & Pan, Y. (2020). Direct ink writing of surface-modified flax elastomer composites. Composites Part B: Engineering, 108061.

6.1 Natural Fiber Structure Introduction

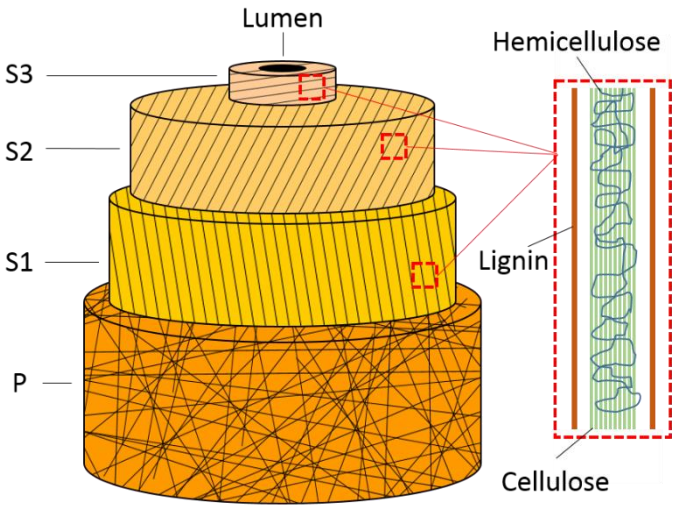

FIG. 26. Typical natural fiber structure.

In general, a single fiber of plant-based natural fibers consists of several cells. These cells are formed by cellulose-based crystalline microfibrils, connecting to a complete layer by lignin and

hemicellulose. Multiple cellulose-lignin-hemicellulose layers in the cell walls combine to create a multiple layer construction (**Fig. 26**). For instance, flax fibers have irregular polygonal cross-sections and a hollow structure, consisting of approximately 81% cellulose, 14% hemicellulose, 3% lignin, and 4% pectin (Huang and Netravali, 2007). The main structure of flax fibers consists of two walls. The first wall along the plant growth is a primary wall containing both cellulose and hemicellulose, with microfibrils disorderly arranged. The thickness of the primary wall is approximately 0.2 μm, according to the recent studies (Amiri et al., 2015). The secondary wall, which consists of another three layers (first, second, and third), is located inside the primary wall. The thickness of the second layer is usually more extensive than those of the first and third layers. It also contributes to the overall strength of the fiber. In this three-layer structure of the secondary wall, helically wound chain-structured microfibrils have been observed. The microfibrils are formed by 30 to 100 cellulose molecule chains, oriented with an approximately 10° angle along the fiber's center axis. The secondary wall contributes up to 70% to the fiber Young's modulus. Hence, a higher cellulose content can result in a higher tensile modulus.

6.2 Sonication Approach for Natural Fiber Modification

Due to the microfibrils' disordered morphology in the primary wall, printing natural fiber composites shows tremendous difficulties in DIW. The fiber agglomeration causes the typical tip clogging issue in extrusion-based AM. Such agglomeration is usually due to the composite's oversized fiber bundles, which can form large fiber blocks near the joint between the dispensing tip and the syringe barrel (**Fig. 26a**), leaving insufficient room for fiber movement resulting in a printed filament with minimal fiber loading, as shown in **Fig. 26b**.

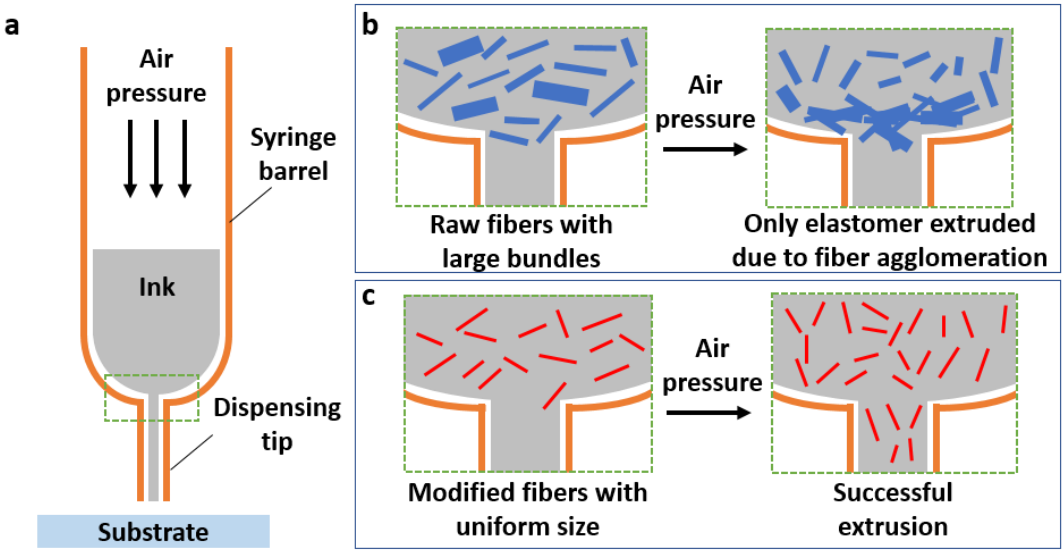

FIG. 27. Demonstration of tip clogging issue of natural fiber composites. (a) Typical clogging location. **(b)** Agglomeration of raw natural fibers. **(c)** Easy extrusion of surface-modified natural fibers.

To make natural fibers printable, we modified them using a sonication-based approach, which removed the primary wall, leading to more uniform fibers without large bundles. The proposed sonication-based surface modification process for flax can separate those large fiber

bundles to enhance the natural fiber-based composite extrusion process (**Fig. 26c**). This method also preserved the secondary wall's aligned microfibrils, keeping the majority of the raw fiber's strength.

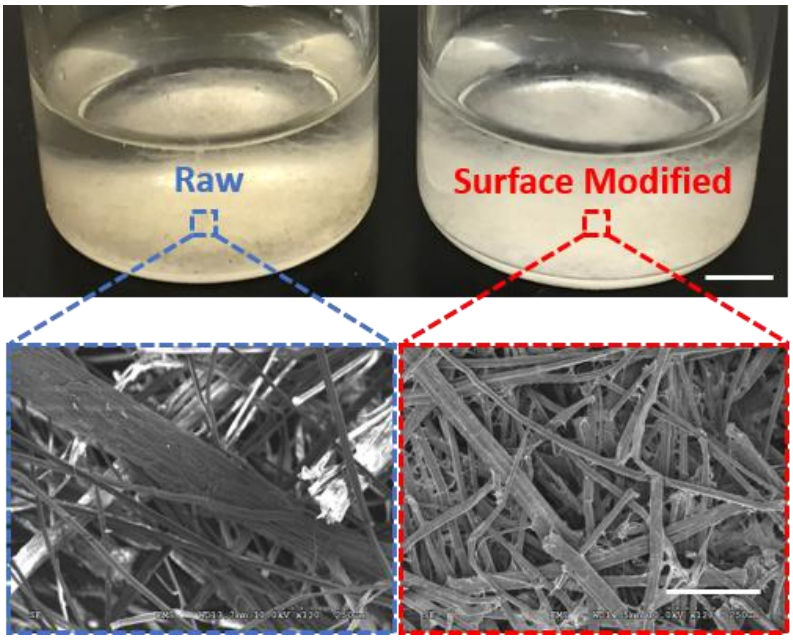

FIG. 28. Natural fiber surface modification

To investigate the sonication process on the natural fiber structure, we soaked the raw short flax fiber into deionized water and used a 300-Watt probe sonication to process the mixture. During the sonication, we observed that the color of short flax fibers changed from brownish to white during the sonication process. Some dark brown particles (primary wall residues) were floating on top of the suspension during the sonication process. **Fig. 28** shows the scanning electron microscopic images of the raw and surface-modified flax fibers. As confirmed, the sonication process mainly removed the primary wall of the raw flax fibers by moderate vibrations. Between each sonication period, those primary layer residues were filtered. The remaining surface-modified flax fibers (sonicated) became more consistent in dimensions upon the removal of these primary wall residues,

which efficiently minimized the fiber agglomeration and made it possible to extrude fiber-dispersed inks without adding additional chemicals. The surface modification process also separated most large bundles of raw flax fibers, which further reduced the average fiber diameter to improve the flexibility. After removing the primary wall of the raw flax fibers, the remaining surface-modified flax in deionized water suspension was dried at 90 °C in an oven overnight. The thoroughly dried surface-modified flax fibers were collected.

6.3 Preparation of Natural Fiber Composite Inks

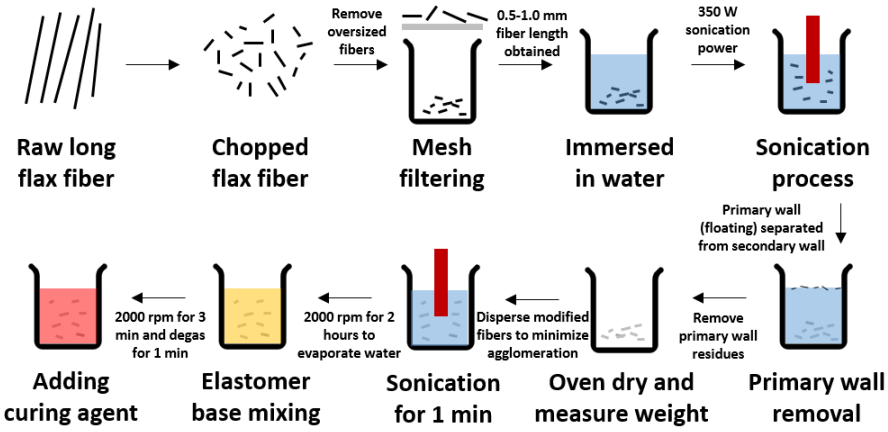

FIG. 29. Natural fiber composites preparation process.

Based on the sonication approach for natural fiber modification, the complete composites preparation process is shown in **Fig. 29**. Raw flax fibers with 20 to 150 μm diameter were first carefully chopped into short pieces. The length of the as-cut fibers mainly ranged from 0.5 mm to 2.0 mm. Afterward, 200 mg of short flax fibers were filtered by a copper mesh with 0.5 mm pores to remove oversized flax fibers further. The filtered flax fibers, together with 50 ml deionized water, were homogenized by a probe sonicator at a 350-Watt power setting. The total sonication time was 3 h (30 min per sonication period, 6 periods in total). The mixture was cooled down to room temperature between each sonication period to avoid the overheating issue in the probe sonication process. In this study, to prepare the composite, Dow Sylgard 184 silicone elastomer was purchased and used as received. It is a two-component (base and curing agent, mix weight ratio 10:1), room temperature curing encapsulant. The 0.2 wt% and 0.5 wt% composites were prepared by adding 20 mg and 50 mg of surface-modified flax fibers to 9.1 g elastomer base, separately. Both blends were mixed at 2000 rpm (AR-100, Thinky) for 30 min. Then, the blends were degassed for 2 min. Afterward, they were blended with 0.9 g curing agent at 2000 rpm for 3 min.

6.4 Extrusion of Natural Fiber Composite Inks

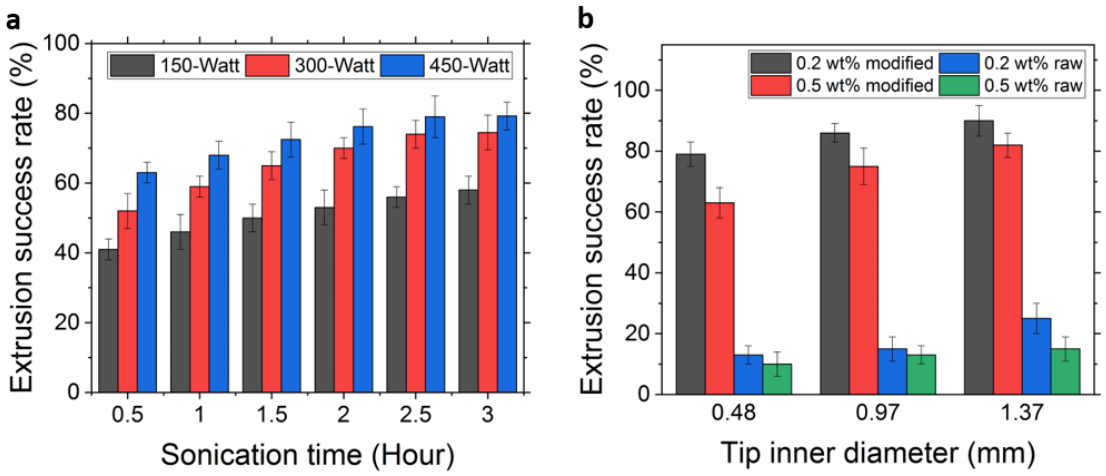

FIG. 30. Extrusion-capability of surface-modified flax elastomer composites. (a) Extrusion success rate of 0.5 wt% surface-modified flax elastomer from different sonication settings, 95% CI. **(b)** Extrusion success rate of 0.2 wt% and 0.5 wt% raw and surface-modified flax elastomer composites through various sized dispensing tips, 95% CI.

The proposed sonication-based surface modification process for flax can separate those large fiber bundles to enhance the natural fiber-based composite extrusion process. To systematically study the sonication process parameters, the extrusion-capability of as-prepared 0.2 wt% and 0.5 wt% flax elastomer composites are experimentally characterized through various sized dispensing tips under different sonication process settings. The blunt dispensing tips' inner diameters are 0.48 mm, 0.97 mm, and 1.37 mm, separately. To characterize the printability, the as-prepared composites are consistently extruded using 3.0 psi pressure for 120 sec to determine the printability. In the repeat experiments, if the tip clogging issue happens, we consider it as a failure.

As shown in **Fig. 30a**, we first investigated the sonication process setting's influence on the extrusion success rate. The inks in this test were loaded by 0.5 wt% fibers in PDMS. The test was

conducted using 0.97 mm dispensing tips. The sonication power settings were 150-Watt, 300-Watt, and 450-Watt, separately. This test indicates that the sonication time is generally proportional to the extrusion success rate, while sonication time longer than 2 hours shows insignificant improvement for 300-Watt and 450-Watt settings with an approximately larger than 70% extrusion success rate. The sonication power is also proportional to the extrusion success rate. 150-Watt power setting shows the least improvement in printability, while 300-Watt and 450-Watt have a much higher extrusion success rate in the overall trend.

We also studied the influence of dispensing tip on the printability. **Fig. 30b** demonstrates the extrusion success rate of 0.2 wt% and 0.5 wt% raw and modified fiber elastomer composites after 3 hours sonication process at a 300-Watt power setting. As expected, surface-modified fibers show a much higher extrusion success rate. For 0.97 mm and 1.37 mm dispensing tips, the extrusion success rates of surface-modified 0.2 wt% and 0.5 wt% fiber elastomer composites are similar, range from 69% to 85%, which is almost four times of the raw fiber ones with only 13% to 23% extrusion success rate. For the 0.48 mm dispensing tip, the extrusion success rate of surface-modified 0.2 wt% and 0.5 wt% fiber elastomer composites decreased to 76% and 60%, separately. This can be explained by the fiber length (0.5 mm to 1.0 mm in this study), which is longer than the tip inner diameter, somehow increases the potential of clogging. The 0.5 wt% flax fiber composites have a slightly lower extrusion success rate than 0.2 wt% for all the dispensing tips. This study's findings reveal that the sonication-based surface modification process enables the extrusion of natural fiber embedded elastomer composites.

6.5 Rheological Properties of Natural Fiber Composite Inks

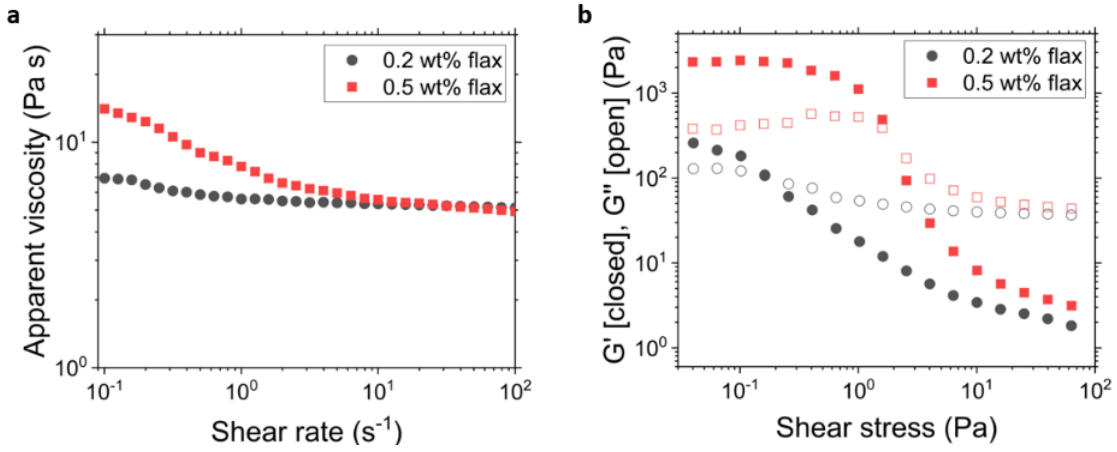

FIG. 31. Natural fiber composites rheological characterization. (a) Apparent viscosity characterization. **(b)** Modulus characterization.

After identifying the proper sonication settings, the rheological properties of the as-prepared 0.2 wt% and 0.5 wt% flax composite inks were measured by a rotational rheometer (Kinexus ultra+, Malvern). As shown in **Fig. 31a**, the 0.5 wt% flax composite ink reveals a slight shear-thinning behavior. It has a higher apparent viscosity up to 14.1 Pa s when the shear rate ranges from 0.1 s^{-1} to 10 s^{-1}. On the other hand, the 0.2 wt% flax composite ink reveals a practically Newtonian-line behavior. The apparent viscosity of the 0.2 wt% flax composite decreases from 6.9 Pa s to 5.1 Pa s when the shear rate increases from 0.1 s^{-1} to 100 s^{-1}. Both inks reveal a similar apparent viscosity trend in the 10 s^{-1} to 100 s^{-1} shear-rate range, which ensures the printability in extrusion-based additive manufacturing technologies. **Fig. 31b** shows the storage modulus (G') and loss modulus (G'') as functions of shear stress for the prepared 0.2 wt% and 0.5 wt% flax composite inks. Both inks are elastic-like solids (G' >> G'') with respective G' values of 106.6 and 487.2 Pa that flow when their respective shear yield stress values of 0.16 and 1.59 Pa are exceeded. Once these inks exit the nozzle and return to the zero-shear conditions, they rapidly retain their filamentary shape.

6.6 Printability of Natural Fiber Composite Inks

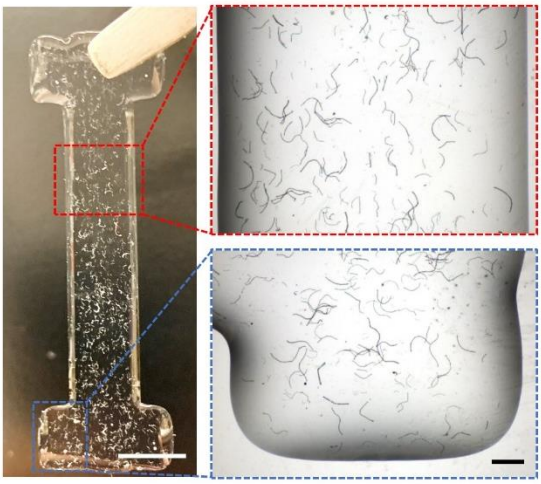

FIG. 32. Images of printed natural fiber composites specimen, left scale bar = 10 mm, right scale bar = 2 mm.

To evaluate the printability of the proposed natural fiber reinforced composited using the sonication approach, a single-layer sample with "I" shape geometry was designed and fabricated, as shown in **Fig. 32**. To write those samples, a 1.37 mm inner diameter stainless steel tip was used to extrude inks onto a glass substrate. The standoff distance was 0.5 mm. The printing speed was 18 mm/s, and the input air pressure was 1.0 psi. The printing temperature was evaluated up to 100 °C to rapidly solidify the samples. It was found that the surface-modified flax fibers are uniformly distributed in the PDMS matrix without agglomerations.

7. Test Case II: Printed Natural Fiber Reinforced Elastomer Composites

As a test case, this chapter demonstrates the DIW of natural fiber-elastomer composite inks developed in Chapter 6 (**Research Task 7**). We first characterize their mechanical performance and then compare them with synthetic fiber-reinforced counterparts. Afterward, we utilize a two-step chemical treatment to obtain transparent natural fibers for optical applications. Some contents have been previously published in (permissions are included in the appendix):

Jiang, Y., Plog, J., Yarin, A. L., & Pan, Y. (2020). Direct ink writing of surface-modified flax elastomer composites. Composites Part B: Engineering, 108061.

Jiang, Y., Yarin, A. L., & Pan, Y. (2020). Printable highly transparent natural fiber composites. Materials Letters, 277, 128290.

7.1 Overview of Natural Fiber Reinforced Elastomer Composites

Silicone-based elastomers, such as polydimethylsiloxane (PDMS), have superior elasticity, biocompatibility, and optical transparency (Mata et al., 2005). A broad range of applications has been demonstrated in bioengineering (Liu et al., 2016), flexible and wearable electronics (Morent et al., 2007). Despite the superior intricate properties of elastomers and their wide applications, researchers also started to investigate functional fillers for producing elastomer composites with new material functionalities. Carbon fibers, glass fibers, and metal particles embedded in elastomer composites have been recently reported (Al-Saleh and Sundararaj, 2009). However, those functional fillers are usually made from unsustainable petroleum. They are not biodegradable and can cause serious disposal/recycling problems in the environment.

Recently, the use of natural fibers instead of synthetic fibers in composite materials attracted significant attention of the research community. Extensive studies on natural fibers,

including sisal (Orue et al., 2016), jute (Matsuzaki et al., 2016), and flax (López Manchado et al., 2003) demonstrated the potential for sustainable and inexpensive components for the next-generation composite materials. These natural fibers exhibit high specific mechanical strength, excellent thermal and acoustic insulation, as well as good biodegradability. In contrast to relatively rigid synthetic fibers, natural fibers also offer excellent flexibility and softness, which make them ideal for many applications such as soft robotics and medical engineering (MR et al., 2018).

Specifically, flax (Linum usitatissimum) is one of the commonly used natural fibers as reinforcement in composites (Yan et al., 2012). Flax fibers are inexpensive and abundant in nature. It is one of the very first materials to be woven into textiles, which was found in graves in Egypt, dating back to 5000 BC. In recent years, Canada has been the largest producer and exporter of flax. Canada produced more than one million tons flax and exported approximately 60% to the EU, 30% to the USA, and 4% to Asia due to the increasing worldwide demand in the linen market. Some other leading producers of flax include France, Belgium, and the Netherlands. Climatic conditions in these regions and countries are suitable for growing and planting flax. The growing cycle of flax is usually short, with only 100 days between sowing and harvesting in some European regions.

Tensile properties of flax fibers are critical in fiber-reinforced polymer composites. Charlet et al. tested single flax fiber using a universal tensile testing machine. It was found that the fibrils arrangement highly affects the tensile properties (Charlet et al., 2009). Garkhail et al. fabricated thermoplastic composites consist of flax fiber and polypropylene and investigated the influence of fiber length and fiber content on stiffness and strength (Garkhail et al., 2000). It was revealed that the stiffness of the flax-based composites is comparable to glass-based composites, indicating that

future research towards significant improvements in tensile and impact strength of these types of composites.

However, the preparation of natural fibers like flax for matrix composites requires extensive efforts due to substantial variations in fiber dimensions and orientations. Many approaches have been developed to prepare fibers in a more consistent and repeatable form, for ease in manufacturing and property control. For instance, it was reported that the alkali treatment of jute in Biopol composites could result in a 30% increase in bending strength (Mohanty et al., 2000). It was proved that the storage modulus of short bamboo fiber-reinforced polypropylene composites could be increased by hybridization. However, these material preparation methods involve complex chemical processes, and most of these composites were fabricated by subtractive manufacturing or injection molding, which have limited flexibility in terms of material manipulation and complicated object geometry.

Recent progress in additive manufacturing enables more advanced design and fabrication of fiber-embedded composites (Tian et al., 2016). For example, carbon fiber-reinforced thermoplastic composites with improved mechanical properties have been fabricated by fused deposition modeling in which the materials are extruded through a heated nozzle (Calvert et al., 1997). Fiber-filled epoxy resins and elastomers have also been demonstrated by the DIW technique (Frutiger et al., 2015). However, studies reporting the printing of natural fibers are very few. Printing heterogeneous natural-fiber-polymer composites by extrusion-based additive manufacturing technologies is challenging due to the poor dispersion of natural fibers, which usually have a significant variation in dimensions. For extrusion-based AM approaches, one of the critical prerequisites is the ink homogeneity, to avoid the typical nozzle clogging issue.

Based on the findings in ink preparation of Chapter 6, herein, we report the DIW of bio-compatible surface-modified short flax elastomer composites with tunable mechanical properties using the sonication-based surface modification approach toward a novel and sustainable method to engineer composites via AM technique.

7.2 Fabrication of Natural Fiber Reinforced Composite Specimens

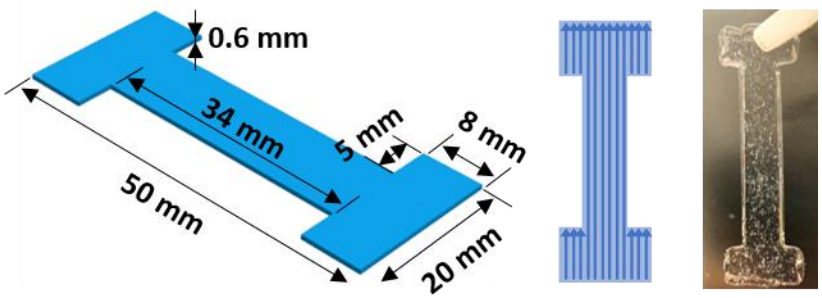

FIG. 33. Geometry and fabrication process of natural fiber reinforced composites.

In this study, a single-layer sample with "I" shape geometry was designed for mechanical characterization, as shown in **Fig. 33**. Filaments were printed in the same direction with a 2 mm distance between each filament. To write those samples, a 1.37 mm inner diameter stainless steel tip was used to extrude inks onto a glass substrate. The standoff distance was 0.5 mm. The printing speed was 18 mm/s, and the input air pressure was 1.0 psi. The printing temperature was evaluated up to 100 ℃ to rapidly solidify the samples.

7.3 Mechanical Behavior of Natural Fiber Reinforced Composites

The tensile strengths of the printed 0 wt%, 0.2 wt%, and 0.5 wt% surface-modified short flax fiber elastomer composites specimens are presented in **Fig. 34a**. The measurements were conducted using an Instron 5942 tensile tester. Both 0.2 wt% and 0.5 wt% flax elastomer composites revealed an approximately 122% increase (from 1800 kPa to 4000 kPa) in tensile strength, compared with the pure elastomer. However, when the fiber loading fraction increases from 0.2 wt% to 0.5 wt%, the tensile strength of the composite did not reveal a noticeable difference. Many studies have reported that the addition of natural and synthetic fibers is beneficial for improving tensile strength (Ramesh et al., 2017). However, the loading fraction was usually much higher in those studies compared to the present work, and the samples were mostly fabricated using injection molding or subtractive manufacturing approaches. For example, to achieve an approximate 100% increase in the tensile strength in the elastomer-based composite, it requires at least a 1.0 wt% carbon fiber loading fraction (Tibbetts et al., 1999), whereas adding only 0.2 wt% of flax fibers is sufficient in the present case. The increased tensile strength is beneficial for many elastomer-based applications, including soft robotics under harsh conditions where a high bearing capability is required.

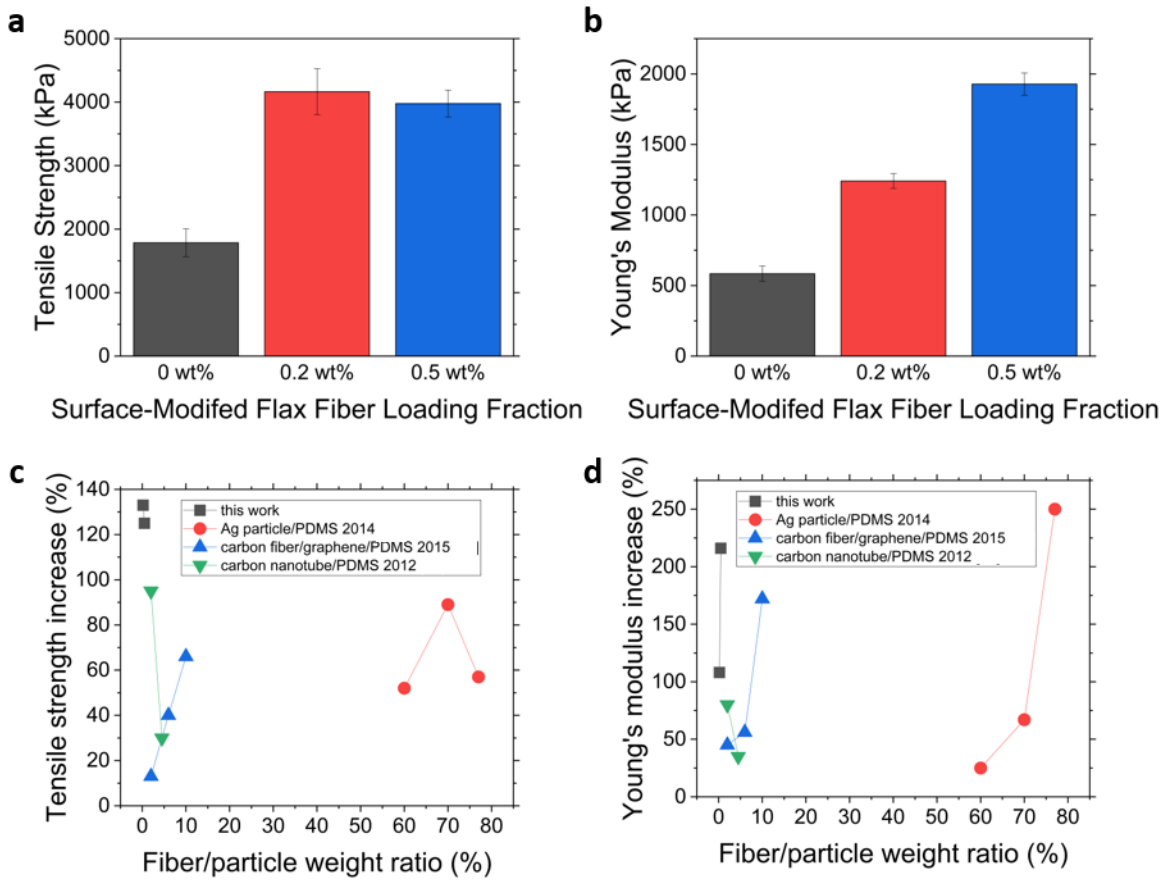

FIG. 34. Mechanical behavior of surface-modified short flax composites. (a) Measured tensile strength of flax elastomer composites. **(b)** Measured Young's modulus of flax elastomer composites. **(c)** Tensile strength of flax-reinforced and other synthetic fibers/particles with different loading fractions. **(d)** Young's modulus of flax-reinforced and other synthetic fibers/particles with different loading fractions.

The measured Young's moduli with different fiber loading fractions are presented in **Fig. 34b**. The average Young's modulus increases from 580 kPa to 1250 kPa and 1860 kPa after adding 0.2 wt% and 0.5 wt% flax fibers, respectively. The increase in Young's modulus associated with the increase in fiber loading reveals a similar trend to many natural fiber-embedded polymer composites fabricated by conventional methods, such as injection molding and subtractive

manufacturing (Ku et al., 2011). However, the enhancement in stiffness in these traditional approaches arises solely from the randomly distributed fibers within the entire polymer matrix, without any local control of more complex structures. Our approach enables a spatial control of fiber distribution by varying the printing process layer-wise and partially adjusting the printing pattern.

As summarized in **Fig. 34c** and **Fig. 34d**, both tensile strength and Young's modulus of the proposed flax elastomer composites can be adjusted by adding a much smaller amount of surface-modified short flax fibers, in comparison with many synthetic fibers and particles, e.g., such as carbon fibers, Ag particles, PVDF fibers, and low-dimensional carbon-based materials-embedded elastomer-based composites (Jiang et al., 2020a).

7.4 Fabrication of Transparent Natural Fiber Composites

Although the surface-modification processes have been developed to transfer raw fibers into a more appropriate form for DIW, the composites based on surface-modified fibers still suffer from inferior light transmittance, limiting their capability in potential optical applications. To increase the transparency of plant-based composites, methods based on high-pressure homogenizer treatment and grinder treatment have been explored (Amiri et al., 2015). These methods usually start from pre-fibrillated pulp instead of raw fibers, possibly due to the homogeneity considerations. Although the obtained light transmittance was outstanding, these processes still require more than 10 times of the physical treatment repetitions. Also, the fabricated composites are limited to simple macroscale geometries, and the compatibility of these natural fiber-reinforced composites with next-generation manufacturing technologies is relatively poor (Christ et al., 2015). Against this background, we present the preparation of highly transparent composites from raw flax fibers using a simple sonication/chemical treatment approach. The developed composites exhibit excellent printability in extrusion-based AM processes, which allows the fabrication of microscale composite objects using plant-based materials. The findings in this study indicate a novel and sustainable method to engineer composites for future functional devices in multiplex geometries with transparent characteristics.

Fig. 35 summarizes the preparation processes of transparent flax fibers (TFFs) from such raw fibers. Long flax fibers with 20 to 200 μm diameter were first chopped into 1 to 3 mm pieces. As shown in **Fig. 35a**, plenty of large dark-colored bundles were observed under the microscope, which can degrade the homogeneity of the prepared composites. To eliminate the inhomogeneity and improve the dispersion of flax fibers, the chopped raw flax fibers were soaked in nitric acid (70%, Sigma-Aldrich) for 15 min to dissolve the pectin content for separating large bundles.

Afterward, the acid-treated flax fibers were washed by deionized (DI) water to remove residual acids. The obtained fibers were then immersed in DI water for a 30 min probe sonicating process (450-Watt, 12 mm probe diameter). The sonication process detached the primary wall of the fiber, leaving well-dispersed repeatable fibers without agglomeration, which are appropriate to further improve the composite printability (**Fig. 35b**).

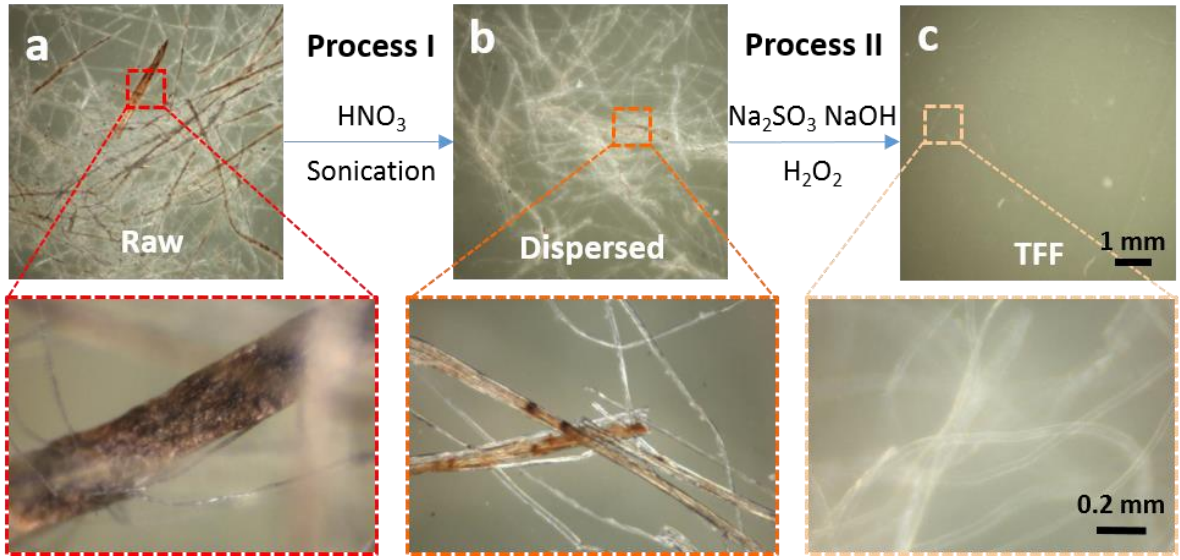

FIG. 35. Transparent natural fiber preparation. (a) Raw flax fiber. **(b)** Dispersed flax fiber after acid-treatment and sonication process. **(c)** Lignin-removed flax fiber.

In the secondary wall structure of flax fibers, despite cellulose and hemicelluloses are optically colorless, lignin exhibits a significantly complicated structure with dark brown color (Zhu et al., 2016). Therefore, natural fibers always appear nontransparent. To remove the dark-colored lignin content, chemicals and processes utilized in conventional paper pulping techniques were used in this study. Briefly, acid-treated flax fibers were soaked in 2.5 mol/L NaOH and 0.4 mol/L Na_2SO_3 in DI water at 90 °C for 6 h (Process I) to partially dissolve the lignin content. Then the fibers were transferred into 2.5 mol/L H_2O_2 in DI water at room temperature for another 72 h

(Process II) to remove the remaining lignin. The as-obtained TFFs were preserved in ethanol. As expected, the fiber color becomes lighter as lignin was gradually removed, and eventually the fibers become transparent, as shown in **Fig. 35c** (Jiang et al., 2020b).

To further prepare the TFF composite, Dow Sylgard 184 silicone elastomer was purchased and used as received. It is a two-component (base and curing agent, mix weight ratio 10:1), room temperature curing polymer. In this study, we prepared TFF composites with loading fractions ranging from 1 to 10 wt%. TFFs were first mixed with the elastomer base at 2000 rpm for 30 min and degassed (AR-100, Thinky) for 2 min. Afterward, they were blended with the curing agent at 2000 rpm for 3 min before loading into a customized aluminum mold with a corresponding specimen dimension of 50 mm × 20 mm × 1.5 mm. The TFF composites were heated at 100 °C for 30 min to thoroughly solidify them for further optical and mechanical characterization.

7.5 Transparency of Natural Fiber Reinforced Composites

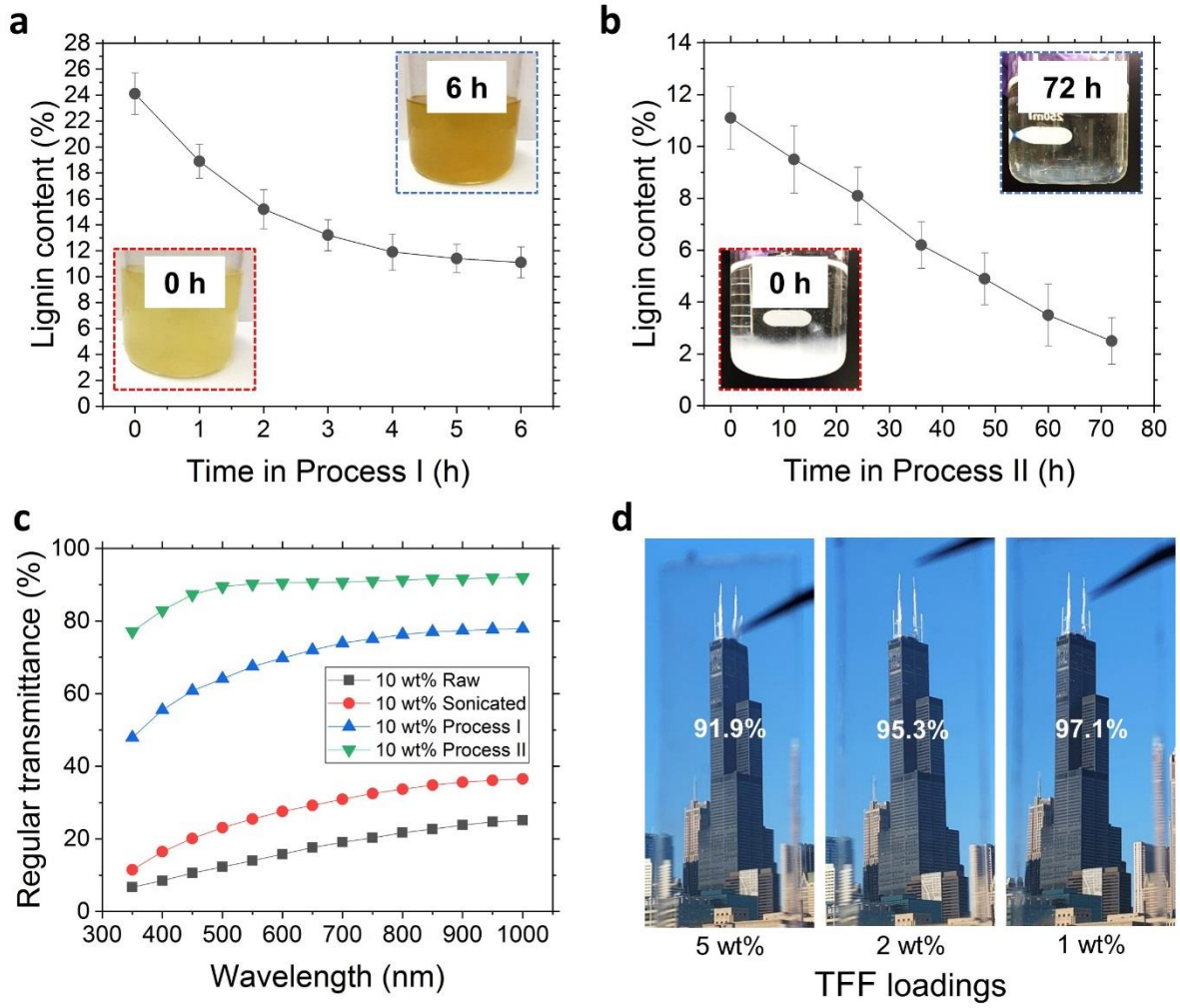

FIG. 36. Natural fiber transparency investigation. (a) Time-dependent lignin content in Process I, 95% CI. **(b)** Time-dependent lignin content in Process II, 95% CI. **(c)** Light transmittance characterizations. **(d)** Demonstration of TFF composites under sunlight with different TFF loadings, light transmittance characterized at 700 nm wavelength.

To investigate the influence of treatment time in both processes I and II on removing lignin for printable natural fiber composites, we quantified the removed lignin content in the flax fibers using the standard methods for lignin determination (Technical Association of Pulp and Paper

Industry Standard Method T 222-om-83). Briefly, fully dried flax fibers (1.0 g, the mass denoted m_0) were measured and extracted with ethanol for 6 h, which was then slowly stirred with cold 72% H_2SO_4 for 2 h. The mixtures were then transferred to a beaker and diluted to 3% by adding DI water and boiled for 4 h. After cooling down, they were filtered and washed using DI water. The insoluble materials were dried and weighed (the mass denoted m_1). The lignin content was calculated as m_1/m_0. As shown in **Fig. 36a**, the lignin was removed rapidly within the first 3 h in Process I, with an up to 45% removal. Afterward, the remaining lignin was further removed in Process II (**Fig. 36b**). Because lignin is colored, while cellulose and hemicellulose are colorless, the color of the fiber indicates the amount of lignin left. As expected, the color becomes lighter as more lignin is removed.

Fig. 36c depicts the measured regular light transmittance of the prepared flax-fiber composite samples at different processing stages. The tested fibers were stored in the elastomer at the 10 wt% fiber loading. The light transmittance of the composites was measured by a spectrophotometer in the 350 to 1000 nm wavelength range. The results revealed that samples after both Process I and Process II demonstrated a significant improvement in light transmission. Specifically, the flax fibers after Process II (TFFs) exhibited superior optical properties, and the prepared composites revealed an up to 95% regular transmittance. In addition, we found that by separating large fiber bundles, the light transmittance of sonicated fibers increased up to 90% compared with raw flax fibers. Afterward, we prepared TFF composites using the aforementioned mold with various TFF loadings and tested them under sunlight (**Fig. 36d**). As expected, although a lower TFF loading exhibits a slightly higher light transmittance, all the specimens with typical fiber loadings revealed superior performance.

7.6 Mechanical Behavior of Transparent Composites

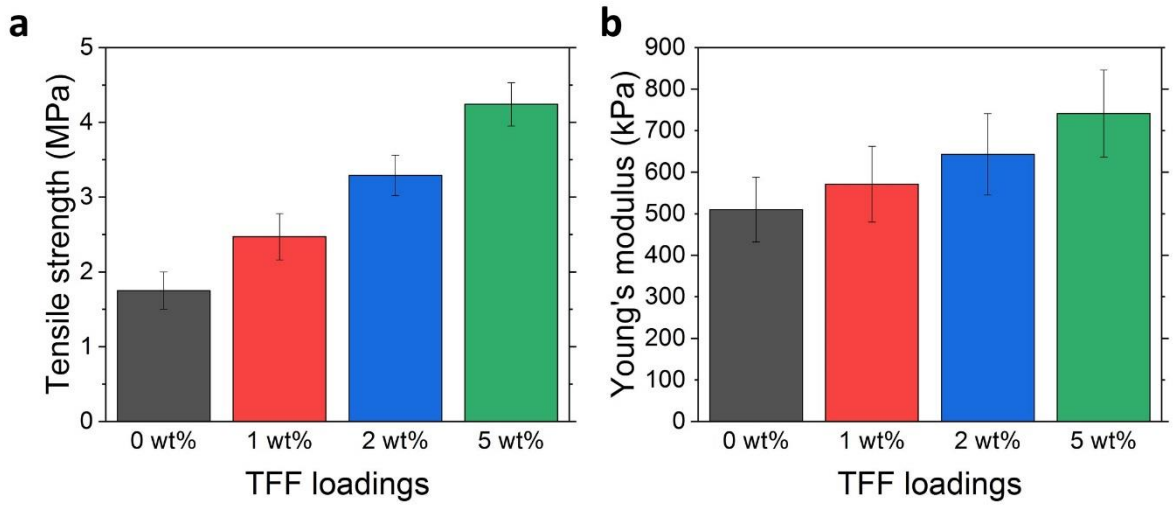

FIG. 37. Mechanical properties of transparent natural fiber composites. (a) Tensile strength of TFF composites, 95% CI. **(b)** Young's modules of TFF composites, 95% CI.

The tensile strengths of TFF composites with different fiber loadings are presented in **Fig. 37a**. The measurements were conducted using an Instron 2710-205 tensile tester. The measured tensile strength ranged from 2.5 to 4.2 MPa when the fiber loading increased from 1 to 5 wt%. Compared with pure elastomer, the 1 wt%, 2 wt%, and 5 wt% specimens revealed approximately 41%, 88%, and 142% increases in tensile strength, respectively. On the other hand, the measured Young's moduli with different fiber loading fractions are presented in **Fig. 37b**. Young's modulus characterizing stiffness was increased by 12%, 26%, and 46% after adding 1 wt%, 2 wt%, and 5 wt% TFFs into the elastomer, respectively. The findings related to both tensile strength and Young's modulus indicated a typical trend in non-transparent natural fiber-reinforced composites (Ku et al., 2011). By removing the lignin content, the concentration of cellulose can be increased. Since cellulose has the actual fiber structure, while lignin only serves as binders to conglutinate fiber cells (Sanjay et al., 2018), the method of flax fiber treatment proposed in this study is

beneficial to improve the overall mechanical reinforcement in composite structures. It should also be noted that the present transparent natural-fiber composites are competitive to many synthetic-fiber reinforced elastomer composites.

7.7 Printability of Transparent Composites

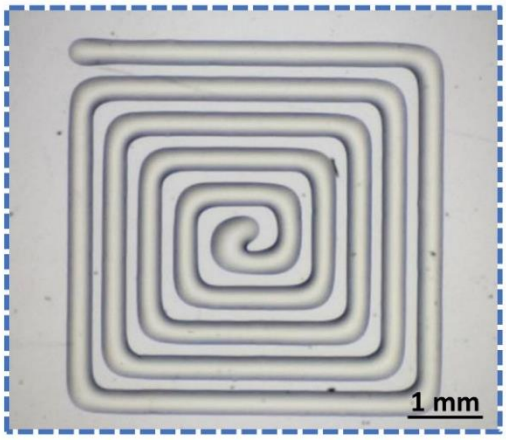

FIG. 38. Printability of transparent natural fiber composites.

As demonstrated in **Fig. 38**, the width of the printed filaments in the "loop" pattern is approximately 275 ± 15 μm, and the printing is free of any fiber agglomeration/inhomogeneity related defects, which confirms the excellent printability of the developed TFF composites in modern AM systems.

CONCLUSION & FUTURE RESEARCH

Motivated by the increasing demand for printable materials in additive manufacturing (AM), this dissertation investigated the direct ink writing (DIW) process of fiber composites for fabricating functional devices. The objective is to develop a fundamental understanding of the complicated correlation between ink properties, DIW printing process, and printed composite functionalities. Three hypotheses were examined in this study, and the corresponding inferences were drawn.

We first developed the DIW setup in Chapter 2 by modifying a dispensing robot to investigate the DIW process. A normalized method for predicting printed filament geometry for a broad type of materials was introduced in Chapter 2. Such process modeling methods could provide a fundamental guideline for the DIW process of fiber composites through identifying appropriate process settings for accurately achieving desired filament geometries.

Chapter 3 confirmed that the incorporation of an electric field between the printing nozzle and the substrate induces an electrowetting effect. Such electrowetting effect enlarges the printable ranges of materials and the working range of manufacturing process settings, as well as improves the printing accuracy. The proposed electrowetting-assisted process can modify the substrate's wetting properties dynamically, resulting in a more than 150% increase in ink throughput.

Chapter 4 verified that the addition of water-washable gel could change the storage modulus and loss modulus of the synthetic fiber suspensions to enhance viscoelastic and shear-thinning properties, increasing the printability of synthetic fiber inks and allowing for higher fiber contents in the composite. As a test case, Chapter 5 presented a thermoresponsive supercapacitor design and fabrication strategy using synthetic fiber composites for self-protective wearable supercapacitor against the common thermal runaway issue of high-performance electrochemical devices. With the

addition of water-washable gel, a less than 200 µm printing resolution was achieved, which was among the best in recently reported printable fiber composites.

Chapter 6 confirmed that the probe sonication process efficiently removes the primary wall of natural fibers and hence increases the printability of natural fibers in DIW while retaining its mechanical characteristics in the printed composite. Using the sonication method, the printability of natural fiber composites was enabled with an as high as 91% successful extrusion rate. As a test case, Chapter 7 reported the DIW of bio-compatible sonicated natural fiber composites with considerably improved mechanical properties with a more than 100% tensile strength increase.

Future research extensions include investigating the DIW process for continuous fiber-based composites and multi-material fabrication for structures with higher geometrical complexity. The influence of the electric field on the wettability of materials and surface energy in a multi-layer construction needs to be studied. Further research will also include the analysis of defects formation and elimination of the DIW process at a three-dimensional material interface.

CITED LITERATURE

Abilash, N., & Sivapragash, M. J. K. S. U. (2016). Optimizing the delamination failure in bamboo fiber reinforced polyester composite. Journal of King Saud University-Engineering Sciences, 28(1), 92-102.

Ahmad, F., Choi, H. S., & Park, M. K. (2015). A review: natural fiber composites selection in view of mechanical, light weight, and economic properties. Macromolecular materials and engineering, 300(1), 10-24.

Ahmed, E. M. (2015). Hydrogel: Preparation, characterization, and applications: A review. Journal of advanced research, 6(2), 105-121.

Akhoundi, B., Behravesh, A. H., & Bagheri Saed, A. (2019). Improving mechanical properties of continuous fiber-reinforced thermoplastic composites produced by FDM 3D printer. Journal of Reinforced Plastics and Composites, 38(3), 99-116.

Al-Saleh, M. H., & Sundararaj, U. (2009). A review of vapor grown carbon nanofiber/polymer conductive composites. Carbon, 47(1), 2-22.

Amiri, A., Ulven, C. A., & Huo, S. (2015). Effect of chemical treatment of flax fiber and resin manipulation on service life of their composites using time-temperature superposition. Polymers, 7(10), 1965-1978.

An, K. H., Kim, W. S., Park, Y. S., Choi, Y. C., Lee, S. M., Chung, D. C., ... & Lee, Y. H. (2001). Supercapacitors using single-walled carbon nanotube electrodes. Advanced Materials, 13(7), 497-500.

Arai, S., Tsunoda, S., Kawamura, R., Kuboyama, K., & Ougizawa, T. (2017). Comparison of crystallization characteristics and mechanical properties of poly (butylene terephthalate) processed by laser sintering and injection molding. Materials & Design, 113, 214-222.

Athreya, S. R., Kalaitzidou, K., & Das, S. (2011). Mechanical and microstructural properties of Nylon-12/carbon black composites: Selective laser sintering versus melt compounding and injection molding. Composites science and technology, 71(4), 506-510.

Bai, J., Goodridge, R. D., Hague, R. J., Song, M., & Murakami, H. (2014). Nanostructural characterization of carbon nanotubes in laser-sintered polyamide 12 by 3D-TEM. Journal of Materials Research, 29(17), 1817.

Bakis, C. E., Bank, L. C., Brown, V., Cosenza, E., Davalos, J. F., Lesko, J. J., ... & Triantafillou, T. C. (2002). Fiber-reinforced polymer composites for construction—State-of-the-art review. Journal of composites for construction, 6(2), 73-87.

Balla, V. K., Kate, K. H., Satyavolu, J., Singh, P., & Tadimeti, J. G. D. (2019). Additive manufacturing of natural fiber reinforced polymer composites: Processing and prospects. Composites Part B: Engineering, 174, 106956.

Bártolo, P. J. (Ed.). (2011). Stereolithography: materials, processes and applications. Springer Science & Business Media.

Bateni, A., Laughton, S., Tavana, H., Susnar, S. S., Amirfazli, A., & Neumann, A. W. (2005). Effect of electric fields on contact angle and surface tension of drops. Journal of colloid and interface science, 283(1), 215-222.

Boley, J. W., White, E. L., Chiu, G. T. C., & Kramer, R. K. (2014). Direct writing of gallium-indium alloy for stretchable electronics. Advanced Functional Materials, 24(23), 3501-3507.

Boparai, K. S., Singh, R., & Singh, H. (2016). Development of rapid tooling using fused deposition modeling: a review. Rapid Prototyping Journal.

Buckley, J. D., & Edie, D. D. (Eds.). (1993). Carbon-carbon materials and composites. William Andrew.

Calvert, P., Lin, T. L., & Martin, H. (1997). Extrusion freeform fabrication of chopped-fibre reinforced composites. High Performance Polymers, 9(4), 449-456.

Charlet, K., Eve, S., Jernot, J. P., Gomina, M., & Breard, J. (2009). Tensile deformation of a flax fiber. Procedia Engineering, 1(1), 233-236.

Cheah, C. M., Fuh, J. Y. H., Nee, A. Y. C., & Lu, L. (1999). Mechanical characteristics of fiber-filled photo-polymer used in stereolithography. Rapid Prototyping Journal.

Chen, B., Jiang, Y., Tang, X., Pan, Y., & Hu, S. (2017). Fully packaged carbon nanotube supercapacitors by direct ink writing on flexible substrates. ACS applied materials & interfaces, 9(34), 28433-28440.

Chiappone, A., Roppolo, I., Naretto, E., Fantino, E., Calignano, F., Sangermano, M., & Pirri, F. (2017). Study of graphene oxide-based 3D printable composites: Effect of the in situ reduction. Composites Part B: Engineering, 124, 9-15.

Chiu, S. H., Wicaksono, S. T., Chen, K. T., Chen, C. Y., & Pong, S. H. (2015). Mechanical and thermal properties of photopolymer/CB (carbon black) nanocomposite for rapid prototyping. Rapid Prototyping Journal.

Christ, S., Schnabel, M., Vorndran, E., Groll, J., & Gbureck, U. (2015). Fiber reinforcement during 3D printing. Materials Letters, 139, 165-168.

Chung, H., & Das, S. (2006). Processing and properties of glass bead particulate-filled functionally graded Nylon-11 composites produced by selective laser sintering. Materials Science and Engineering: A, 437(2), 226-234.

Chunze, Y., Yusheng, S., Jinsong, Y., & Jinhui, L. (2009). A nanosilica/nylon-12 composite powder for selective laser sintering. Journal of Reinforced Plastics and Composites, 28(23), 2889-2902.

Compton, B. G., & Lewis, J. A. (2014). 3D-printing of lightweight cellular composites. Advanced materials, 26(34), 5930-5935.

Cui, X., Lv, R., Sagar, R. U. R., Liu, C., & Zhang, Z. (2015). Reduced graphene oxide/carbon nanotube hybrid film as high performance negative electrode for supercapacitor. Electrochimica Acta, 169, 342-350.

Deng, D., Jain, A., Yodvanich, N., Araujo, A., & Chen, Y. (2016, August). Three-dimensional circuit fabrication using four-dimensional printing and direct ink writing. In 2016 International Symposium on Flexible Automation (ISFA) (pp. 286-291). IEEE.

DicCbshfsE, J., Abd Rahim, M. K., Samsuri, N. A., Salim, H. A. M., & Ali, M. F. (2011). Embroidered fully textile wearable antenna for medical monitoring applications. Progress In Electromagnetics Research, 117, 321-337.

Dresselhaus, M. S., Dresselhaus, G., Eklund, P. C., & Rao, A. M. (2000). Carbon nanotubes. In The physics of fullerene-based and fullerene-related materials (pp. 331-379). Springer, Dordrecht.

Duineveld, P. C. (2003). The stability of ink-jet printed lines of liquid with zero receding contact angle on a homogeneous substrate. Journal of Fluid Mechanics, 477, 175-200.

Dulieu-Barton, J. M., & Fulton, M. C. (2000). Mechanical properties of a typical stereolithography resin. Strain, 36(2), 81-87.

Ebbesen, T. W., Lezec, H. J., Hiura, H., Bennett, J. W., Ghaemi, H. F., & Thio, T. (1996). Electrical conductivity of individual carbon nanotubes. Nature, 382(6586), 54-56.

Fan, D. W., Kim, H. S., & De Cooman, B. C. (2009). A review of the physical metallurgy related to the hot press forming of advanced high strength steel. Steel Research International, 80(3), 241-248.

Feng, X., Ouyang, M., Liu, X., Lu, L., Xia, Y., & He, X. (2018). Thermal runaway mechanism of lithium ion battery for electric vehicles: A review. Energy Storage Materials, 10, 246-267.

Franchin, G., Wahl, L., & Colombo, P. (2017). Direct ink writing of ceramic matrix composite structures. Journal of the American Ceramic Society, 100(10), 4397-4401.

Friedrich, L., & Begley, M. (2018). In situ characterization of low-viscosity direct ink writing: Stability, wetting, and rotational flows. Journal of colloid and interface science, 529, 599-609.

Friedrich, L., Collino, R., Ray, T., & Begley, M. (2017). Acoustic control of microstructures during direct ink writing of two-phase materials. Sensors and Actuators A: Physical, 268, 213-221.

Frutiger, A., Muth, J. T., Vogt, D. M., Mengüç, Y., Campo, A., Valentine, A. D., ... & Lewis, J. A. (2015). Capacitive soft strain sensors via multicore–shell fiber printing. Advanced Materials, 27(15), 2440-2446.

Gao, C., Lee, S. W., & Yang, Y. (2017). Thermally regenerative electrochemical cycle for low-grade heat harvesting. ACS Energy Letters, 2(10), 2326-2334.

Gardner, J. M., Sauti, G., Kim, J. W., Cano, R. J., Wincheski, R. A., Stelter, C. J., ... & Siochi, E. J. (2016). 3-D printing of multifunctional carbon nanotube yarn reinforced components. Additive Manufacturing, 12, 38-44.

Garkhail, S. K., Heijenrath, R. W. H., & Peijs, T. (2000). Mechanical properties of natural-fibre-mat-reinforced thermoplastics based on flax fibres and polypropylene. Applied Composite Materials, 7(5-6), 351-372.

Ge, Q., Dunn, C. K., Qi, H. J., & Dunn, M. L. (2014). Active origami by 4D printing. Smart Materials and Structures, 23(9), 094007.

Gibson, I., Rosen, D. W., & Stucker, B. (2014). Additive manufacturing technologies (Vol. 17). New York: Springer.

Gill, T. J., & Hon, K. K. B. (2004). Experimental investigation into the selective laser sintering of silicon carbide polyamide composites. Proceedings of the Institution of Mechanical Engineers, Part B: Journal of Engineering Manufacture, 218(10), 1249-1256.

Goh, G. D., Yap, Y. L., Agarwala, S., & Yeong, W. Y. (2019). Recent progress in additive manufacturing of fiber reinforced polymer composite. Advanced Materials Technologies, 4(1), 1800271.

Goodridge, R. D., Shofner, M. L., Hague, R. J., McClelland, M., Schlea, M. R., Johnson, R. B., & Tuck, C. J. (2011). Processing of a Polyamide-12/carbon nanofibre composite by laser sintering. Polymer Testing, 30(1), 94-100.

Gratson, G. M., Xu, M., & Lewis, J. A. (2004). Direct writing of three-dimensional webs. nature, 428(6981), 386-386.

Gu, J., Lv, Z., Wu, Y., Guo, Y., Tian, L., Qiu, H., ... & Zhang, Q. (2017). Dielectric thermally conductive boron nitride/polyimide composites with outstanding thermal stabilities via in-situ polymerization-electrospinning-hot press method. Composites Part A: Applied Science and Manufacturing, 94, 209-216.

Gupta, A., & Ogale, A. A. (2002). Dual curing of carbon fiber reinforced photoresins for rapid prototyping. Polymer composites, 23(6), 1162-1170.

Gupta, M., & Wang, K. K. (1993). Fiber orientation and mechanical properties of short-fiber-reinforced injection-molded composites: Simulated and experimental results. Polymer Composites, 14(5), 367-382.

Gurr, M., Hofmann, D., Ehm, M., Thomann, Y., Kübler, R., & Mülhaupt, R. (2008). Acrylic nanocomposite resins for use in stereolithography and structural light modulation based rapid prototyping and rapid manufacturing technologies. Advanced Functional Materials, 18(16), 2390-2397.

Hahn, H. T., & Tsai, S. W. (1980). Introduction to composite materials. CRC Press.

Haleem, A., & Javaid, M. (2019). Additive manufacturing applications in industry 4.0: a review. Journal of Industrial Integration and Management, 4(04), 1930001.

Hammami, A., Raymond, N., & Armand, M. (2003). Runaway risk of forming toxic compounds. Nature, 424(6949), 635-636.

Harish, S., Michael, D. P., Bensely, A., Lal, D. M., & Rajadurai, A. (2009). Mechanical property evaluation of natural fiber coir composite. Materials characterization, 60(1), 44-49.

Hartl, D. J., & Lagoudas, D. C. (2007). Aerospace applications of shape memory alloys. Proceedings of the Institution of Mechanical Engineers, Part G: Journal of Aerospace Engineering, 221(4), 535-552.

Hofmann, A., Uhlmann, N., Ziebert, C., Wiegand, O., Schmidt, A., & Hanemann, T. (2017). Preventing Li-ion cell explosion during thermal runaway with reduced pressure. Applied Thermal Engineering, 124, 539-544.

Huang, X., & Netravali, A. (2007). Characterization of flax fiber reinforced soy protein resin based green composites modified with nano-clay particles. Composites Science and Technology, 67(10), 2005-2014.

Ivey, M., Melenka, G. W., Carey, J. P., & Ayranci, C. (2017). Characterizing short-fiber-reinforced composites produced using additive manufacturing. Advanced Manufacturing: Polymer & Composites Science, 3(3), 81-91.

Jiang, Y., Hu, S., & Pan, Y. (2018). A Normalized Trace Geometry Modeling Method with Bulge-Free Analysis for Direct Ink Writing Process Planning. 3D Printing and Additive Manufacturing, 5(4), 301-310.

Jiang, Y., Cheng, M., Shahbazian-Yassar, R., & Pan, Y. (2019). Direct Ink Writing of Wearable Thermoresponsive Supercapacitors with rGO/CNT Composite Electrodes. Advanced Materials Technologies, 4(12), 1900691.

Jiang, Y., Plog, J., Yarin, A. L., & Pan, Y. (2020). Direct ink writing of surface-modified flax elastomer composites. Composites Part B: Engineering, 108061.

Jiang, Y., Yarin, A. L., & Pan, Y. (2020). Printable highly transparent natural fiber composites. Materials Letters, 277, 128290.

Kang, K. H. (2002). How electrostatic fields change contact angle in electrowetting. Langmuir, 18(26), 10318-10322.

Karalekas, D., & Antoniou, K. (2004). Composite rapid prototyping: overcoming the drawback of poor mechanical properties. Journal of materials processing technology, 153, 526-530.

Kemp, J. W., Hmeidat, N. S., & Compton, B. G. (2020). Boron nitride-reinforced polysilazane-derived ceramic composites via direct-ink writing. Journal of the American Ceramic Society.

Kim, Y., Yuk, H., Zhao, R., Chester, S. A., & Zhao, X. (2018). Printing ferromagnetic domains for untethered fast-transforming soft materials. Nature, 558(7709), 274-279.

Ku, H., Wang, H., Pattarachaiyakoop, N., & Trada, M. (2011). A review on the tensile properties of natural fiber reinforced polymer composites. Composites Part B: Engineering, 42(4), 856-873.

Lewis, J. A., Smay, J. E., Stuecker, J., & Cesarano, J. (2006). Direct ink writing of three-dimensional ceramic structures. Journal of the American Ceramic Society, 89(12), 3599-3609.

Liu, Y., Song, Y., Niu, S., Zhang, Y., Han, Z., & Ren, L. (2016). Integrated super-hydrophobic and antireflective PDMS bio-templated from nano-conical structures of cicada wings. RSC advances, 6(110), 108974-108980.

López Manchado, M. A., Arroyo, M., Biagiotti, J., & Kenny, J. M. (2003). Enhancement of mechanical properties and interfacial adhesion of PP/EPDM/flax fiber composites using maleic anhydride as a compatibilizer. Journal of Applied Polymer Science, 90(8), 2170-2178.

Lu, L., Tang, X., Hu, S., & Pan, Y. (2018). Acoustic field-assisted particle patterning for smart polymer composite fabrication in stereolithography. 3D Printing and Additive Manufacturing, 5(2), 151-159.

M'barki, A., Bocquet, L., & Stevenson, A. (2017). Linking rheology and printability for dense and strong ceramics by direct ink writing. Scientific reports, 7(1), 1-10.

Mata, A., Fleischman, A. J., & Roy, S. (2005). Characterization of polydimethylsiloxane (PDMS) properties for biomedical micro/nanosystems. Biomedical microdevices, 7(4), 281-293.

Matsuzaki, R., Ueda, M., Namiki, M., Jeong, T. K., Asahara, H., Horiguchi, K., ... & Hirano, Y. (2016). Three-dimensional printing of continuous-fiber composites by in-nozzle impregnation. Scientific reports, 6, 23058.

Melenka, G. W., Cheung, B. K., Schofield, J. S., Dawson, M. R., & Carey, J. P. (2016). Evaluation and prediction of the tensile properties of continuous fiber-reinforced 3D printed structures. Composite Structures, 153, 866-875.

Meyer, R. (2012). Handbook of pultrusion technology. Springer Science & Business Media.

Mohan, N., Senthil, P., Vinodh, S., & Jayanth, N. (2017). A review on composite materials and process parameters optimisation for the fused deposition modelling process. Virtual and Physical Prototyping, 12(1), 47-59.

Mohanty, A. K., Khan, M. A., & Hinrichsen, G. (2000). Surface modification of jute and its influence on performance of biodegradable jute-fabric/Biopol composites. Composites science and technology, 60(7), 1115-1124.

Morent, R., De Geyter, N., Axisa, F., De Smet, N., Gengembre, L., De Leersnyder, E., ... & Payen, E. (2007). Adhesion enhancement by a dielectric barrier discharge of PDMS used for flexible and stretchable electronics. Journal of Physics D: Applied Physics, 40(23), 7392.

MR, S., Siengchin, S., Parameswaranpillai, J., Jawaid, M., Pruncu, C. I., & Khan, A. (2018). A comprehensive review of techniques for natural fibers as reinforcement in composites.

Ngo, T. D., Kashani, A., Imbalzano, G., Nguyen, K. T., & Hui, D. (2018). Additive manufacturing (3D printing): A review of materials, methods, applications and challenges. Composites Part B: Engineering, 143, 172-196.

Ning, F., Cong, W., Qiu, J., Wei, J., & Wang, S. (2015). Additive manufacturing of carbon fiber reinforced thermoplastic composites using fused deposition modeling. Composites Part B: Engineering, 80, 369-378.

Orue, A., Jauregi, A., Unsuain, U., Labidi, J., Eceiza, A., & Arbelaiz, A. (2016). The effect of alkaline and silane treatments on mechanical properties and breakage of sisal fibers and poly (lactic acid)/sisal fiber composites. Composites Part A: Applied Science and Manufacturing, 84, 186-195.

Parandoush, P., & Lin, D. (2017). A review on additive manufacturing of polymer-fiber composites. Composite Structures, 182, 36-53.

Patel, J. P., Patel, C. P., & Patel, U. J. (2012). A review on various approach for process parameter optimization of fused deposition modeling (FDM) process and Taguchi approach for optimization. International Journal of Engineering Research and Applications, 2(2), 361-365.

Pech, D., Brunet, M., Taberna, P. L., Simon, P., Fabre, N., Mesnilgrente, F., ... & Durou, H. (2010). Elaboration of a microstructured inkjet-printed carbon electrochemical capacitor. Journal of Power Sources, 195(4), 1266-1269.42

Qiao, P., Davalos, J. F., & Brown, B. (2000). A systematic analysis and design approach for single-span FRP deck/stringer bridges. Composites Part B: Engineering, 31(6-7), 593-609.

Ramesh, M., Palanikumar, K., & Reddy, K. H. (2017). Plant fibre based bio-composites: Sustainable and renewable green materials. Renewable and Sustainable Energy Reviews, 79, 558-584.

Raney, J. R., Compton, B. G., Mueller, J., Ober, T. J., Shea, K., & Lewis, J. A. (2018). Rotational 3D printing of damage-tolerant composites with programmable mechanics. Proceedings of the National Academy of Sciences, 115(6), 1198-1203.

Restrepo, J. J., & Colorado, H. A. (2020). Additive manufacturing of composites made of epoxy resin with magnetite particles fabricated with the direct ink writing technique. Journal of Composite Materials, 54(5), 647-657.

Rocha, V. G., Saiz, E., Tirichenko, I. S., & García-Tuñón, E. (2020). Direct ink writing advances in multi-material structures for a sustainable future. Journal of Materials Chemistry A, 8(31), 15646-15657.

Rosato, D. V., & Rosato, M. G. (2012). Injection molding handbook. Springer Science & Business Media.

Saari, M., Cox, B., Richer, E., Krueger, P. S., & Cohen, A. L. (2015). Fiber encapsulation additive manufacturing: An enabling technology for 3D printing of electromechanical devices and robotic components. 3D Printing and Additive Manufacturing, 2(1), 32-39.

Sakly, A., Kenzari, S., Bonina, D., Corbel, S., & Fournée, V. (2014). A novel quasicrystal-resin composite for stereolithography. Materials & Design (1980-2015), 56, 280-285.

Salmoria, G. V., Ahrens, C. H., Beal, V. E., Pires, A. T. N., & Soldi, V. (2009). Evaluation of post-curing and laser manufacturing parameters on the properties of SOMOS 7110 photosensitive resin used in stereolithography. Materials & Design, 30(3), 758-763.

Sanjay, M. R., Madhu, P., Jawaid, M., Senthamaraikannan, P., Senthil, S., & Pradeep, S. (2018). Characterization and properties of natural fiber polymer composites: A comprehensive review. Journal of Cleaner Production, 172, 566-581.

Schiaffino, S., & Sonin, A. A. (1997). Formation and stability of liquid and molten beads on a solid surface. Journal of fluid mechanics, 343, 95-110.

Singla, A. K., Chawla, M., & Singh, A. (2000). Potential applications of carbomer in oral mucoadhesive controlled drug delivery system: a review. Drug development and industrial pharmacy, 26(9), 913-924.

Skylar-Scott, M. A., Gunasekaran, S., & Lewis, J. A. (2016). Laser-assisted direct ink writing of planar and 3D metal architectures. Proceedings of the National Academy of Sciences, 113(22), 6137-6142.

Smay, J. E., Cesarano, J., & Lewis, J. A. (2002). Colloidal inks for directed assembly of 3-D periodic structures. Langmuir, 18(14), 5429-5437.

Srisuwan, S., Prasoetsopha, N., Suppakarn, N., & Chumsamrong, P. (2014). The effects of alkalized and silanized woven sisal fibers on mechanical properties of natural rubber modified epoxy resin. Energy Procedia, 56, 19-25.

Stoppa, M., & Chiolerio, A. (2014). Wearable electronics and smart textiles: a critical review. sensors, 14(7), 11957-11992.

Stringer, J., & Derby, B. (2010). Formation and stability of lines produced by inkjet printing. Langmuir, 26(12), 10365-10372.

Tekinalp, H. L., Kunc, V., Velez-Garcia, G. M., Duty, C. E., Love, L. J., Naskar, A. K., ... & Ozcan, S. (2014). Highly oriented carbon fiber–polymer composites via additive manufacturing. Composites Science and Technology, 105, 144-150.

Tian, X., Liu, T., Yang, C., Wang, Q., & Li, D. (2016). Interface and performance of 3D printed continuous carbon fiber reinforced PLA composites. Composites Part A: Applied Science and Manufacturing, 88, 198-205.

Tibbetts, G. G., & McHugh, J. J. (1999). Mechanical properties of vapor-grown carbon fiber composites with thermoplastic matrices. Journal of Materials Research, 14(7), 2871-2880.

Tlegenov, Y., Hong, G. S., & Lu, W. F. (2018). Nozzle condition monitoring in 3D printing. Robotics and Computer-Integrated Manufacturing, 54, 45-55.

Valentine, A. D., Busbee, T. A., Boley, J. W., Raney, J. R., Chortos, A., Kotikian, A., ... & Lewis, J. A. (2017). Hybrid 3D printing of soft electronics. advanced Materials, 29(40), 1703817.

Van Der Klift, F., Koga, Y., Todoroki, A., Ueda, M., Hirano, Y., & Matsuzaki, R. (2016). 3D printing of continuous carbon fibre reinforced thermo-plastic (CFRTP) tensile test specimens. Open Journal of Composite Materials, 6(01), 18.

Vinson, J. R., & Chou, T. W. (1975). Composite materials and their use in structures.

Wang, X., Jiang, M., Zhou, Z., Gou, J., & Hui, D. (2017). 3D printing of polymer matrix composites: A review and prospective. Composites Part B: Engineering, 110, 442-458.

Wong, K. V., & Hernandez, A. (2012). A review of additive manufacturing. International scholarly research notices, 2012.

Xie, F., Zhang, T. A., Dreisinger, D., & Doyle, F. (2014). A critical review on solvent extraction of rare earths from aqueous solutions. Minerals Engineering, 56, 10-28.

Yan, C., Hao, L., Xu, L., & Shi, Y. (2011). Preparation, characterisation and processing of carbon fibre/polyamide-12 composites for selective laser sintering. Composites Science and Technology, 71(16), 1834-1841.

Yan, L., Chouw, N., & Yuan, X. (2012). Improving the mechanical properties of natural fibre fabric reinforced epoxy composites by alkali treatment. Journal of Reinforced Plastics and Composites, 31(6), 425-437.

Yang, C., Tian, X., Liu, T., Cao, Y., & Li, D. (2017). 3D printing for continuous fiber reinforced thermoplastic composites: mechanism and performance. Rapid Prototyping Journal.

Yang, Y., Chen, Z., Song, X., Zhang, Z., Zhang, J., Shung, K. K., ... & Chen, Y. (2017). Biomimetic anisotropic reinforcement architectures by electrically assisted nanocomposite 3D printing. Advanced materials, 29(11), 1605750.

You, X., Yang, J., Feng, Q., Huang, K., Zhou, H., Hu, J., & Dong, S. (2018). Three-dimensional graphene-based materials by direct ink writing method for lightweight application. International Journal of Lightweight Materials and Manufacture, 1(2), 96-101.

Zak, G., Haberer, M., Park, C. B., & Benhabib, B. (2000). Mechanical properties of short-fibre layered composites: prediction and experiment. Rapid Prototyping Journal.

Zeng, K., Pal, D., & Stucker, B. (2012, August). A review of thermal analysis methods in laser sintering and selective laser melting. In Proceedings of Solid Freeform Fabrication Symposium Austin, TX (Vol. 60, pp. 796-814).

Zhao, Y. X., Li, H. X., Ding, H., & Xiong, Y. L. (2005). Integrated modelling of a time-pressure fluid dispensing system for electronics manufacturing. The International Journal of Advanced Manufacturing Technology, 26(1-2), 1-9.

Zhong, W., Li, F., Zhang, Z., Song, L., & Li, Z. (2001). Short fiber reinforced composites for fused deposition modeling. Materials Science and Engineering: A, 301(2), 125-130.

Zhu, M., Song, J., Li, T., Gong, A., Wang, Y., Dai, J., ... & Hu, L. (2016). Highly anisotropic, highly transparent wood composites. Advanced materials, 28(26), 5181-5187.

YIZHOU JIANG

Curriculum Vitae

Department of Mechanical and Industrial Engineering
University of Illinois at Chicago
842 W. Taylor St., Chicago, IL 60607
E-mail: yjiang89@uic.edu *Phone*: (312) 522-4146

EDUCATION

Ph.D. Candidate in Industrial Engineering
Emphasis: Advanced Manufacturing Processes
University of Illinois at Chicago, Chicago, IL *12/2020 (Expected)*
Advisor: Dr. Yayue Pan
Thesis: *Direct Ink Writing of Multi-Functional Fiber Composites*
GPA: 4.0/4.0

M.S. in Electrical and Computer Engineering
Emphasis: Computer Vision & Image Processing
University of Illinois at Chicago, Chicago, IL *05/2016*
GPA: 3.9/4.0

B.S. in Automation Engineering
Jilin University, Changchun, China *07/2015*
GPA: 3.5/4.0

HONORS AND AWARDS

Dean's Scholar Fellowship Nominee
University of Illinois at Chicago, Chicago, IL *03/2020*

Graduate College Student Presenter Award
University of Illinois at Chicago, Chicago, IL *11/2017*

Graduate Student Council Travel Award
University of Illinois at Chicago, Chicago, IL *11/2017*

Excellence Award
2014 Freescale Cup National University Student Intelligent Car Race *08/2014*

Jilin University Outstanding Student Award (top 3%)
Jilin University, Changchun, China *06/2012*

Communication Engineering Department Scholarship
Jilin University, Changchun, China *06/2012*

ACCEPTED JOURNAL ARTICLES

[J1] **Jiang, Y.**, Hu, S., Pan, Y. (2018). A normalized trace geometry modeling method with bulge-free analysis for direct ink writing process planning. *3D Printing and Additive Manufacturing.* 5(4), 301.

[J2] **Jiang, Y.**, Cheng, M., Shahbazian-Yassar, R., Pan, Y. (2019). Direct ink writing of wearable thermoresponsive supercapacitors with rGO/CNT composite electrodes. *Advanced Materials Technologies.* 4(12), 1900691.

[J3] **Jiang, Y.**, Plog, J., Yarin, A. L., Pan, Y. (2020). Direct ink writing of surface-modified flax elastomer composites with programmable mechanics. *Composites Part B: Engineering*. 108061.

[J4] **Jiang, Y.**, Wang, Y., Lichade, K. M., He, H., Feinerman, A., Pan, Y. (2020). Textured window design for continuous projection stereolithography process. *Manufacturing Letters.*

[J5] **Jiang, Y.**, Wang, Y., He, H., Feinerman, A., Pan, Y. (2020). Constrained window design in projection stereolithography for continuous 3D printing. *3D Printing and Additive Manufacturing.*

[J6] **Jiang, Y.**, Yarin, A. L., Pan, Y. (2020). Pintable highly transparent natural fiber composites. *Materials Letters.* 128290.

[J7] Cheng, M., **Jiang, Y.**, Yao, W., Yuan, Y., Deivanayagam, R., Foroozan, T., Huang, Z., Song, B., Rojaee, R., Shokuhfar, T., Pan, Y., Lu, J., Shahbazian-Yassar, R. (2018). Elevated-temperature 3d printing of hybrid solid-state electrolyte for li-ion batteries. *Advanced Materials*. 30(39), 1800615.

[J8] Chen, B., **Jiang, Y.**, Tang, X., Pan, Y., Hu, S. (2017). Fully packaged carbon nanotube supercapacitors by direct ink writing on flexible substrates. *ACS applied materials & interfaces.* 9(34), 28433.

[J9] Plog, J., **Jiang, Y.**, Pan, Y., Yarin, A. L. (2020) Electrostatic charging and deflection of droplets for drop-on-demand 3d printing within confinements. *Additive Manufacturing*. 101400.

[J10] Plog, J., **Jiang, Y.**, Pan, Y., Yarin, A. L. (2020). Electrostatically-Assisted Direct Ink Writing for Additive Manufacturing. Additive Manufacturing. In press.

[J11] Plog, J., Löwe, J. M., **Jiang, Y.**, Pan, Y., Yarin, A. L. (2019). Control of direct writing of ink droplets using electrowetting. *Langmuir*. 35(34), 11023.

[J12] Löwe, J. M., Plog, J., **Jiang, Y.**, Pan, Y., Yarin, A. L. (2019). Drop deposition affected by electrowetting in direct ink writing process. *Journal of Applied Physics.* 126(3), 035302.

[J13] Cheng, M., Ramasubramanian, A., Rasul, M. G., **Jiang, Y.**, Yuan, Y., Foroozan, T., Deivanayagam, R., Saray, M. T., Rojaee, R., Song, B., Yurkiv, Y. R., Pan, Y., Mahsayek, F., Shahbazian-Yassar, R. (2020). Direct ink writing of polymer composite electrolytes with enhanced thermal conductivities. *Advanced Functional Materials*. Accepted.

JOURNAL ARTICLES UNDER REVIEW

[R1] Yazdanpanah, G., Shah; Somala, S. R, Anwar, K. N., Shen, X., **Jiang, Y.**, Rabiee, B., Omidi, M., Rosenblatt, M. I., Shokuhfar, T., Pan, Y., Naba, A., Djalilian, A. (2020). In-situ porcine corneal matrix hydrogel as ocular surface bandage. *Biomaterials*. (Manuscript submitted on 7/28/2020)

[R2] Lichade, K. M., **Jiang, Y.**, Pan, Y. Hierarchical nano/micro-structured surfaces with high surface area/volume. *Journal of Manufacturing Science and Engineering*. (Manuscript submitted on 8/26/2020)

JOURNAL ARTICLES IN PROGRESS

[P1] **Jiang, Y.**, Plog, J., Yarin, A. L., Pan, Y. Liquid stability in electric field assisted direct ink writing process. (Finishing manuscript)

[P2] Plog, J., **Jiang, Y.**, Yarin, A. L., Pan, Y. Coalescence of Sessile Droplets Driven by Electric Field in the 3D Printing Framework. (Revising manuscript)

[P3] Rasul, M. G., Cheng, M., **Jiang, Y.**, Pan, Y., Shahbazian-Yassar, R. Direct ink writing of silane-boron nitride embedded solid polymer electrolyte for li-ion battery. (Collecting data)

[P4] Guidetti, M., Zampini, M. A., **Jiang, Y.**, Gambacorta, C., Smejkal, J. P., Pan, Y., Klatt, D., Royston, T. J. Magnetic Resonance Elastography of an Anisotropic Phantom made via Embedded Direct Ink Writing using Axially- and Torsionally-Polarized Radially converging Shear Waves. (Writing manuscript)

PATENTS

[PT1] Yarin, A. L., Pan, Y., Plog, J., **Jiang, Y.** University of Illinois at Chicago. (2020) "Electric-field assisted drop and jet control in 3d printing and direct writing". #2020-085, pending.

TEACHING EXPERIENCE

Teaching Assistant

University of Illinois at Chicago, Chicago, IL *08/2016 – Present*

IE-345 Regression Applications and Forecasting in Engineering	*Fall 2016*
ENGR-111 Engineering Practicum in Additive Manufacturing	*Fall 2016, Spring 2017*
IE-201 Financial Engineering	*Fall 2017*
IE-446 Quality Control and Reliability	*Spring 2018*
IE-594 Advanced Topics in 3D Printing and Additive Manufacturing	*Spring 2019, Spring 2020*

PRESENTATIONS

28th Annual International Solid Freeform Fabrication Symposium. *"A normalized trace geometry modeling method with bulge-free analysis for direct ink writing process planning"*

Austin, TX *08/2017*

APPENDIX

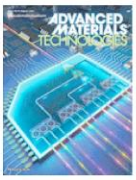

Direct Ink Writing of Wearable Thermoresponsive Supercapacitors with rGO/CNT Composite Electrodes

Author: Yizhou Jiang, Meng Cheng, Reza Shahbazian-Yassar, et al
Publication: Advanced Materials Technologies
Publisher: John Wiley and Sons
Date: Oct 18, 2019

Order Completed

Thank you for your order.

This Agreement between University of Illinois at Chicago -- Yizhou Jiang ("You") and John Wiley and Sons ("John Wiley and Sons") consists of your license details and the terms and conditions provided by John Wiley and Sons and Copyright Clearance Center.

Your confirmation email will contain your order number for future reference.

License Number	4939581232182
License date	Oct 31, 2020

Printable Details

Licensed Content

Licensed Content Publisher	John Wiley and Sons
Licensed Content Publication	Advanced Materials Technologies
Licensed Content Title	Direct Ink Writing of Wearable Thermoresponsive Supercapacitors with rGO/CNT Composite Electrodes
Licensed Content Author	Yizhou Jiang, Meng Cheng, Reza Shahbazian-Yassar, et al
Licensed Content Date	Oct 18, 2019
Licensed Content Volume	4
Licensed Content Issue	12
Licensed Content Pages	9

Order Details

Type of use	Dissertation/Thesis
Requestor type	Author of this Wiley article
Format	Print and electronic
Portion	Full article
Will you be translating?	No

About Your Work

Title	Research Assistant
Institution name	The University of Illinois at Chicago
Expected presentation date	Nov 2020

Additional Data

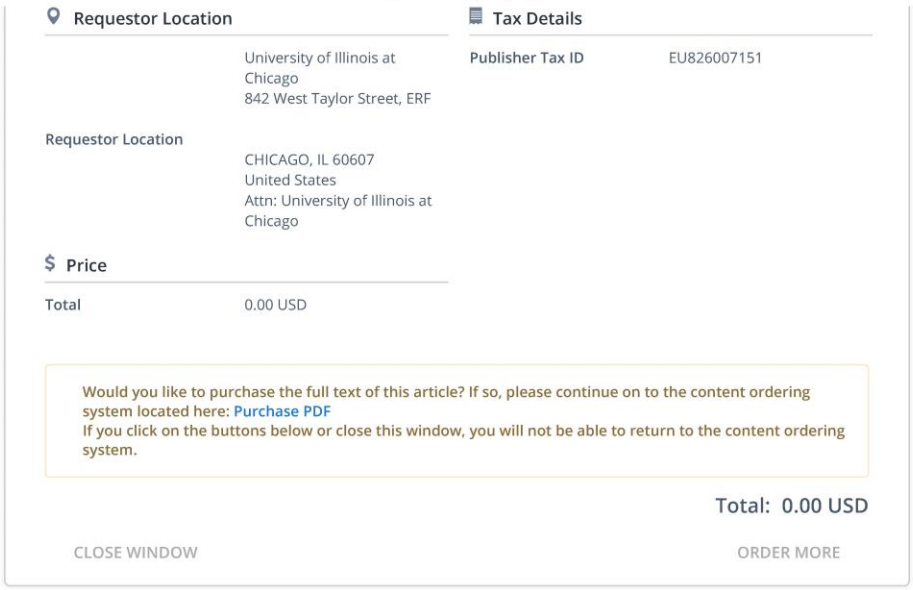

Requestor Location

University of Illinois at Chicago
842 West Taylor Street, ERF

Requestor Location

CHICAGO, IL 60607
United States
Attn: University of Illinois at Chicago

Tax Details

Publisher Tax ID EU826007151

Price

Total 0.00 USD

Would you like to purchase the full text of this article? If so, please continue on to the content ordering system located here: Purchase PDF
If you click on the buttons below or close this window, you will not be able to return to the content ordering system.

Total: 0.00 USD

CLOSE WINDOW ORDER MORE

Printable highly transparent natural fiber composites

Author: Yizhou Jiang,Alexander L. Yarin,Yayue Pan

Publication: Materials Letters
Publisher: Elsevier
Date: 15 October 2020

Direct ink writing of surface-modified flax elastomer composites

Author: Yizhou Jiang,Jevon Plog,Alexander L. Yarin,Yayue Pan

Publication: Composites Part B: Engineering

Publisher: Elsevier

Date: 1 August 2020

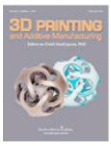

A Normalized Trace Geometry Modeling Method with Bulge-Free Analysis for Direct Ink Writing Process Planning

Author: Yizhou Jiang, Shan Hu, Yayue Pan
Publication: 3D Printing and Additive Manufacturing
Publisher: Mary Ann Liebert, Inc.
Date: Dec 1, 2018

Permissions Request

Mary Ann Liebert, Inc. publishers does not require authors of the content being used to obtain a license for their personal reuse of full article, charts/graphs/tables or text excerpt.

BACK CLOSE WINDOW

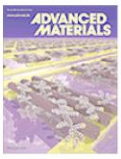

3D-Printing of Lightweight Cellular Composites

Author: Jennifer A. Lewis, Brett G. Compton
Publication: Advanced Materials
Publisher: John Wiley and Sons
Date: Jun 18, 2014

Order Completed

Thank you for your order.

This Agreement between University of Illinois at Chicago -- Yizhou Jiang ("You") and John Wiley and Sons ("John Wiley and Sons") consists of your license details and the terms and conditions provided by John Wiley and Sons and Copyright Clearance Center.

Your confirmation email will contain your order number for future reference.

License Number	4939590651932
License date	Oct 31, 2020

Printable Details

Licensed Content

Licensed Content Publisher	John Wiley and Sons
Licensed Content Publication	Advanced Materials
Licensed Content Title	3D-Printing of Lightweight Cellular Composites
Licensed Content Author	Jennifer A. Lewis, Brett G. Compton
Licensed Content Date	Jun 18, 2014
Licensed Content Volume	26
Licensed Content Issue	34
Licensed Content Pages	6

Order Details

Type of use	Dissertation/Thesis
Requestor type	University/Academic
Format	Print and electronic
Portion	Figure/table
Number of figures/tables	1
Will you be translating?	No

About Your Work

Title	Research Assistant
Institution name	The University of Illinois at Chicago
Expected presentation date	Nov 2020

Additional Data

Portions	Fig. 1b

Requestor Location

University of Illinois at Chicago
842 West Taylor Street, ERF

Requestor Location

CHICAGO, IL 60607
United States
Attn: University of Illinois at Chicago

Tax Details

Publisher Tax ID EU826007151

Price

Total 0.00 USD

Would you like to purchase the full text of this article? If so, please continue on to the content ordering system located here: Purchase PDF
If you click on the buttons below or close this window, you will not be able to return to the content ordering system.

Total: 0.00 USD

CLOSE WINDOW ORDER MORE

SPRINGER NATURE

Printing ferromagnetic domains for untethered fast-transforming soft materials

Author: Yoonho Kim et al
Publication: Nature
Publisher: Springer Nature
Date: Jun 13, 2018

Order Completed

Thank you for your order.

This Agreement between University of Illinois at Chicago -- Yizhou Jiang ("You") and Springer Nature ("Springer Nature") consists of your license details and the terms and conditions provided by Springer Nature and Copyright Clearance Center.

Your confirmation email will contain your order number for future reference.

License Number	4939591375816
License date	Oct 31, 2020

Printable Details

Licensed Content

Licensed Content Publisher	Springer Nature
Licensed Content Publication	Nature
Licensed Content Title	Printing ferromagnetic domains for untethered fast-transforming soft materials
Licensed Content Author	Yoonho Kim et al
Licensed Content Date	Jun 13, 2018

Order Details

Type of Use	Thesis/Dissertation
Requestor type	academic/university or research institute
Format	print and electronic
Portion	figures/tables/illustrations
Number of figures/tables/illustrations	1
High-res required	no
Will you be translating?	no
Circulation/distribution	1 - 29
Author of this Springer Nature content	no

About Your Work

Title	Research Assistant
Institution name	The University of Illinois at Chicago
Expected presentation date	Nov 2020

Additional Data

Portions	Fig. 1a

Acoustic control of microstructures during direct ink writing of two-phase materials

Author: Leanne Friedrich,Rachel Collino,Tyler Ray,Matthew Begley
Publication: Sensors and Actuators A: Physical
Publisher: Elsevier
Date: 1 December 2017

Order Completed

Thank you for your order.

This Agreement between University of Illinois at Chicago -- Yizhou Jiang ("You") and Elsevier ("Elsevier") consists of your license details and the terms and conditions provided by Elsevier and Copyright Clearance Center.

Your confirmation email will contain your order number for future reference.

License Number	4939600191185
License date	Oct 31, 2020

Printable Details

Licensed Content

Licensed Content Publisher	Elsevier
Licensed Content Publication	Sensors and Actuators A: Physical
Licensed Content Title	Acoustic control of microstructures during direct ink writing of two-phase materials
Licensed Content Author	Leanne Friedrich,Rachel Collino,Tyler Ray,Matthew Begley
Licensed Content Date	Dec 1, 2017
Licensed Content Volume	268
Licensed Content Issue	n/a
Licensed Content Pages	9
Journal Type	S&T

Order Details

Type of Use	reuse in a thesis/dissertation
Portion	figures/tables/illustrations
Number of figures/tables/illustrations	3
Format	both print and electronic
Are you the author of this Elsevier article?	No
Will you be translating?	No

About Your Work

Title	Research Assistant
Institution name	The University of Illinois at Chicago
Expected presentation date	Nov 2020

Additional Data

Portions	Fig. 1

Requestor Location

University of Illinois at Chicago
842 West Taylor Street, ERF

Requestor Location

CHICAGO, IL 60607
United States
Attn: University of Illinois at Chicago

Price

Total 0.00 USD

Tax Details

Publisher Tax ID 98-0397604

Total: 0.00 USD

CLOSE WINDOW ORDER MORE